University of Liverpool

Doctoral Thesis

Development of the Pixel Tracker and Study of Combinatoric Background for the Mu3e experiment

---

Author:
Andrew Groves

Supervisor:
Prof. Joost Vossebeld
Dr. Nikolaos Rompotis

Thesis submitted in accordance with the requirements of the University of Liverpool for the degree of Doctor in Philosophy by Andrew Groves

in the

Particle Physics
Department of Physics

April 23, 2022

UNIVERSITY OF LIVERPOOL

Abstract

Development of the Pixel Tracker and Study of Combinatoric Background for the Mu3e experiment

by Andrew Groves

The Mu3e experiment is dedicated to the search for the decay $\mu^+ \to e^+e^+e^-$ with a sensitivity aim of 10^{-16} using the world's most intense muon beam. This decay violates lepton flavor conservation and is strongly suppressed in the standard model, however there are many models that go beyond the standard model that do predict some level of flavor violations making this decay a great indicator for new physics.

There are many challenges to measuring this decay with this sensitivity. For instance, we need excellent momentum, space and time resolution to be able to reduce background levels to allow for the sensitivity aim. In this thesis I will describe how the detector aims to tackle some on these challenges and explain in detail the work done on developing the construction methods and quality assurance tests for the outer pixel tracker.

Due to the high rate of muons that will be decaying in this experiment a good understanding of potential background sources is important. This thesis will detail the simulation and estimation of the main background of Internal Conversion and will also go onto optimising the selection criteria used to find good events. Another potential source of background is from combinations of multiple decays that have been reconstructed together. The main source of this background is Bhabba and Michel and is studied in detail in Ref. [1]. This thesis will discuss another two types, Internal Conversion and Michel as well as Photon Conversion and Michel, and it will detail the event estimate in the signal region.

Acknowledgements

I would like to thank Joost and Nikos first for the many hours of guidance they have provided. I would like to thank the rest of the Mu3e group in Liverpool; Helen, Sean, Afaf and in particular Carlos for all the assistance in the Lab and checking all my strange ideas. I would also like to thank the Liverpool HEP computing department for answering all my simple questions, in particular Steve as without his help I would never have been able to port the Mu3e software onto the Cern GRID.

I would like to thank the rest of the Mu3e collaboration in particular Frank, for his friendly face and travel guidance. Richard and Kirk, for their detector help. I would also like to thank the Heidelberg pixel team for helping with the testbeam work, particularly David and Heiko who helped with all my software questions. Locally I would thank Jan and Eva for helping with MuPix.

I would like to thank the friendly office for providing plenty of procrastination with our endless talking and trips to the AJ. Finally, I would like to thank Amy and my family for the love and support throughout this work.

Contents

Chapter 1

The Standard Model and beyond

Particle physics is concerned with the fundamental constituents of nature and their interactions. The current theory to describe these is known as the Standard Model, which is one of the most tested theories in history and has held up remarkably well [2, 3]. However, there are a number of areas that the Standard Model doesn't explain.

This chapter will focus on the Standard Model with special attention to its flavour structure. The chapter will then move on to discussing the problems with the Standard Model before explaining the current theories that include charged lepton flavour violation.

1.1 The Standard Model of Particle Physics

The world that we live in appears to be made up of just a few particles. Atoms make up everything that we see in nature however these are not fundamental, but they are made up of electrons, protons and neutrons. The electron is the only particle out of these that does not consist itself of other particles; if we probe further into the proton and neutron it is found that they are bound states of particles called quarks, namely up and down quarks. These 3 particles including the electron neutrino form the first generation of spin $\frac{1}{2}$ particles called fermions. Each of these also has a corresponding antiparticle, which are particles that have the same mass but opposite quantum numbers. In high energy interactions more particles are found, which can be grouped into 3 different generations, as shown in figure 1.1. There are 3 different types of particles in this diagram, leptons, quarks and bosons. Flavour refers to the species of an elementary particle. The Standard Model counts six flavours of quarks and six flavours of leptons. The

bosons are the forces carriers while the matter particles are leptons and quarks. The leptons discovered are the electron, muon and tau as well as their neutrino counterparts. All of these particles behave in the same way with respect to the electromagnetic and weak interactions with the main difference being their mass. When the muon was first discovered and identified as a lepton it was first thought that it was an excited state of the electron. This however would mean that the decay $\mu^- \longrightarrow e^-\gamma$ should be possible [4]. This was not observed [5] leading to a new quantum number being introduced, called lepton number, which was assumed to be a conserved quantity. Each generation has its own lepton number. In weak interactions each lepton is accompanied by its own neutral partner called a neutrino, which was first proposed by Pauli to solve the β decay problem of the conservation of energy and angular momentum [6]. Hadrons are bound states of several quarks. There are two classes of these namely mesons with integer spin and baryons with half integer spin. Baryons and mesons have integer charge while the quarks have fractional charge, namely $-\frac{1}{3}$ and $\frac{2}{3}$. Quarks carry numerous quantum numbers. The first being colour which takes the values red, green and blue. The colour quantum number acts like a charge in the strong force. The second being a flavour quantum number e.g. strangeness for the strange quark. The final quantum number is weak isospin explained in section 1.1.2. Flavour is conserved in quarks for the strong and the electromagnetic interactions, however this conservation is broken for the weak interaction.

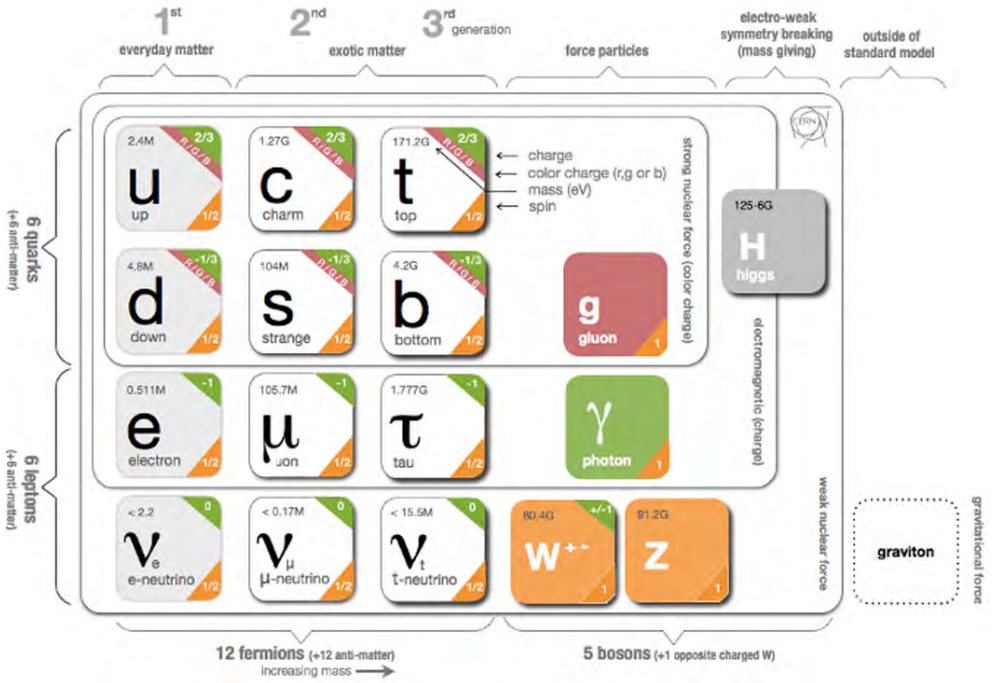

FIGURE 1.1: The Standard model including 3 generation of matter particles and the gauge bosons. The spin, mass and charge are also shown as well as which particles participate in each force [7].

1.1.1 Particles interactions

There are 4 fundamental forces in nature: the weak force, the electromagnetic force, the strong force and gravity. Each of these are mediated by the exchange of virtual particles called gauge bosons. Gravitational interactions between particles are feeble and can be neglected at present energies. The strong force is responsible for binding quarks together. It is mediated by the gluon which also carries colour charge. There are 8 different colour charged gluons, each carrying a colour and anti-colour. Only the quarks and gluons carry colour charge, and these are the only particles to interact via the strong force. The current best theory to describe the strong force is Quantum Chromodynamics (QCD) [2, 8–10]. The electromagnetic interaction is mediated by the photon, this couples to electric charge meaning that all charged particles can interact by this force, it is described by Quantum Electrodynamics (QED) [3, 11–14]. The last force is the weak interaction, which is mediated by the massive W^+, W^- and Z bosons, which couple to weak isospin. This force is explained in more detail in section 1.1.2.

1.1.2 Weak interaction

To be able to describe the weak interaction some key principles need to be introduced. We first need to explain what parity, and chirality are. After this we will move on to discussing the form of the weak interaction and its implications on lepton number. The following section discusses weak currents. For a more detailed description see Ref. [4].

Parity

The parity transformation (or space inversion) is defined by,

$$\boldsymbol{P} : \overrightarrow{x} \rightarrow \overrightarrow{x'} = -\overrightarrow{x}. \tag{1.1}$$

which simultaneously flips the sign of all three spatial coordinates. This has a different effect depending on the type of vector or scalar e.g. it inverts polar vectors but not axial vectors and pseudoscalar but not scalar quantities. The parity operator can also be applied to a rest frame Dirac spinor ($\vec{p} = \vec{0}$) leading to these having intrinsic parity of ± 1. Parity plays a important role in the weak interaction which has been shown to be parity violating.

Charge and CP

With the discovery of the positron [15] it was proposed that a new type of charge symmetry existed, this was extended to all fermions and bosons by Feynman. This assumes the forces behave in the same way no matter what charge a particle has. However, it can be shown that charge symmetry only holds for electromagnetic and strong interactions but is violated in weak interactions.
This led to the proposal that a combined symmetry of charge and parity could be conserved. This was later found to also be broken, be it at a very small level by CP violating decays of neutral kaons, discussed further in section 1.1.3 [16].

Helicity and chirality

In the weak interaction only, the left-handed chiral components take part. To understand this statement, we first need to explain helicity. Physically, helicity eigenstates are eigenstates of the spin operator resolved along the direction of $\overrightarrow{p}$. This is useful when the spin operator does not commute with the energy

operator, so cannot be known at the same time. As helicity does commute, we are able to get some information about the spin.

Another operator that can commute with the energy operator is the γ_5 matrix, thus states may also be classified by the eigenvalues of γ_5. The γ_5 matrix is the product of the 4 other gamma matrices, also known as Dirac matrices, these are a set of generic matrices with specific anticommutation relations. This has a small change with respect to helicity where the fermions eigenvalues are equal to the helicity while for anti-fermions it is equal to minus the helicity. These eigenvalues are known as chirality and γ_5 as the chirality operator. This is only true in the massless limit; thus, we must regard the mass terms as coupling to states of different chirality. The different states are known as left and right-handed.

V-A theory and parity violation

In 1957 it was found that parity is violated in weak interactions, specifically in nuclear β decays [17]. This meant that the theory at the time, the Fermi theory, needed modifying to explain this. The modification was to have a theory with vector and axial vector currents to naturally introduce parity violation [18].

In the new formulation of the weak currents the term $(1 - \gamma_5)$ which is the left-handed chirality projector operator appears, this term dictates that only left handed components of the Dirac spinor enters into the weak interaction.

1.1.3 Weak interaction currents

Now that the weak interaction is understood to be parity violating, we can discuss the form of the currents which make up the interaction Hamiltonian. First the leptonic weak currents are discussed followed by the quark currents. The quark currents are important as the weak interaction does not couple to the mass eigenstates for quarks but rather to different weak eigenstates. These are related by the Cabibbo-Kobayashi-Maskawa (CKM) matrix.

Leptonic weak currents

The total leptonic charged current is defined as

$$j^{\mu}_{CC}(\text{leptons}) = j^{\mu}_{weak}(e) + j^{\mu}_{weak}(\mu) + j^{\mu}_{weak}(\tau) \tag{1.2}$$

where

$$j^{\mu}_{weak}(e) = \overline{\nu_e}\gamma^{\mu}\frac{(1-\gamma_5)}{2}e \tag{1.3}$$

where $\overline{\nu_e}$ is the adjoint spinor ($\theta^{\dagger}\gamma_0$), e is the fermion spinor and γ^{μ} are the Dirac gamma matrices and run from 0 to 3. The reason that this is referred to as the charged lepton current is because each part, $j^{\mu}_{wk}(e)$ has a total charge. Each lepton pair has the same coupling, independent of flavour.

However this is not the end of the story, in 1973 a neutral current decay was observed [19]. This was predicted earlier in the Glashow-Salam-Weinberg (GSW) [20–22] theory and leads to two neutral currents and introduces a number of constants; namely c^l_L, c^l_R and g_N. The constants (c^l_L, c^l_R) are the relative combination of V-A and V+A , while g_N is the strength of the neutral current compared to charged ones (g).

In the GSW theory these values are predicted in terms of the weak mixing angle (θ_W) where,

$$g_N = \frac{g}{\cos\theta_W},\ c^l_L = -\frac{1}{2} + \sin^2\theta_W,\ c^l_R = \sin^2\theta_W. \tag{1.4}$$

The coefficients are independent of flavour. The most recently determined value of $\sin^2\theta_W$, by CODATA in 2018, is 0.22290 ± 0.00030 [23].

Quark Weak currents

Now turning the attention to the quark sector, we will start by only considering two generations a quarks to follow a historic route.

With the discovery of quarks it was found that the weak currents follow the same form as for the leptons. This shows universality between leptons and quarks in the weak interaction. However a problem was that the rate of $d \to u$ is slightly lower than $\mu^- + W^+ \to \nu_\mu$. This problem was solved by saying that the strength of the weak interaction was shared between the $\Delta S = 0$ and the $\Delta S = 1$ transitions [24]. This leads to weak charged currents for quarks to be

$$j^{\mu}_{Cab}(e)(u,d,s) = \cos\theta_C\overline{u}\gamma^{\mu}\frac{(1-\gamma_5)}{2}d + \sin\theta_C\overline{u}\gamma^{\mu}\frac{(1-\gamma_5)}{2}s \tag{1.5}$$

where $\overline{u}$ is the adjoint spinor, d and s are the fermion fields, γ^μ are the Dirac gamma matrices and θ_C is the Cabibbo angle. This can be rewritten by introducing a mixed quark field,

$$d' \equiv \cos\theta_C d + \sin\theta_C s \tag{1.6}$$

thus,

$$j^\mu_{Cab}(e)(u,d,s) = \overline{u}\gamma^\mu \frac{(1-\gamma_5)}{2} d'. \tag{1.7}$$

It was however noticed by Glashow–Iliopoulos–Maiani (GIM) that this raises an issue in the second order as processes such as $K_2 \to \mu^+ + \mu^-$ or $K^+ \to \pi^+ + l + \bar{l}$ would be $\Delta S = 2$ transitions [25]. To get around this problem they introduced a fourth quark, now called the charm quark. This new quark would couple in a similar way as before leading to the 4 quark current being,

$$j^\mu_{Cab}(e)(u,d,c,s) = \overline{u}\gamma^\mu \frac{(1-\gamma_5)}{2} d' + \overline{c}\gamma^\mu \frac{(1-\gamma_5)}{2} s'. \tag{1.8}$$

GIM proposed describing the weak interaction by a SU(2) Yang-Mills gauge theory, which later transpired to be of U(1)xSU(2) symmetry. This formulation unified electromagnetism with the weak interaction, and the generators of SU(2) is what we call weak isospin. Thus, the weak neutral quark currents become

$$g_N \sum_{q=u,c,d',s'} \overline{q}\gamma^\mu \Big(c^q_L \frac{1-\gamma_5}{2} + c^q_R \frac{1+\gamma_5}{2} \Big) q. \tag{1.9}$$

In summary the quark fields that participate in the weak interaction are (u, d') and (c, s') where s' and d' are not the fields with definite mass but are related to the mass eigenstates s and d by the Cabibbo matrix. The main problem with this matrix was that CP violation had been seen to occur within the first 2 generations of quarks. To achieve this there needed to be a complex phase introduced somewhere in this matrix. Kobayashi and Maskawa attempted to do this, however they found that for 2 generations of quarks this was not possible. They then showed that a 3-generation model could introduce a CP violating phase. This discovery as well as the discovery of the bottom quark 4 years later

helped confirm a 3-generation model [26]. The full matrix is then,

$$\boldsymbol{V} = \begin{pmatrix} V_{ud} & V_{us} & V_{ub} \\ V_{cd} & V_{cs} & V_{cb} \\ V_{td} & V_{ts} & V_{tb} \end{pmatrix} \tag{1.10}$$

which is known as the Cabibbo-Kobayashi-Maskawa (CKM) matrix [27].

1.1.4 Neutrino oscillations

In the late 1960s the Brookhaven Solar Neutrino Experiment studied the amount of solar neutrinos produced during nuclear fusion [28]. This experiment found only a third of the predicted number thus giving rise to the solar neutrino problem. This problem was solved by Super-Kamiokande in 1998 and the SNO collaboration in 2002 which gave evidence for neutrino oscillations [29, 30].
Neutrino oscillations can be explained by saying that the mass eigenstates, labelled ν_1, ν_2 and ν_3, are not the same as the weak eigenstates measured but rather a combination of all 3. The mass eigenstates can be related to the weak eigenstates by the Pontecorvo–Maki–Nakagawa–Sakata (PMNS) matrix [31, 32].

$$\begin{bmatrix} \nu_e \\ \nu_\mu \\ \nu_\tau \end{bmatrix} = \begin{bmatrix} U_{e1} & U_{e2} & U_{e3} \\ U_{\mu 1} & U_{\mu 2} & U_{\mu 3} \\ U_{\tau 1} & U_{\tau 2} & U_{\tau 3} \end{bmatrix} \begin{bmatrix} \nu_1 \\ \nu_2 \\ \nu_3 \end{bmatrix} \tag{1.11}$$

Using this matrix the probability for a neutrino to oscillate to a different flavour can be found if we say that $\nu_{e,\nu,\tau}$ evolve according to the time dependence of the mass eigenstates. Following this through, you get the general form shown in equation 1.12. This shows that the oscillations depend on the energy of the neutrino, the distance that the neutrino travels and the mass difference between the mass eigenstates.

$$P(\nu_\alpha \longrightarrow \nu_\beta) = \sum_{ij} U^*_{\alpha i} U_{\beta j} U_{\alpha i} U^*_{\beta j} e^{-i(\delta m^2_{ij} L/2E)} \tag{1.12}$$

1.1.5 Problems with the Standard Model

The Standard Model describes many phenomena and predicts the existence of many particles. However, there are still many phenomena and experimental observations that are not explained by this theory.

The most obvious natural phenomenon that the Standard Model doesn't describe is gravity, however this effect is negligible at the typical energy levels studied in high-energy-physics. There have been efforts to describe gravity as a quantum field theory however there are still issues yet to be resolved [33, 34].

Astrophysics has several observations that give evidence for a new unknown type of matter and energy, dubbed dark matter and dark energy. Dark matter was introduced as a way of solving the velocity of galaxy spiral arms [35, 36]. While dark energy was introduced to explain the anisotropy in the cosmic microwave background radiation [37]. The percentage of these is measurable by determining the cosmological constants, this has shown that the universe is made up of 69% dark energy, 26% dark matter and only 5% baryonic matter [38]. This implies that the particles described by the Standard Model framework do not account for 95% of the universe.

The Standard Model is also not able to sufficiently explain the imbalance of matter and anti-matter in the universe, there are mechanisms, but it is not enough. For this imbalance to occur Andrei Sakharov set 3 conditions [39]: these are baryon number violation, CP violation and interactions out of thermal equilibrium. CP violation is allowed in the SM and observed, however only for weak interactions. It is a great puzzle as to why it is not observed in the strong interaction, even though it is not prohibited.

The observations of neutrino oscillations shows that they have mass, this is not included in the Standard Model but can be extended to include this. Neutrino oscillations violate lepton number, a property otherwise conserved in the Standard Model [28, 29, 40].

Another problem to consider is why the Higgs boson mass is so much lighter than the Planck mass, this is called the hierarchy problem. This is because you would expect the quantum corrections to the Higgs mass making its value huge compared to where it sits.

In the Standard Model, interactions involving leptons are universal, this means that they are the same irrespective of flavour. Recent observations however

seem to challenge this universality. There are indications that currently it is found in B mesons decays there are larger than expected rates for decays to τs. The significance of these results sits at 4 standard deviations [41].

There are other results that the Standard Model is not able to explain. In the Standard Model the radius of hydrogen is predicted and confirmed in experiment, however the radius of muonic hydrogen is predicted but the observed value deviates from the prediction by as many as 7 standard deviations [42–45]. Another result is the magnetic moment of the muon, its current observed value is 4.2 standard deviations from the Standard Model with a new g-2 experiment at FNAL reducing the uncertainty [46–48].

1.2 Charged lepton flavour violation

With the observation of neutrino oscillations, it is shown that lepton number is not a conserved quantity, however, to this day there has been no detection of it in the charged sector. There have been many searches to try and identify any violation [49–51]. These are shown in figure 1.3 along with what decay channel was under investigation. It also shows future experiments predicted sensitivity including Mu3e with an aim of 10^-16. Many of these experiments used muons due to several reasons, for example their ease of production and their purely leptonic decays. The last observations in some of the main decay channels are detailed in section 1.3. The advantage of these types of searches is the near zero contribution from the Standard Model. This is because the only contribution in the Standard Model is due to neutrino mixing leading to a branching ratio that is extremely small [52–54]:

$$Br(\mu \to e\gamma) = \frac{3\alpha}{32\pi}\Big| \sum_{i=2,3} U^*_{\mu i} U_{ei} \frac{\Delta m^2_{i1}}{M^2_W}\Big|^2 < 10^{-54}, \tag{1.13}$$

as it happens by neutrino mixing, as shown in figure 1.2 Thus any signal would indicate new physics as no experiment gets near to this sensitivity. The most sensitive experiment to date is from MEG and sets a limit of $< 4.2 \times 10^{-13}$ at a 90% confidence level [50]. The planned upgrade will push this to $< 6 \times 10^{-14}$. The reason for this small branching ratio is due to the GIM mechanism. With the relative masses of the W ($M_W = 80.4$ GeV) and the neutrino mass difference

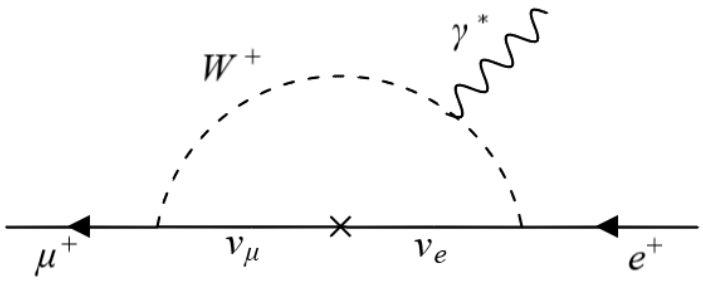

FIGURE 1.2: Standard Model Feynman diagram for the decay $\mu \to e\gamma$.

($\mathcal{O}(10^{-3}\ eV^2)$). The SM branching ratio of the decay $\mu \to eee$ would be even smaller than $\mu \to e\gamma$ due to the addition vertex after the photon.

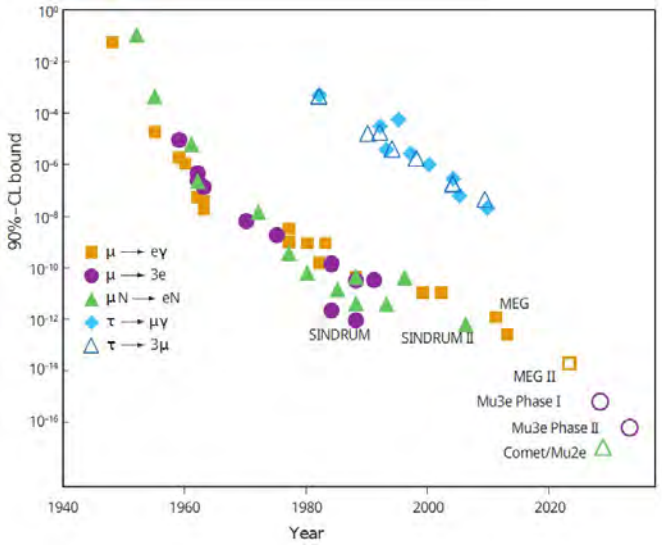

FIGURE 1.3: The history of CLFV searches and their 90% confidence limits in the main muon and tau channels and the expected limits for future experiments [55, 56].

1.2.1 Effective theory for lepton flavour violation

An effective Lagrangian can be used to describe lepton flavour violation [57]. These Lagrangians are constructed as an extension of the Standard Model by increasing the dimensions beyond the 4 in the Standard Model. The Lagrangian

terms that are of interest for the decay $\mu \to eee$ are proposed by [54];

$$\begin{aligned} L_{\mu\to eee} \;=\; & \frac{4G_F}{2}\,[m_\mu A_R\,\overline{\mu_R}\sigma^{\mu\nu}e_L F_{\mu\nu} + m_\mu A_L\,\overline{\mu_L}\sigma^{\mu\nu}e_R F_{\mu\nu} \\ & +\; g_1\,(\overline{\mu_R}e_L)\,(\overline{e_R}e_L) + g_2\,(\overline{\mu_L}e_R)\,(\overline{e_L}e_R) \\ & +\; g_3\,(\overline{\mu_R}\gamma^\mu e_R)\,(\overline{e_R}\gamma_\mu e_R) + g_4\,(\overline{\mu_L}\gamma^\mu e_L)\,(\overline{e_L}\gamma_\mu e_L) \\ & +\; g_5\,(\overline{\mu_R}\gamma^\mu e_R)\,(\overline{e_L}\gamma_\mu e_L) + g_6\;(\overline{\mu_L}\gamma^\mu e_L)\,(\overline{e_R}\gamma_\mu e_R) \;+\; H.c.\,]\,. \end{aligned} \tag{1.14}$$

In this equation the terms $A_{R,L}$ are the coupling constants for the decay $\mu_R \to e_L\gamma$ and $\mu_L \to e_R\gamma$, while the other terms are four fermion interaction terms and H.C. is the Hermitian conjugate.

To understand the different charged lepton flavour violation modes' effective mass sensitivity it is useful to change the parametrisation in equation 1.14. An alternative form is shown in equation 1.15 [58]. This introduces 2 key parameters, Λ which is the effective mass scale of the new physics and κ which is the relative size of the 2 types of interactions. Using these parameters a plot can be produced, seen in figure 1.4, showing the sensitivity to the branching ratio of the respective decay modes at a given value of Λ and κ.

$$\begin{aligned} L_{LFV} \;=\; & \left[\frac{m_\mu}{(\kappa+1)\Lambda^2}\;\overline{\mu_R}\sigma^{\mu\nu}e_L F_{\mu\nu}\right]_{\gamma-\text{penguin}} \\ & +\left[\frac{\kappa}{(\kappa+1)\Lambda^2}\;(\overline{\mu_L}\gamma^\mu e_L)\,(\overline{e_L}\gamma_\mu e_L)\right]_{\text{tree}} \end{aligned} \tag{1.15}$$

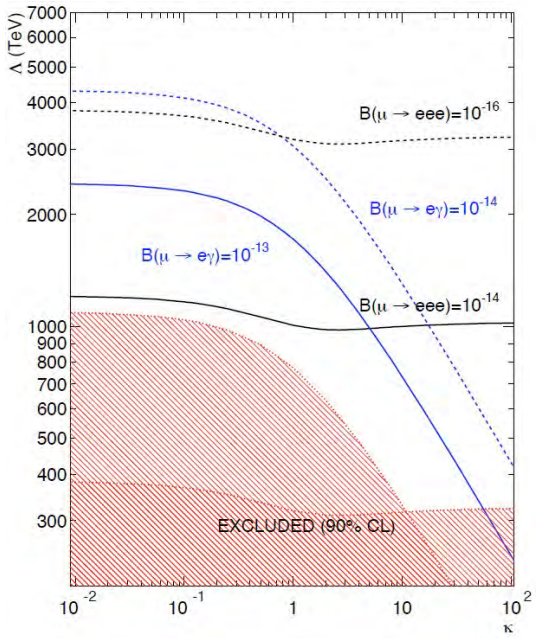

FIGURE 1.4: Sensitivity of the $\mu \to e\gamma$ and $\mu \to eee$ channel as a function of the ratio of penguin diagram to the tree diagrams. The red shaded region is the current excluded region of the branching ratio based on current experimental results. The solid and dashed lines will be future excluded limits with new experimental result [58].

1.2.2 Models to describe lepton flavour violation

Supersymmetric models

Supersymmetric models are of great interest in particle physics as they provide a solution to the hierarchy problem. This is because the quadratic cancellation associated with the added SUSY particles mean the Higgs scalar mass will be naturally of the electroweak order.

In the minimal supersymmetric extension to the Standard Model each Standard Model particle has a partner particle, e.g. slepton [59]. For CLFV the particles of interest are the sleptons, sneutrinos, neutralinos ($\widetilde{\chi}_i^0$) and charginos ($\widetilde{\chi}_i^{\pm}$). The $\widetilde{\chi}_i^0$ and $\widetilde{\chi}_i^{\pm}$ are a mixture of the neutral and charged gauginos and Higgsinos. New sources of CLFV can accrue due the couplings between these particles, provided the mass matrices for the lepton and sleptons do not align, as is the case in a majority of theories.

SUSY models can be embedded into grand unified theories. This is when the standard model gauge groups are part of a larger group at higher energies. One such higher group is SU(5), this can produce lepton flavour violation through

radiative corrections to the SUSY breaking term causing the masses. For some parameters of this theory it could produce a branching ratio at the level of 10^{-16} for the decay $\mu \to eee$ [54, 60]. A Feynman diagram for the decay $\mu \to e\gamma$ in super symmetry is shown in figure 1.5.

In minimal supersymmetric models where there is a requirement of gauge invariance, interactions can happen that violate baryon and lepton number conservation. However, to prevent the proton decaying too fast ($10^{-}2$ seconds), a parity is introduced to distinguish superparticles from ordinary particles. This is called R-parity and defined as $(-1)^{3B-L+2S}$, where B, L and S are the baryon number, lepton number, and spin, respectively. It is also possible that this isn't conserved, provided the coupling constants to introduce proton decay are suppressed. This would lead to a larger contribution to tree level diagrams for $\mu \to eee$ [61].

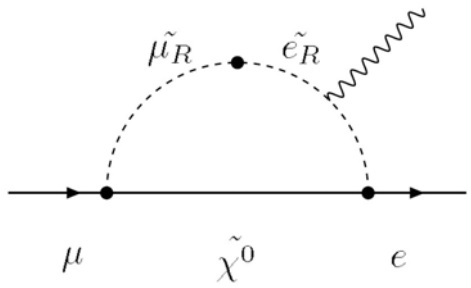

FIGURE 1.5: Feynman Diagram for SU(5) SUSY theory for the decay $\mu \to e\gamma$ [54].

Other models

If you introduce neutrino mass and mixing to the SM this introduces lepton flavour violation only at unobservable levels. If, however, you introduce neutrino mass by the seesaw model, where there is a heavier right-handed neutrino to account for the small mass of the neutrinos, then the branching ratio would increase. However even for the most extreme masses this would only increase the branching ratio to $\mathcal{O}(10^{-40})$ from the Standard Model branching ratio of $\mathcal{O}(10^{-54})$, remaining undetectable in Mu3e [62].

There are also theories that allows for a heavy boson and charged fermion to run in a penguin diagram, this can lead to an enhancement of the decay $\mu \to eee$ while the decay $\mu \to e\gamma$ doesn't receive a enhancement. One of these models is

the doubly charged Higgs [63].

1.3 Charged lepton flavour violation experiments

Due to the many different theories for lepton flavour violation with varying predicted branching ratios, measuring these can provide a good test for new physics. There are many different processes that can be searched for to identify CLFV for instance rare muon and tau decays and muon to electron conversion on nuclei. Muons provide the most stringent limit as they can be produced in large quantities, have a long lifetime (2.2 μs) as well as having purely leptonic decay modes. The main muon decay modes that are examined are $\mu \to e\gamma$ being investigated by MEG [50]. Comet [64] and Mu2e [65] are investigating $\mu N \to eN$. While $\mu \to eee$ is what Mu3e will measure. These all have a muon beam hit a target and measure the decay particles. The current limit of $\mu \to eee$ was set by SINDRUM [66] so this will also be discussed here.

1.3.1 SINDRUM

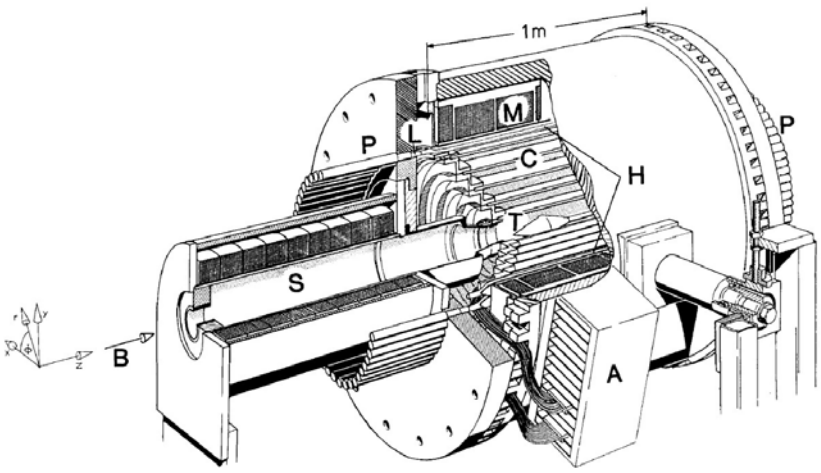

FIGURE 1.6: Diagram of SINDRUM. The incoming muons (B) are stopped on the target (T). The multiwire proportional chambers (C) measure the momentum and the hodoscope (M) the timing of the decay products [49].

The last search for $\mu \to eee$ was performed in 1988 by the SINDRUM experiment at the Swiss Institute for Nuclear Research (now PSI). In this experiment no events were found in the signal region. Thus they set a upper limit on the

branching ratio of $< 1 \times 10^{-12}$ at a 90% confidence level [66]. The spectrometer used in this experiment is shown in figure 1.6, the beam was stopped at a rate of $5 \times 10^6 \mu/s$ in a hollow double cone target. The resulting electrons were detected by 5 concentric multi wire proportional chambers, 3 of which are also equipped with cathode strips to find the z coordinate, and an array of scintillation counters. All of these were housed in a magnetic field of 0.33 T.
SINDRUM was then upgraded to investigate neutrinoless $\mu^- \to e^-$ conversion in muonic atoms. For this they set a limit on the decay of $< 7 \times 10^{-13}$ at a 90% confidence level.

1.3.2 MEG and MEG II

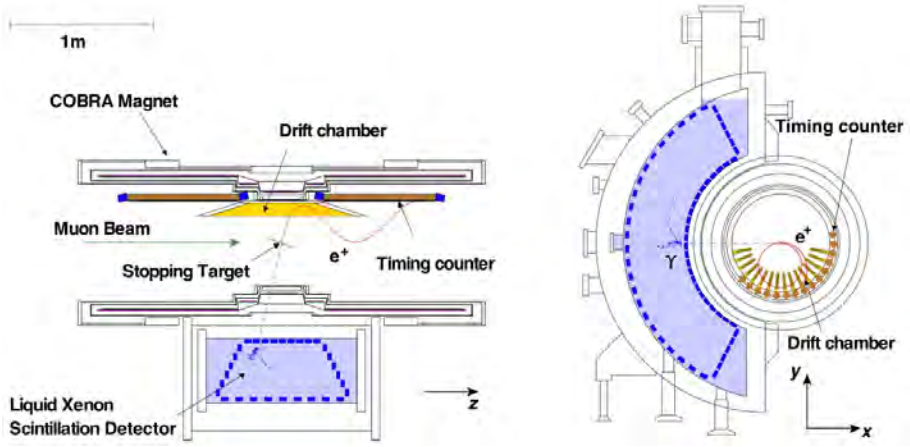

FIGURE 1.7: A schematic of the MEG detector showing a simulated event as well as labelling all the main elements of the detector [50].

The most recent measurement of charged lepton flavour violation is by **Mu** to **E G**amma (MEG) by examining the decay $\mu \to e\gamma$. This experiment ran from 2009-2013 at PSI.
A total of 7.5×10^{14} muons where stopped in the experiment and no excess was found thus setting a new upper limit on this decay of $< 4.2 \times 10^{-13}$ at a 90% confidence level [50].
In the experiment the muons were stopped by a thin stopping target composed of a single sheet of polyethylene at an angle of 70° to maximise stopping while minimising multiple scattering and Bremsstrahlung. The resulting positrons were detected by a drift chamber system consisting of 16 independent modules covering the angles 191.25° to 378.75° [67]. The timing of the positrons was

measured by the timing counters consisting of scintillating bars. The photons were detected by a liquid Xenon calorimeter, designed to fully contain a 52.83 MeV photon shower. All but the liquid Xenon detector were in a superconducting magnet with a field of 1.27 T at the centre. The setup is shown in figure 1.7.

This detector has been upgraded to improve the sensitivity to 6×10^{-14}, and started collecting data in 2021 and still is a the time of writing. It will achieve this sensitivity by an upgrade of the drift chamber to a cylindrical drift volume and an improved timing detector using scintillating tiles. There is also a new Radiative Decay counter designed to help suppress the background [68].

1.3.3 Mu2e and Comet

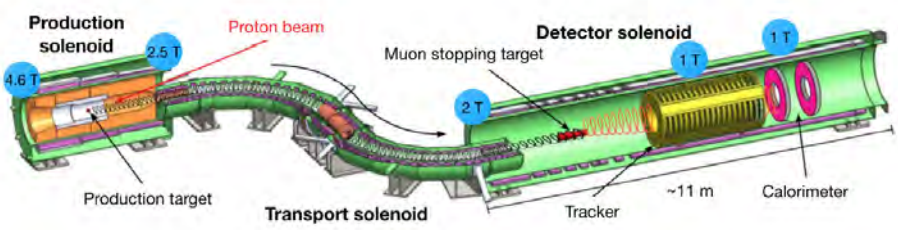

FIGURE 1.8: Diagram of the Mu2e detector with all the main elements of the detector [69].

The Mu2e and Comet experiments investigate muon to electron conversion in muonic atoms. This is when muons are trapped in the orbit around the target material's nuclei. If a muon undergoes a CLFV transition to an electron, the energy of the emitted electron is equal to the muon mass minus the binding energy and the energy of the recoiling nucleus. There are no standard model decay electrons which have an energy this high.

The Mu2e experiment is located at Fermilab and plans to study the decays of 10^{18} muons on an aluminium target taken in a period of 3 years. It aims for a sensitivity of $5{\times}10^{-17}$ and to start running in 2024. It will use a pulsed proton beam hitting a tungsten target to produce a beam of pions. These then decay into muons and the transport solenoid will remove any excess pions, leaving only muons. This transport solenoid also allows for the selection of momentum. This is done by adjusting the magnetic field so only muons with the desired momentum is able to travel around to the stopping target. The momentum of

electrons, produced by the muon conversion or background processes, is measured using straw drift tubes. The straw tracker has a hole in the middle to allow it to miss low momentum electrons, a source of background in this experiment as they come from 3 body muon decays. It is then followed by a CsI calorimeter, which is used for many purposes such as timing information and particle identification. The data taking doesn't start until 700 ns after the beam pulse to reduce beam related backgrounds [65, 69].

The COMET (Coherent Muon to Electron Transition) experiment will be performed at J-Parc, also using a muon beam hitting an aluminium target. Phase one of the experiment aims to have a sensitivity of 3×10^{-15}. Beam commissioning will start in 2022, with the aim of physics measurements in 2023. The target is located in a drift chamber to measure the momentum of the electrons [64]. There is also a phase 2 planned which will reach a sensitivity of 2.6×10^{-17}. It will change the transport solenoid allowing for a better momentum selection of the muons. After the target a detector solenoid will be placed, this will allow low momentum electrons and beam related backgrounds to be removed. The detector technology will be changed to straw tubes and an electron calorimeter. Figure 1.9 shows a diagram of the detectors for phase 1 and 2. [70].

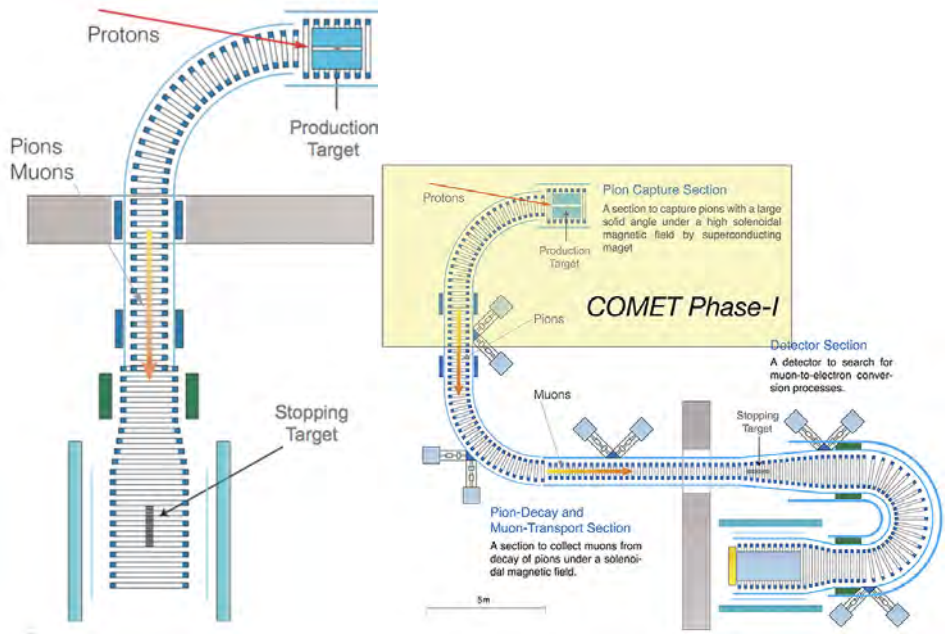

(a) (b)

FIGURE 1.9: Diagram of COMET phase 1 (A) and 2 (B) [71].

Chapter 2

The Mu3e Experiment

The Mu3e experiment aims to observe the decay $\mu^+ \to e^+e^+e^-$ if the branching ratio is larger than 10^{-16} or to exclude higher branching ratios to a 90% confidence level. This decay complements other CLFV experiments and searches and will provide a good probe into new physics beyond the Standard Model. To be able to achieve the sensitivity aim more than 10^{17} muons need to be stopped. To take the data in a reasonable time frame of 3 years the muon beam rate needs to be of order 10^9 Hz.

The current best source of low energy muons is the $\pi E5$ beam line at PSI, providing a rate of 1×10^8 Hz. This will allow for a competitive limit of 2×10^{-15} to be set and allow the collaboration to develop the technology solutions needed achieve the overall aim. This will be known as phase-I, aiming to take data in 2024. A new high intensity beam line is currently under investigation at PSI to provide the needed muon rate to achieve the aimed sensitivity, this is known as phase-II aiming for 2029 . This chapter will describe the concept of detection before describing the phase-I detector in detail, for more information see the Mu3e Technical design report (TDR) [1].

2.1 The Signal and background of the mu3e experiment

The decay $\mu^+ \to e^+e^+e^-$ is characterised by 2 positrons and 1 electron coming from a single vertex at the same point in time. The total energy of the 3 track system will be equal to the muon mass [72]

$$E_{tot} = \sum E_i = m_\mu = 105.66\,\text{MeV} \tag{2.1}$$

and the vector sum of the decay products momentum should vanish, this would only hold if the muon was at rest.

$$|\vec{p}_{tot}| \;=\; \left|\sum \vec{p}_i\right| \;=\; 0 \tag{2.2}$$

The individual energies of the decay products must be smaller than approximately half the muon mass, as shown in figure 2.1. It also shows that the detector must be able to detect energy across a wide range.

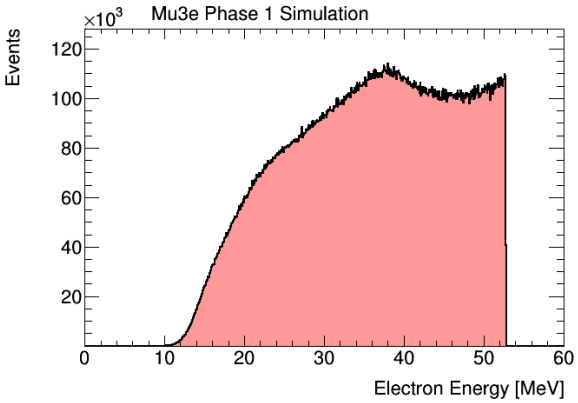

FIGURE 2.1: Distribution of the energy of only the electron after a signal decay, this only shows the number of frames simulated and does not relate to the phase-I rate. This shows that the detector needs to be able to detect particles over a wide range.

Internal Conversion

The decay $\mu^+ \to e^+e^+e^-\nu\overline{\nu}$, known as Internal Conversion, is the main background process that gives the closest signal topology. The branching ratio of this decay is $(3.4\pm0.4)\times10^{-5}$ for p_T of < 17 MeV/c [72]. The method of reduction for this background is to precisely measure the momentum of the decay products, this is because the neutrinos would carry away some energy leading to the total momentum of the 3 electrons being greater than zero and the sum of the energies would not equal that of the muon mass. The visible mass of the 3 electrons from Internal Conversion is shown in figure 2.2(a). This shows that it is possible to get events within the muon mass range, however the fraction of events in this range is close to the sensitivity aim and a good mass resolution is therefore needed. The integrated contribution of Internal Conversion in the signal region is shown in figure 2.2(b) as a function of the mass resolution.

This shows that to reach the sensitivity goal of 10^{-16} at the 2σ level, a mass resolution of 0.5 MeV/c^2 is required [73] [74].

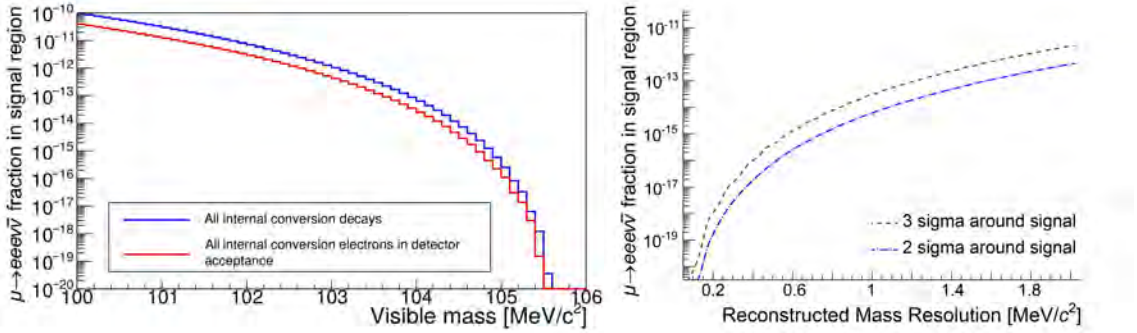

(a) (b)

FIGURE 2.2: (a) The branching fraction for Internal Conversion events, integrated over the total energy as a function of the visible muon mass for all electrons and for those in the detector acceptance [1]. (b) The expected contamination in the signal region with respect to the reconstructed mass resolution [1].

Combinatoric decays

The main decay channel of stopped muons is the Michel decay which has a branching ratio of close to 1 [72]. Due to this decay not producing negatively charged particles it can only contribute to the experiments background if the particle is reconstructed with particles from a different decay. Such as Bhabha scattering or Internal Conversion.

The Bhabha scattering can happen by a Michel positron scattering on a electron inside the target, this produces an e^+e^- pair. Combining this pair with a Michel decay positron can produce a fake signal, see figure 2.3(a). This background has been studied in detail for the TDR [1] for which 2.5×10^{15} muon stops were simulated resulting in 4 reconstructed events of in the mass range 103 - 110 MeV/c^2 and none above 104 MeVc^2 [1]. The second highest combinatoric background is the combination of a e^+e^- pair from an Internal Conversion event with a Michel positron see figure 2.3(b). This was determined internally prior when the TDR work being completed by running a truth level simulation.

Another potential combinatoric background is from photon conversions inside the target region or the inner pixel layers. The photons mainly come from radiative muon decays with a branching ratio of $(3.3\pm1.3)\times10^{-3}$ for photons with energy greater than 20 MeV [72]. Both of these combinatoric background

sources have been studied in chapter 6 and 7 and the method of simulation is also discussed.

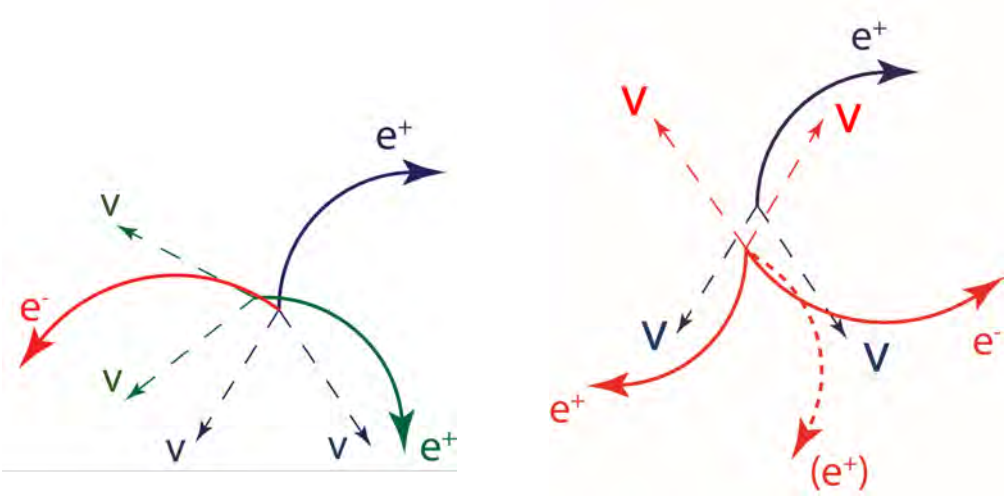

(a) (b)

FIGURE 2.3: (a) Schematic of Michel and Bhabha combination, the blue and green lines indicate Michel decays while the red is the Bhabba electron (b) Schematic of Michel and Internal Conversion combination, the red lines indicate the Internal Conversion particles and the blue is the Michel particles. Adapted from [1].

2.2 Experimental Concept

The Mu3e detector is a high-resolution spectrometer designed for the measurement of low energy electrons emitted from stopped muon decays. The whole detector is placed inside a magnetic field of 1 T, allowing for the momentum of the electrons to be calculated from the curvature of the particle tracks.

A schematic of the detector can be seen in figure 2.4 showing both a longitudinal and transverse projection, these include the tracks of a signal decay. The muon beam is stopped on a double cone shaped hollow target, which is surrounded by 2 High Voltage MAPS (HV-MAPS) pixel layers thinned to 50 μm. There are 2 more layers of HV-MAP pixel chips at a larger radii to increase the detector acceptance and to measure the electron momenta. Precise timing is needed for the reduction of accidental backgrounds. To achieve this, there are scintillating fibres, constructed out of multi-clad plastic fibres, located just before the outer pixel layers. The section of the solenoid that these are located is known as the central station.

Due to the presence of the magnetic field the tracks will form a helix around the detector barrel and pass back into the central station or into 2 other detector stations known as recurl stations, these are upstream and downstream of the beam pipe. Both of these consist of 2 more pixel layers as well as scintillating tiles to provide more timing information.

The coordinate system used in this thesis and in Mu3e is centred in the stopping target with the z axis pointing in the beam direction, the y axis is pointing up and the x axis is oriented to have a right-handed system. The polar angle is donated by θ when measured from the z axis and λ when measured from the x-y plane. The azimuthal angles are denoted by φ.

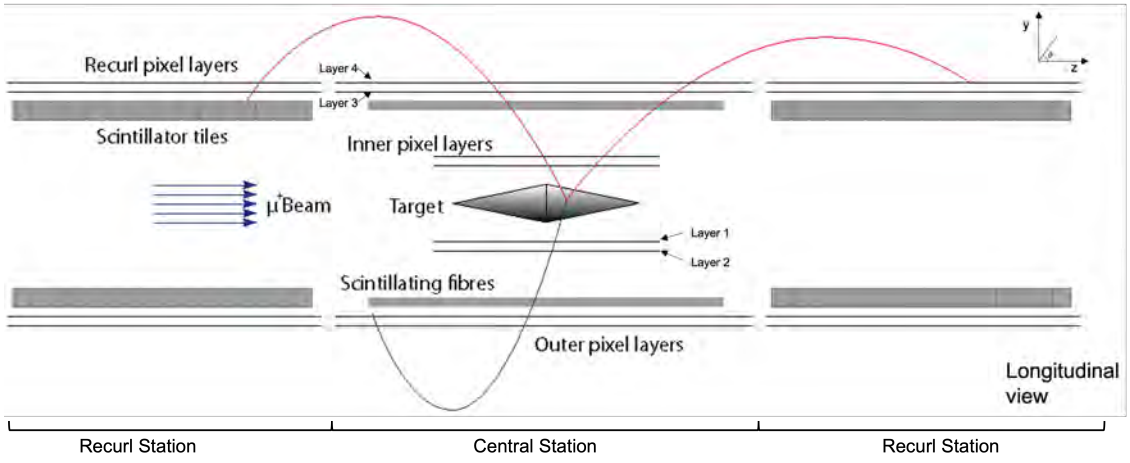

(a)

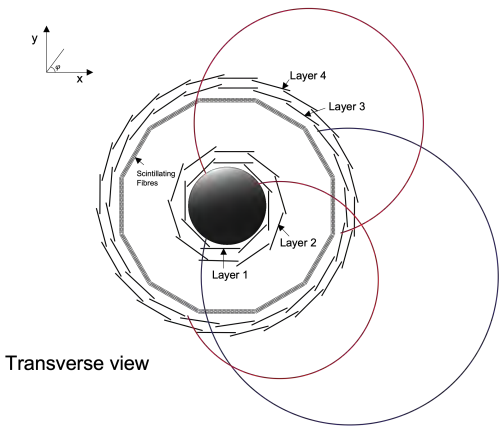

(b)

FIGURE 2.4: Schematic for the Mu3e phase-I detector cut along the beam axis. The tracks [1]

2.2.1 Momentum resolution

Due to the low momentum of the decay electrons/positrons the main source of resolution on the momentum measurement is from multiple Coulomb scattering. If the thickness of the traversed material is small the scattering angle can be described by a Gaussian with a mean of 0, where the standard deviation is given by the Highland formula [75].

$$\sigma_{MS} = \frac{13.6MeV}{p\beta c} z\sqrt{\frac{X}{X_0}}\left(1 + 0.038 \ln \frac{X}{X_0}\right) \propto \frac{1}{p}\sqrt{\frac{X}{X_0}} \tag{2.3}$$

Here p is the momentum, βc is the velocity, z is the charge number of the incident particle and $\frac{x}{X_0}$ is the material thickness in radiation lengths. This leads to a very tight material constraint on the detector design.

The momentum measurement of a track depends on the track angle Ω in the magnetic field and the multiple scattering angle Θ_{MS}. A schematic is shown in figure 2.5. This is a example diagram with 3 detector planes, the first being the double red lines where multiple scattering happens in the second red line, this then changing the track angle for when it gets detected by the 3rd red line. [1]

$$\frac{\sigma_p}{p} \propto \frac{\Theta_{MS}}{\Omega} \tag{2.4}$$

This shows that if we want the right-hand side to be the smallest, we need Ω to be largest, this is when $\Omega = \pi$. This can be achieved by having detectors at a larger radius but with the same position in z, which would however limit the acceptance for low momentum particles. Since all particles are below 53 MeV, particles will follow a complete helix trajectory inside a strong enough magnet. To benefit from this effect Mu3e has a limited number of tracking layers at smaller radii inside a large radius magnetic field.

[1] This equation comes from $\frac{\sigma_p}{p} = \frac{2\sigma_{MS}}{Br}$ where r is the radius of the track.

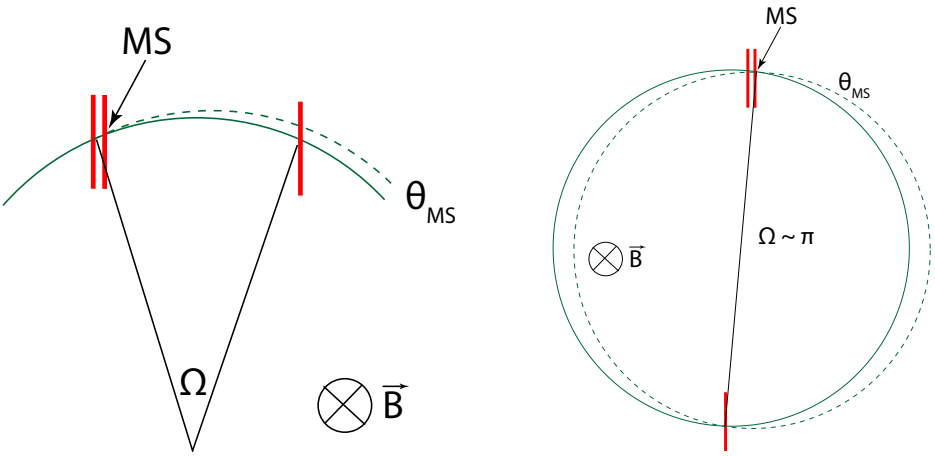

(a) (b)

FIGURE 2.5: (a) Multiple scatting transverse to the magnetic field (b) Multiple scattering for a semi-circular trajectory. These both consist of 3 detector planes indicated by the red lines, the second detector plane is where multiple scattering occurs [1].

2.3 Phase-I Detector

2.3.1 Muon Beam

Due to the Mu3e experiment looking for a extremely rare decay it requires a muon beam with high intensity. To spread the muon decays evenly in time the beam will also run continuously. This allows for a better suppression of combination backgrounds as decay particles will be less likely to be reconstructed at the same time.

The only facility in the world capable of delivering the muon rate needed to achieve the sensitivity aim in a reasonable amount of time is the $\pi E5$ beam line at PSI, which provides a rate of close to 10^8 muons/s. This beamline is shared with the MEG II detector which is permanently located in the rear part of the $\pi E5$ area. Due to space limitations a 3.2 m compact muon beam line (CMBL) has been designed to fit into the front of the $\pi E5$ area, this is shown in figure 2.6.

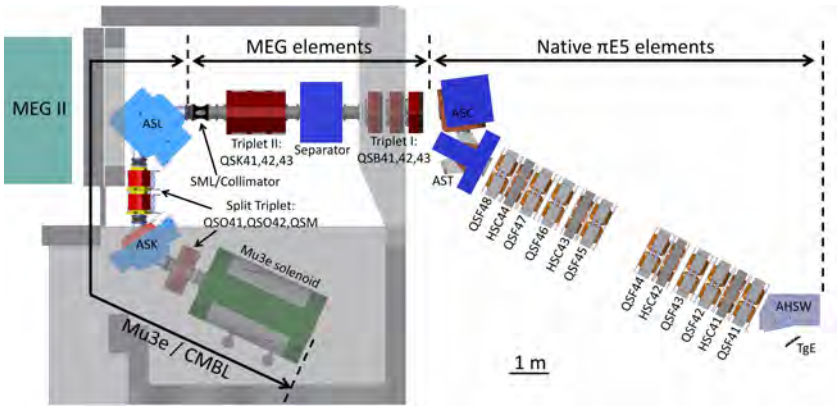

FIGURE 2.6: CAD model of the $\pi E5$ beam line along with the CMBL. [1]

The beamline works by first firing a beam of 590 MeV protons at a graphite target named target E, this generates pions inside the target. The pions at the surface decay into muons that are 100% polarised with a momentum of around 28 MeV [76]. Due to alternative pion decays as well as muons decaying around TgE there is a large contamination of electrons and positrons in the beam. A ±200 kV Wien filter (E × B field separator) is used to remove this contamination. Tests performed in 2018 yielded $1.1{\times}10^{8}\mu^{+}/s$ at 2.4 mA proton current at the injection point of the Mu3e solenoid. The contamination of positrons without a Wien filter was measured to be $e^{+}/\mu^{+} = 10.4$, with the Wien filter on this was reduced by a factor of 15. Further upgrades to the Wien filter have not yet been measured, however it is expected to reduce the contamination by 3 orders of magnitude. This new Wien filter is already in the beam line.

2.3.2 Magnet

The magnet for the Mu3e experiment needs to provide a homogeneous magnetic field for precise momentum measurements as well as serving as a beam optical element. The magnetic field strength for the experiment is 1 T parallel to the beam line. The magnet will also act as a sealed volume for the Mu3e detector while the outside of the magnet includes an iron return yoke to reduce stray fields at a distance of 1 m down to 5 mT.

2.3.3 Target

The stopping target is optimised to stop the muons with minimal losses, spread the decay vertices out as far as possible and minimise material encountered by the positrons and electrons from the muon decays. It is also advantageous to use a low Z-material as this will suppress photon conversions and large angle coulomb scattering.

The design of the target is shown in figure 2.7(a), it is a hollow double cone constructed out of Mylar. This is the same target design that was used in SINDRUM [49]. Other target designs were considered however for the given beam parameters and geometric constraints none provided higher stopping fraction with equal or less material. The total thickness of the target is 422 μm which corresponds to a radiation length of 0.15%. A prototype has been constructed and can be seen in figure 2.7(b).

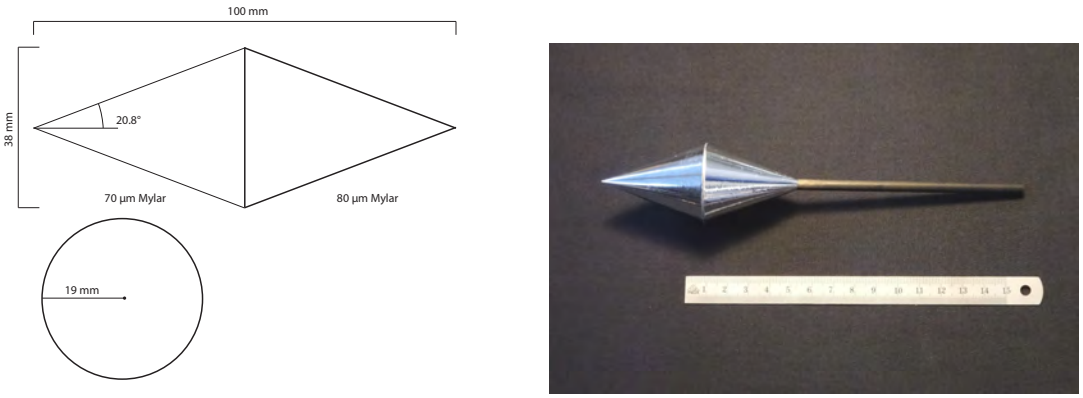

(a) (b)

FIGURE 2.7: (a) Dimensions of the stopping target, the muon beam will enter from the left (b) First prototype of the target. [1]

The target will be supported by a carbon tube glued to the downstream end of the target. Due to the length of this tube, it has a rear end support and a joint near the target to prevent vibrations down its length. From the downstream side end the target can be adjusted in all 3 dimensions using adjustment screws with a limited range to protect the inner pixel layers.

2.3.4 General Layout

The Mu3e detector is divided into 3 sections, a central station and 2 recurl stations. The central station is where the beam collides with the target, the resulting tracks first pass through 2 layers of silicon pixel detectors. These layers

are key to the vertex location. The tracks will then pass-through scintillating fibres for the timing information and through 2 more pixel layers. Due to the magnetic field the particle tracks recurl back towards the beamline, and get detected again, in either the central station or by 2-pixel layers in the recurl stations before arriving at the scintillating tiles.

2.3.5 Timing detectors

To reduce combinatoric background processes a timing system has been developed allowing for the identification coincidental tracks. The system consists of a scintillating fibre hodoscope around the central part of the detector, these are constructed out of multiclad fibres from Kuraray, type SCSF-78MJ. There are two scintillator tile detectors located at both recurl stations, these tiles are constructed out of EJ-228 plastic scintillator.
Both subsystems employ silicon photo multipliers (SiPMs) for the readout of the scintillation light as these are compact, insensitive to the magnetic field, feature high photon detection efficiency and provide the accurate timing response needed. Both detectors use a custom frontend chip, MuTrig, which has been designed to readout the timing detectors with the desired resolution while also maintaining the high rate needed for Mu3e.

Fibre Detector

The purpose of the fibres is to measure the particles' timing with a resolution of 1 ns while minimising the amount of material in the path of the particles. The fibre detector also needs to have a high granularity to cope with the rates of the experiment.
A CAD drawing of the fibre system is shown in figure 2.8. The fibre modules will consist of three layers of 250 μm diameter scintillating fibres, arranged just inside the outer pixel layer at a radius of 6 cm from the central axis. This leads to SiPM 3072 channels. The fibres are connected to multi-channel SiPM arrays collecting the light from several fibres.

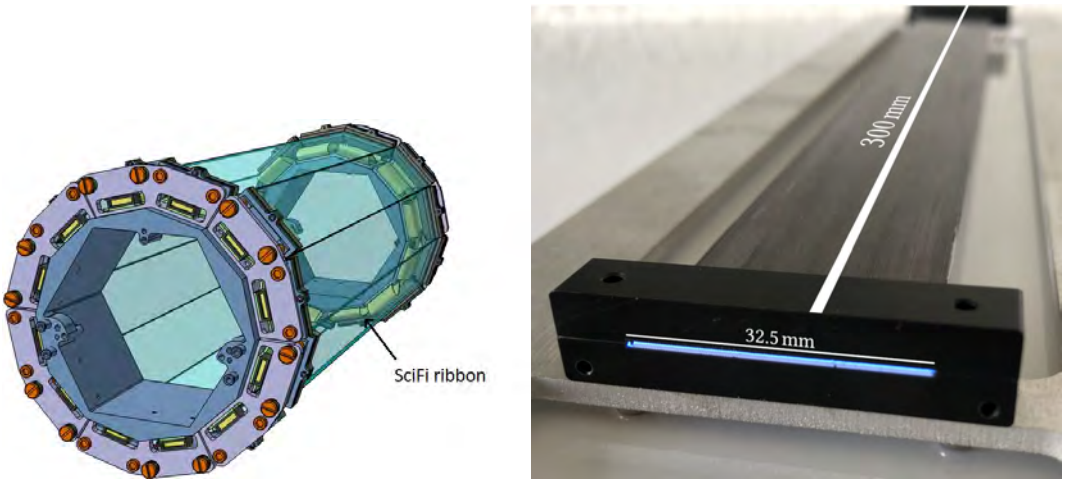

(a) (b)

FIGURE 2.8: (a) CAD diagram for the scintillating fibre detector with each fibre ribbon shown (b) Prototype fibre ribbon made from 3 layers of fibres with a preliminary holding structure [1].

Tile Detector

The aim of the tile detector is to measure the timing of the particles to a precision of 100 ps with an efficiency close to 100%. This is feasible as the tiles don't have the same material constraints as the rest of the detector.

Each recurl station will consist of 3360 tiles at a radius of 6.3 cm from the central axis, organised into modules with 416 tiles each as shown in figure 2.9. Each tile consists of a plastic scintillator cube glued to a SiPM soldered to a readout PCB.

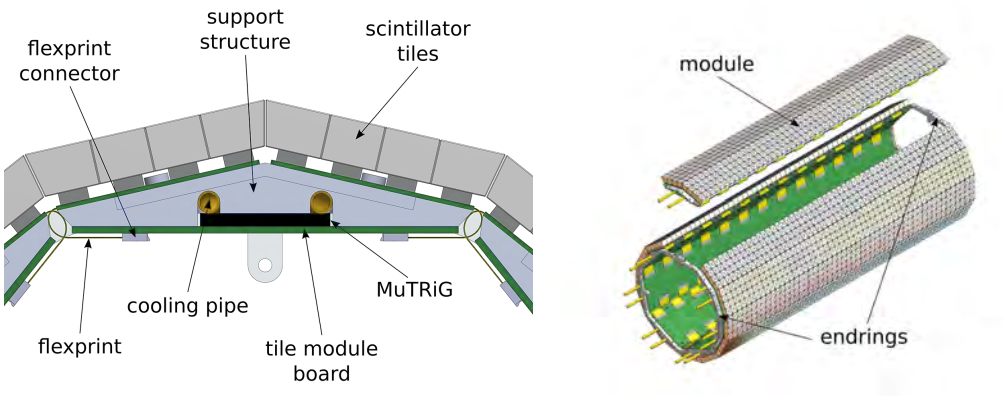

(a) (b)

FIGURE 2.9: CAD drawing for a scintillating tile submodule with (a) showing a transverse cut out and (b) showing the full detector [1]

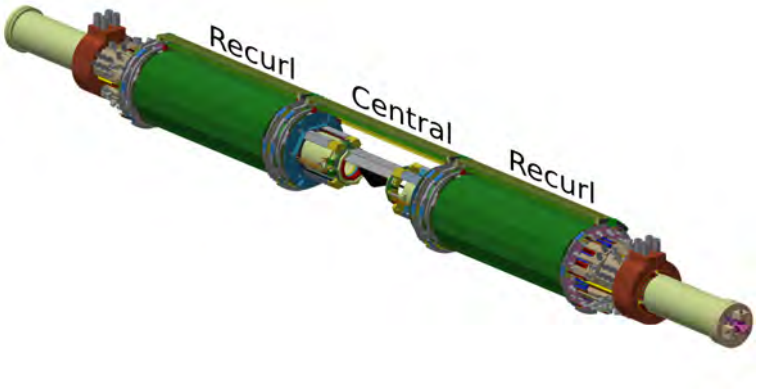

FIGURE 2.10: The pixel tracker with the central and recurl stations labelled, some tracker modules are removed to improve visibility

2.3.6 Pixel detector

The pixel detector for the Mu3e experiment is designed to provide particle track reconstruction for vertex reconstruction and momentum measurement. It is designed to achieve the best possible momentum and vertex resolution required to achieve the sensitivity of the experiment. To be able to achieve this there is a strict material budget in the detector, as the dominating error in the experiment is multiple scattering. For this reason, High Voltage Monolithic Active Pixel Sensors (HV-MAPS) will be used and thinned to 50 μm, known as MuPix. These chips are then mounted to a low mass flex circuit for powering and readout. Further details on the tracker and the chip can be found in chapter 4.

Tracker Layout

The tracker consists of 3 parts, the central station and 2 recurl stations, as shown in figure 2.10. The detectors of the central station provide the main hits for track and vertex reconstruction while the recurl stations improve momentum resolution.

The central tracking station consists of 2 inner and 2 outer pixel layers. The central station geometry is shown in figure 4.1 and the design parameters listed in table 2.1. The recurl stations consist of only layer 3 and 4.

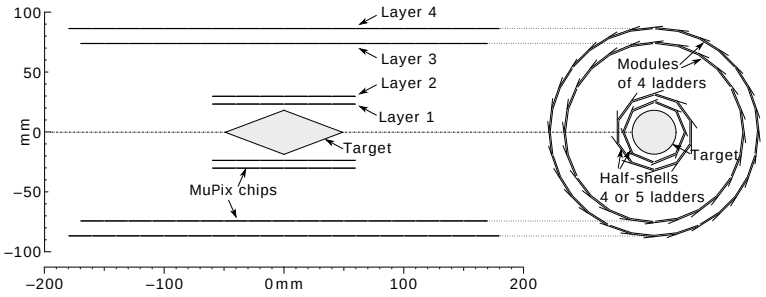

FIGURE 2.11: Geometry of the central pixel station

layer	1	2	3	4
number of modules	2	2	6	7
number of ladders	8	10	24	28
number of MuPix sensors per ladder	6	6	17	18
instrumented length [mm]	124.7	124.7	351.9	372.6
minimum radius [mm]	23.3	29.8	73.9	86.3

TABLE 2.1: Pixel tracker geometry of the central barrel, taken from [1].

Helium cooling

The pixel detector will be cooled by gaseous helium to minimise the material in the active region. The maximum operating temperate of the HV-MAPS pixel sensors is 70 °C and a total power consumption of the full pixel tracker is 4.55 kW. The Helium cooling system is designed to remove this heat.
This will be discussed further in chapter 4.1.

2.4 Reconstruction and Simulation

2.4.1 Data Acquisition

All sub detectors for the experiment will stream data continuously to the data acquisition system without the need for a hardware trigger. A complete schematic of the readout system is shown in figure 2.12 [77, 78].

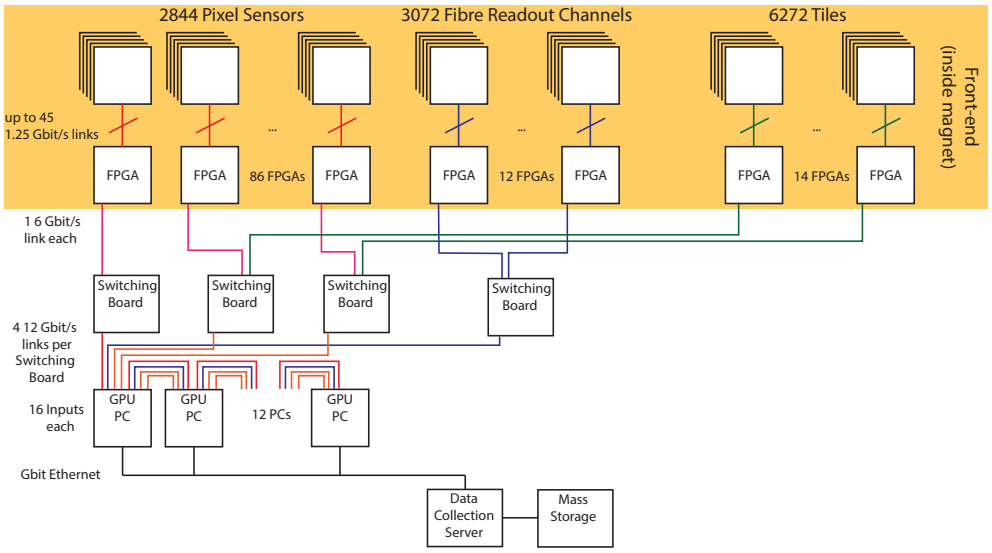

FIGURE 2.12: Schematic of the Mu3e readout scheme [1].

Front End and Switching Boards

All sub detectors will provide zero-suppressed hit information to the front-end boards, each hit provides a time stamp as well as the position which is known from the input channel of the front end board. The pixel chips also provide extra information of the address of the hit pixel.

The pixel detectors will provide continuous data even when there are no hits, this includes status information and fixed data patterns for no hits. The fibres work differently as it is expected that a particle will produce signal in several fibres, these need to be clustered together, which is done on the front-end boards. Four switching boards will be used, one for the central station pixels, one for the fibres and 2 for the recurl stations. In these switching boards data from the multiple front-end boards will be merged, time ordered and merged into time slices, known as frames, allowing for the filter farm to access all detector information for a given time slice.

Filter Farm

The filter farm will consist of 12 PCs, each of which is equipped with a FPGA board to receive the information from the switching boards. Each of these computers are daisy chained together so if the first one is busy event frames are passed to the next one. The hits are then transformed to a global coordinate system and some simple geometric selection criteria are performed to reduce

the number of potential combinations. This data is then copied to the GPU where fast track and vertex reconstruction is done. Time frames with a good 3 track vertex are then saved to disk for offline analysis. The reduction of this fast reconstruction stage in data rate is from 80 Gbit/s to 100 MB/s and saved to mass storage [77]. The estimated data storage needed is 1 PB.

2.4.2 Online Reconstruction

Due to the experiment readout being triggerless all the muon decays need to be fully reconstructed online, this puts a high demand on the speed of the reconstruction algorithms. To this end a new fast track reconstruction algorithm was developed for when track uncertainties are dominated by multiple scattering in the detector planes [79]. This was done as the standard track fitting algorithms, such as Kalman filters [80], require a lot of computing power and time to fit Mu3e tracks due to the high muon rate. Due to the low momentum of the tracks in a magnetic field the particles do not form a straight line. This increases the number of combinations possible for each particle.

The tracking algorithm used in Mu3e works by assuming that there is no energy loss between planes and that the spatial uncertainties are negligible, it also assumes that the errors from multiple scattering are small meaning that the track should always be a helix. This is because MuPix has a spatial resolution of 25 μm, which is a great deal smaller than the multiple scattering uncertainties. These assumptions mean that the trajectory in a magnetic field can be fully described by knowing the 3 hit (minimum number of hits to define a trajectory) positions and the curvature of the track. To describe this scenario better the trajectory consists of 2 helices with a kink at the middle hit. This fit is then described by the trajectory that minimises the χ^2

$$\chi^2(r) = \varphi^2_{MS}(r)/\sin^2(\theta) + \Theta^2_{MS}(r), \tag{2.5}$$

where θ is the helix polar angle. This is non-linear and doesn't have an analytic solution but can be linearised around a known solution such that φ_{MS} and Θ_{MS} are linear functions of the curvature r.

For tracks with more than 3 hits the track is divided up into multiple triplets and combined. The solution to minimise the track χ^2, is the weighted average of

the individual solutions. In the experiment the online reconstruction will make tracks with 4 hits, which are known as short tracks throughout this thesis. These tracks are used to reconstruct the vertex, this involves cycling over all combinations of 2 positive and 1 negative charge tracks and using an iterative linearised method to fit the vertex. For the offline reconstruction the short tracks can be extended to form long tracks with either 6 or 8 hits. Long 8 hit tracks are tracks that make one full turn in the central station. Long 6 hit tracks are a 4 hit tracks and a pair of hits in the outer layers, this can be either in the central or outer station. Due to the cancellation of the multiple scattering errors, the momentum resolution for long tracks is much better than that for short tracks, as shown in figure 2.13. The shape of the long tracks is due to Coulomb scattering getting less dominate until the momentum of the particle starts to take effect, this results in a minimum around 20 MeV/c. Fake tracks for 6 hit tracks is around 5%, for 4 hit tracks around 1% and for 8 hit tracks it can reach the same level as truth tracks. This high fake rate is due to the particle making several turns in the magnetic field. The other fake tracks can come from combinations of hits from different tracks while the rest from hits from the same tracks but different turns in the detector. These can be reduced by selecting the inclination angle. The noise rate of pixel is 0.1 Hz per frame, this corresponds to one hit, thus is negligible.

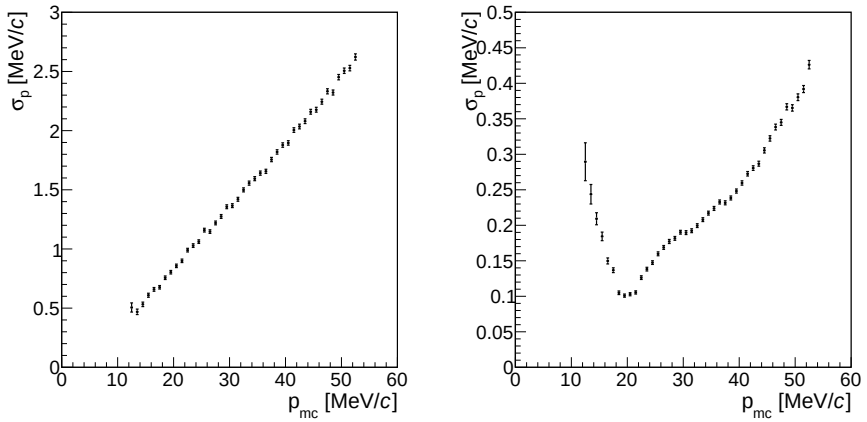

(a) (b)

FIGURE 2.13: (a) Momentum resolution of short tracks (b) Momentum resolution of long tracks as a function of total momentum. The momentum resolution is at a minimum when the track recurls through exactly half a circle. [1]

2.4.3 Simulation

The simulation is used to optimise the detector design, estimate background levels and develop the reconstruction code. It is based on Geant4 [81–83] and is described below.

Detector Geometry

The simulated detector geometry follows the planned geometry closely. The simulated region extends 3 m in all directions from the target. A detailed Geant4 CAD schematic is shown in figure 2.14.

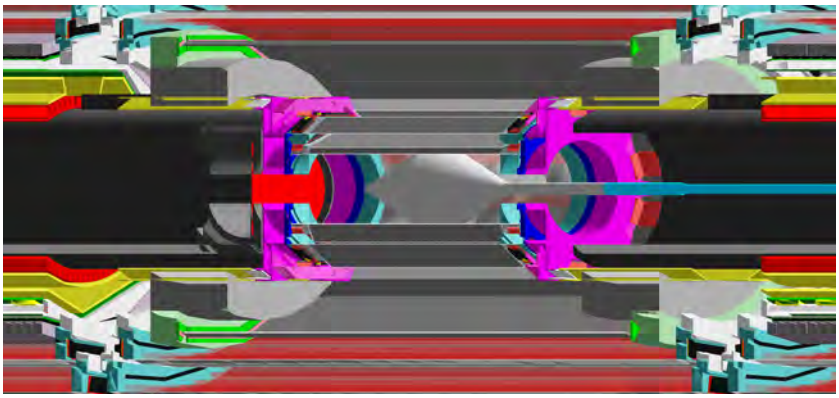

FIGURE 2.14: Geant4 diagram of the simulated detector region focusing on the centre region and cut open at x= −19.5 mm

The simulated beam starts 1 m in front of the target and is generated with a beam profile based on beam measurements at the same point. It then passes through a Mylar moderator followed by a lead collimator which removes larger scattering angles before exiting the beam vacuum through a 35 μm Mylar window. The beam then collides with the target with its support structure also simulated.

The pixel sensor is simulated in detail with the end pieces and support wheels. The ladders themselves have the sensor support structure and the flex print simulated. The fibres are simulated to include the shape, thickness, support structure and staggering. The parameters of the fibre ribbons can be easily changed with the base configuration being 12 ribbons in 3 layers. The tiles also have a full simulation of the scintillating tiles, Silicon Photo-Multipliers, PCBs hosting the Silicon Photo-Multipliers, the readout chips and support structure.

Physics Processes

In the Mu3e experiment the muon decays are generated by first pseudorandomly, to allow for generation with the same random seed in future, generating the 4 momenta of the decay products in the rest frame, these are distributed in the phase space according to the simulation process. The generated particles are then propagated through the detector and the response is simulated. It also simulates interactions with matter such as energy lose due to ionisation, bremsstrahlung etc.

The Michel decay simulation, with the polarisation of the muon in GEANT4, is based on Scheck and Fischer [84, 85]. The radiative decay in Geant4 was implemented by the TWIST collaboration based on Fronsdal [86]. In the Mu3e simulation the differential branching fraction in energy and solid angle by Kuno and Okada is used [87]. The Internal Conversion decays are simulated with the general matrix element by Signer et al. [88].

The signal decays have been generated using 3 particle phase space distributions, this is the same procedure as used by SINDRUM. The general matrix elements by Kuno et al [88] have been implemented.

The simulation software also has the ability to generate multiple muon decays at a single point or in a fixed length time frame, to allow for the study of combinatoric backgrounds.

2.5 Upgrades to the Mu3e detector

2.5.1 Phase-II of the Mu3e experiment

A new high intensity muon beam line is under development at PSI, which will deliver a rate of $>2\times10^9$ Hz muons on target [89]. To exploit this higher rate the Mu3e detector would need to be upgraded. In the baseline design, two new recurler stations would be constructed and placed upstream and downstream, see figure 2.15. This allows for precision measurements of the momentum of all tracks in the acceptance as well as the precise timing needed to reduce the combinatoric backgrounds due to the high rate of muon decays. It will also increase the acceptance of long tracks.

Due to the higher rate the beam can be collimated better, this allows for a small and longer target leading to better vertex spread. We could also make use of the timing resolution of improved HV-MAPS, thus reducing the material budget in the active region as the fibre detector could be removed entirely.

With this added rate and the detector modifications the experiment can reach its target sensitivity of $\mathrm{B}(\mu \to eee) \leq 10^{-16}$.

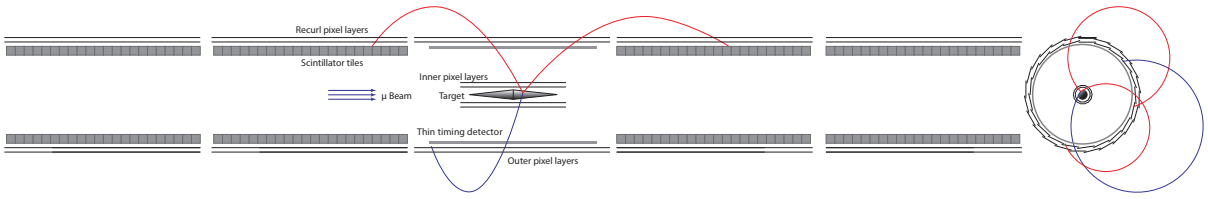

FIGURE 2.15: Potential design of phase-II of the Mu3e detector

2.5.2 The Mu3e-gamma experiment

Further uses of the Mu3e detector have also been considered, one potential option is to search for the CLFV decay $\mu^+ \to e^+\gamma$. The positron can be detected by the current Mu3e detector while the photon could be detected by electron-positron pair production. To allow this to happen another detection station needs to be constructed at a larger radius consisting of a photon converter, 2 layers of pixels and a timing detector, this can be seen in figure 2.16. It is also foreseen to have a magnetic field of 2 T meaning no decay positrons can reach the photon detection layers at higher radii [90].

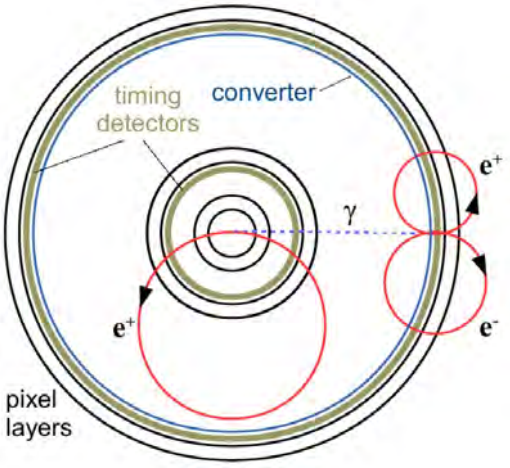

FIGURE 2.16: Diagram for the Mu3e-γ experiment in the transverse plane with the muon beam going into the page.

Chapter 3

MuPix Sensor and Testbeam

Due to the very strict material limit in the detector, conventional hybrid pixel chips are not suitable for the Mu3e experiment. Only monolithic sensors can fulfil this limit, these integrate the readout onto the sensor chip. For the Mu3e detector High-Voltage Monolithic Active Pixel Sensors (HV-MAPS) have been chosen with a custom chip, known as MuPix, being designed. A number of prototypes have already been designed and tested with the first large scale chip being MuPix8. The chips are tested in testbeam campaigns using a dedicated MuPix telescope.

This chapter describes the basic principle of HV-MAPS before talking about the performance of recent prototypes. It will then go on to describing the MuPix telescope and results from the October 2019 testbeam at PSI. This testbeam used 4 layers of MuPix chips, 3 reference planes consisting of 200 Ωcm MuPix8 and the DUT (Device Under Test) layer. The chips tested in this testbeam are MuPix8 and 9. The MuPix8 scans performed were threshold scans while varying the supply voltages. The MuPix9 scans were threshold scans with varying amplifier voltage.

3.1 MuPix and the MuPix Telescope

3.1.1 HV-MAPS

Traditional monolithic active pixel sensors (MAPS) include a full readout mechanism and collect charge by diffusion from a depleted layer of a few 10s of micron thickness. This means that most of the substrate is inactive and can be thinned away. The new ALICE tracker will use this technology in its inner tracker [91].

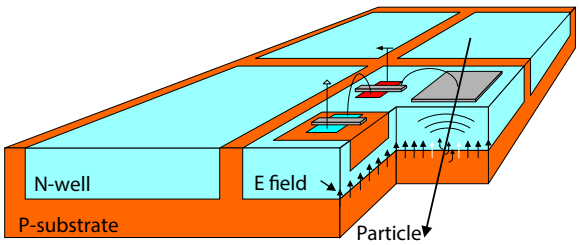

FIGURE 3.1: Sketch of the HV-MAPS detector design [92].

One of the main issues with MAPS is the relatively low speed and time resolution. This can be overcome by utilising commercial HV-CMOS processes to create HV-MAPS. These chips collect ionisation charge by drift rather than by diffusion allowing for a time resolution of a few ns. In the MuPix chips, the amplification of the signal happens inside the pixel cell while the readout electronics are located at the chip periphery. The limited depth of the depletion zone also allows for these chip to be thinned, to as little as 50 μm. The use of HV-CMOS technology for particle detection was first proposed in Ref [92].

3.1.2 Prototypes

There have been a number of prototype HV-MAPS sensors (MuPix) developed for Mu3e to develop all the necessary elements for the final detector chip. The most recent iterations are discussed here.

MuPix8

MuPix8 was the first large scale prototype with a size of 10.8×19.5 mm^2. It includes all the main features that are required for the final detector chip and consists of 128×200 pixels, each with a size of 81×80 μm^2, read out by their own digital cell in the periphery. The chips are divided into 3 sub matrices (A,B,C) each with their own state machine. A state machine is what governs the internal readout of the cell. The chip has been manufactured on 80 Ωcm and 200 Ωcm resistivity substrates to increase the depletion zone with respect to previous prototypes. The layout of MuPix8 can be seen in figure 3.2.
The analogue pixels of the chip consists of a deep n-well containing the electronics. This well is implemented in a p-substrate thus forming the sensor diode while the logic inside the n-well is unaffected. The signal that is induced inside

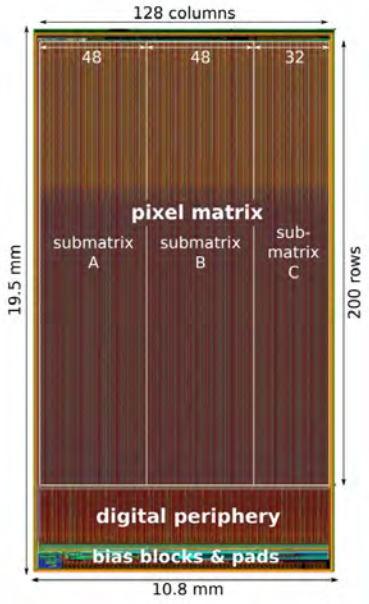

FIGURE 3.2: The layout of MuPix8. The different sub matrices are shown and the number of rows and columns.

the pixel is amplified and then driven to the digital cell by a source follower for matrix A and current mode transmission for matrices B and C.

The digital cell takes the analogue signal and digitises it. For matrices B and C a receiver cell converts the current signal to a voltage one while matrix A doesn't need a receiver cell. It is then passed through a comparator converting it to a logic signal which raises the hit flag and stores a timestamp if the signal is above threshold. Timestamps and associated pixel addresses are read out following a column parallel approach.

Various test beam campaigns and laboratory tests have been performed to characterise the chip [93–95]. The chip was first commissioned in September 2017 and was fully functional. The efficiency of the 80 Ωcm substrate chip with a bias of −60 V is shown in figure 3.3(A). This shows that the chip has a 20 mV wide plateau where the efficiency is greater than 99.9%. Another aspect that can be investigated with MuPix8 is the effect on efficiency with different depletion zones. The 2 substrates that have been manufactured have been tested with the same bias voltage of 50 V, this is to compare how the efficiency changes with depletion depth. This is because the depletion depth, thus the efficiency, is dependent on the bias voltage and the resistivity on the chip. Another useful test is to vary the bias voltage while keeping the resistivity then same (200 Ωcm) to confirm the drop off in efficiency as bias voltage decreases. Both of these

observed behaviours is consistent with the theory that the depletion zone, thus the efficiency, depends on the resistivity and bias voltage.

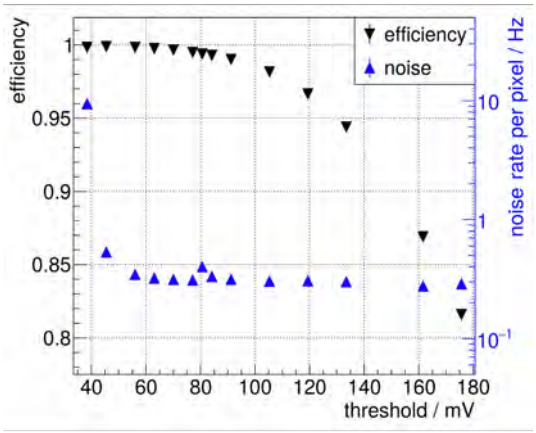

(a)

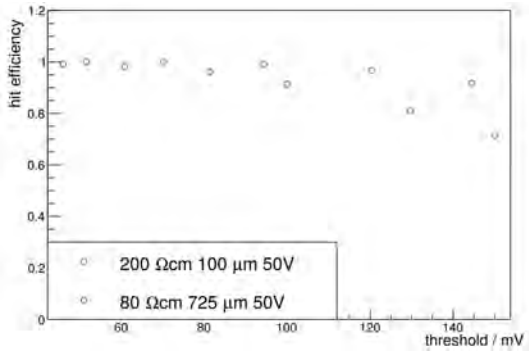

(b)

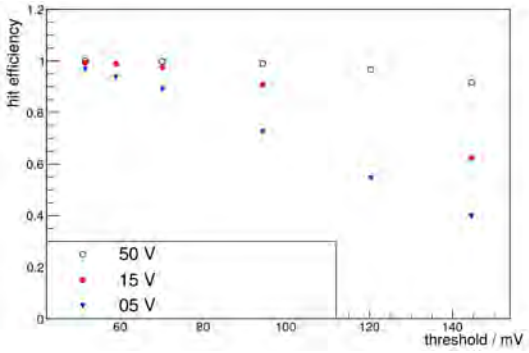

(c)

FIGURE 3.3: MuPix8 efficiency plots (a) Efficiency plot with a bias of −60 V using a 80 Ωcm resistivity chip thinned to 62 μm (b) Comparing the efficiency of different substrate resistances (c) Comparing different bias voltage for the same substrate. [1]

MuPix9

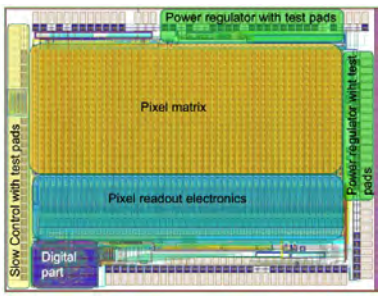

FIGURE 3.4: The layout of MuPix9 with different sections highlighted.

The MuPix9 chip is a small prototype made on a substrate of 20 Ωcm resistivity and a size 4.7×3.6 mm^2. It hosts 48 columns, each with 20 pixels. The main purpose of this chip was to test additional circuits for power regulation that are needed for chip integration in a larger detector. The pixel matrix is a condensed version of the MuPix8 matrix A with some small changes. The main change is that it now has a NMOS amplifier while MuPix8 had PMOS. The readout cells are modified to allow for serial powering. Another aspect changed is that the power distribution for the digital and analogue cell are separated allowing for each to be tested separately.
A testbeam campaign has been performed with this chip and is discussed in this thesis.

MuPix10

The MuPix10 chip is intended to be the final prototype chip, it consists of 3 sub matrices each with their own state machine. The sub matrices consist of 42, 43 and 43 double columns, respectively, leading to a total of 256 pixel columns and 250 pixel rows with a pixel size of 80×80 μm^2. A schematic layout of MuPix10 is shown in figure 3.5. The main difference of note from MuPix8 is that all the matrices are now the same. MuPix10 also includes power regulation to allow for one input voltage from which all other voltages are generated. In addition, modifications have been made to the routing of the analogue signals from the pixels to reduce crosstalk. MuPix10 has been tested and results show a reduction in cross talk and equal efficiency compared with MuPix8. It also allows all the powering from a single 1.8 V supply voltage. MuPix11 is of a very similar design with only some minor fixes and was submitted in January 2022.

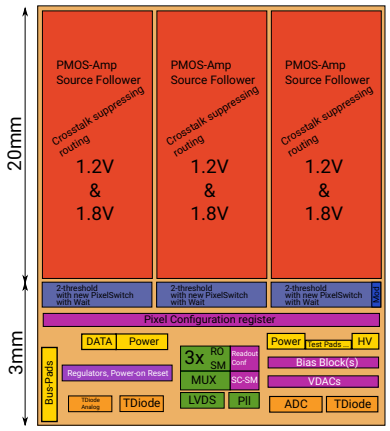

FIGURE 3.5: The schematic layout of MuPix10 with labelling and locations of properties.

3.1.3 The MuPix Telescope

The MuPix telescope is a set up used to test MuPix chips in test beams, it is a custom-made set-up using 4 planes connected to a FPGA inside the DAQ computer, its design allows for multiple telescopes to be placed in a single line. [96]. The MuPix telescope readout can stream data without any hardware trigger while using a scintillating detector at each end to get a time reference. The coordinate systems used within the MuPix telescope can be seen in figure 3.6. The beam direction is along the z axis and the x goes along the columns. The $\pi M1$ beam line at PSI consists of pion, electrons and muons with a total beam energy of 270 MeV.

For the use of tracking algorithms with respect to the MuPix telescope some simplifications can be used. The tracks do not pass through a magnetic field. The energy loss per layer is low, and therefore not considered. All possible tracks are considered and fitted. If there are multiple hits in one of the layers then the track with the lowest χ^2 is taken.

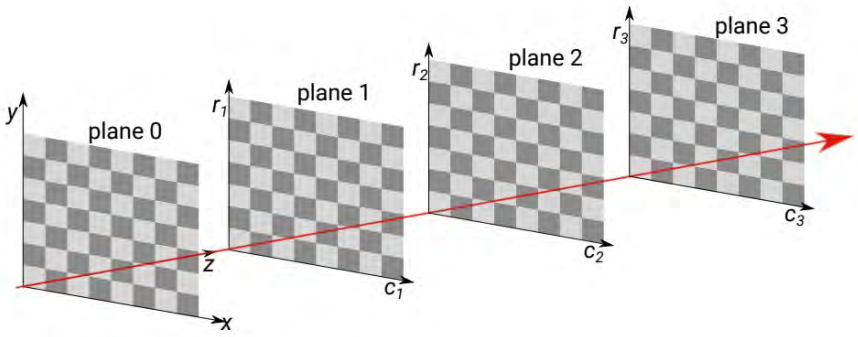

FIGURE 3.6: Sketch of the coordinate system for the MuPix telescope, the particle beam is shown in red. The global coordinate system (x,y,z) is defined by layer 0 and the local cordiante system (c,r) is shown for other layers [97].

Track Reconstruction

The tracking model used for the MuPix telescope is a straight line fit.
The straight line fit doesn't take into account multiple Coulomb scattering and is thus simply described by

$$\boldsymbol{f}(z) = \boldsymbol{a} + \boldsymbol{s} \cdot z \tag{3.1}$$

The full track reconstruction has not been used due to simplifications, such as no magnetic field, can be done thus speeding up the track reconstruction. Where z is the z position in the global coordinate system, **a** is the initial (x,y) position in the global coordinate system at z = 0 and **s** is a two dimensional slope. The uncertainties on the measurement of x and y are typically (pixel size)/$\sqrt{12}$. This is for single hits only; the error would be reduced for particles that fire more than one pixel. The main advantage of this method is that it is non iterative and thus can be implemented fast. However, the resulting precision of the reconstructed trajectory is less than tracking models that take into account multiple scattering, such as the general broken line fit.

Device under Test Studies

The device under test (DUT) is the chip plane under examination and is used to characterise chip prototypes, this is only one chip in the MuPix telescope and is normally the second chip in the line. A track is based on hits in the other

layers of the telescope and an extrapolated position in the DUT is matched to recorded hits by defining a matching radius. The matching radius draws a circle with the radius around the track which passes through the DUT, if there is a hit inside this radius it is matched to the track. If there are multiple hits non is matched. Any rotations of the DUT are corrected for by minimising the residual distributions and if there are multiple hits within the matching radius the closest one is taken.

Efficiency

The efficiency of the sensor is estimated by taking the total number of matched tracks, which are tracks that have been linked to a hit in the DUT (k), over the total number of tracks that pass through the DUT (N).

$$\epsilon = \frac{k}{N} \tag{3.2}$$

The uncertainty on these measurements can be taken as a positive outcome of a Bernoulli trail leading to the posterior

$$P(\epsilon|k, N) \propto \epsilon^k (1-\epsilon)^{N-k} \tag{3.3}$$

This is due the prior being set to 1. This leads to the uncertainty of the efficiency to be Δx fulfilling a confidence interval of 1σ.

$$\frac{\int_x^{x+\Delta x} \epsilon^k (1-\epsilon)^{N-k} d\epsilon}{\int_0^1 \epsilon^k (1-\epsilon)^{N-k} d\epsilon} = C.L. \tag{3.4}$$

This calculated efficiency can be influenced by noise, for instance if the noise rate is high it can lead to higher efficiencies. This potential influence on the measured efficiency can be defined as

$$\epsilon_m = \epsilon_k + (1-\epsilon_k)\epsilon_n \tag{3.5}$$

ϵ_n is where the probability to match a noise hit

$$\epsilon_n = \frac{\pi r_{cut}^2}{A_p} n_p t_{window} \tag{3.6}$$

n_p is the average noise rate per pixel, A_p the area of a pixel, r_{cut} is the maximum matching radius and t_{window} is the time window to search for matching hits [97].

Noise

It is not unusual for hits in the DUT not to be assigned to a track, this is known as noise, and it is needed to be accounted for when examining the efficiency of the chip. These hits come from 2 possible sources, beam related backgrounds and sensor noise. The beam related backgrounds come from particles that are not reconstructed as tracks due to misalignment or inefficiencies or scattering at large angles in the reference layers. Sensor noise can originate from leakage currents in the sensing diode or noise in the circuity. To measure the average pixel noise, we define

$$n_p = \frac{n_{hits_{nm}}}{N_p \Delta t} \tag{3.7}$$

This uses the number of non-matched hits $n_{hits_{nm}}$, the number of pixels N_p and the runtime. This is an overestimate of the noise because clustering, geometrical acceptance and tracking inefficiencies are ignored.

The first effect is clustering and cross talk, these are treated together as they both cause more than one pixel to fire when a particle traverses the chip. To deal with these effects, clustering algorithms are used. All hits that share an edge (of the pixel) or corner (of the pixel) are grouped together, to make a cluster. This cluster is then treated as one single detection point and individual hits in the cluster are discounted from the noise. To include this effect the variable $n_{hits_{nm}}$ needs to be replaced with $n_{cluster_{ROI}}$

The second effect is the geometrical acceptance this is when particles scatter from outside the reference systems into the DUT layer. This effect is larger when the reference chips are the same size as the DUT layer. This can be alleviated by defining a region of interest so that the most affected edge regions of the DUT are removed.

If two particles travel close together in space and time but not share a pixel edge, they create a hit if in different columns, however if they fire a hit in the same column the one with the lowest address is saved. The final effect is inefficiencies in the reference planes, this leads to some particles not being matched to hits

FIGURE 3.7: Picture of the set up from a testbeam campaign in October 2019 at PSI.

in the reference planes and the number of missed tracks can be defined as,

$$N_{missed} = \frac{N}{\epsilon_t} - N \tag{3.8}$$

where N is the total number of reconstructed tracks and ϵ_t is the tracking efficiency. This leads to a more precise noise calculation of the form [97]

$$n_{pROI} = \frac{n_{cluster_{ROI}} - N_{missed}}{N_{pROI}\Delta t} \tag{3.9}$$

MuPix Telescope hardware

The MuPix telescope requires several hardware components. The MuPix chips are mounted onto an insert and are then mounted to a motherboard. This motherboard has a cut out to not interfere with the particle tracks. The motherboard is secured to a metal frame on a precision x and y stage. The motherboard has all the electrical connections for the chip and is connected to the computer using a StratixIV FPGA development board [98]. An image can be seen in figure 3.7.

3.2 MuPix8 Studies

3.2.1 Alignment

The MuPix telescope is aligned in 2 ways, the first is a mechanical alignment up to a precision in the order of 150 μm by using micrometer screws. There is

then a software-based alignment to correct it further as well as accounting for rotation around the beam axis, this is done by minimising the χ^2 of tracks. For MuPix8 the residuals in x and y in the DUT layer are shown in figure 3.8. The DUT layer is not included in the tracking. To confirm if rotations are correctly removed the mean residuals in x and y are studied as a function of the row or column number and a profile is plotted. This will show any rotations around the z axis as well as the uniformity of residuals across the whole chip. These are shown in figure 3.9. The flat profile at the centre of the chip shows that the rotations are accounted for, and the residuals follow the same trend throughout the chip. The edge effect of these is due to scattering from outside the telescope.

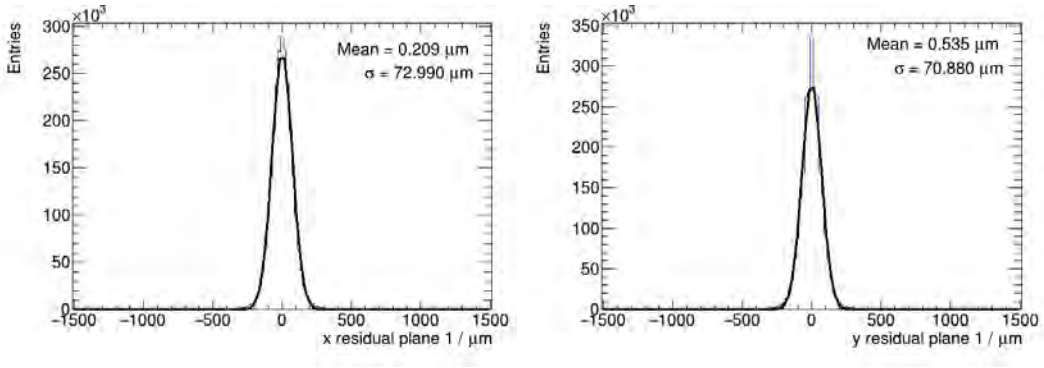

(a) (b)

FIGURE 3.8: Residual plots for MuPix8 DUT layer for both x (a) and y (b). The distribution has been fitted with a Gaussian and the mean and standard deviation is shown on the plot.

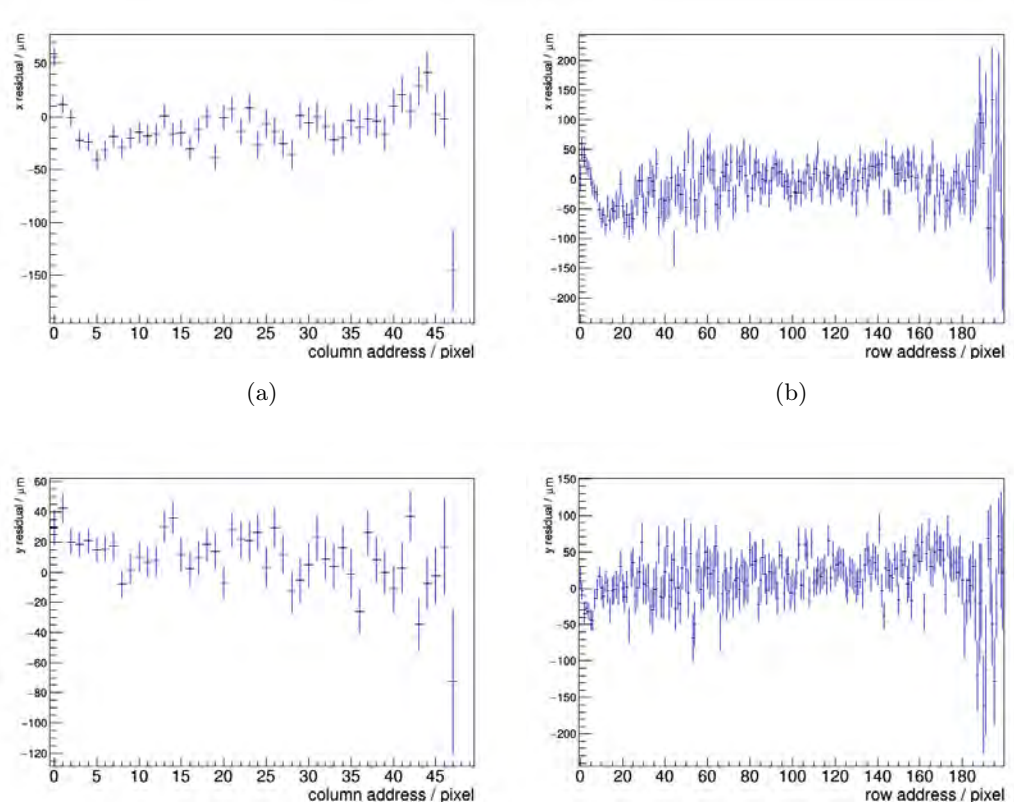

(a) (b)

(c) (d)

FIGURE 3.9: Profiles of the residuals and position for the MuPix8 sensor. The flat centre is expected as it indicates there is no rotation of the chip, the fluctuations are also expected due to the mixed beam.

3.2.2 Crosstalk and clustering

Charge sharing can produce clusters in MuPix8. Crosstalk can also produce clusters, as well as hits elsewhere in the chip. Charge sharing is most likely to generate clusters up to size 4 due to a particle depositing energy at the intersection of 4 pixels. Crosstalk happens in MuPix8 due to the signal routing. This is because the signal lines that transmit information from the analog pixel to the digital periphery are analog voltage signals. Due to the space between lines being limited neighbouring lines experience capacitive coupling. Crosstalk will only happen in the columns and never in the rows as the parallel signal lines travel along the columns.

During the testbeam there is no easy way to distinguish between crosstalk and real clusters from a traversing particle on an event-by-event basis. To study crosstalk, we need to study asymmetries between the cluster size along rows

and columns, if the cluster extends more than 2 along any row or column it is unlikely to be produced by a single particle. An exception to this are δ-electrons from rare hard scatters.

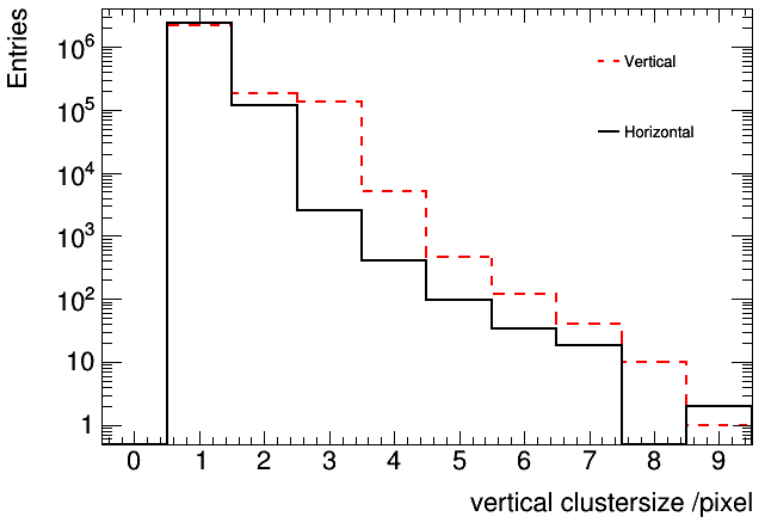

FIGURE 3.10: Number of clusters by different cluster sizes for both horizontal (x-axis) and vertical (y-axis). The high vertical 3 clusters are due to the effect of crosstalk.

Figure 3.10 shows the cluster size along columns and rows. This shows that there is a enhancement of 3-hit clusters along the columns. The cluster positions can also be plotted and are shown in figure 3.11. This shows that single-hit clusters are distributed homogeneously in the chip while 2-hit and 3-hit cluster sizes are located more towards the higher rows. The 3-hit cluster sizes are what we are interested in for crosstalk understanding. This means that if we examine the location of these, we can start to understand how long the connection length of the lines need to be for cross talk to accrue. The higher number of 3 clusters sizes are indicated in figure 3.11(d) by the lighter green colour.

To see if crosstalk is expected to be observable in the smaller MuPix9 chip, we need to examine at which point triple clusters start, we can see from inspection that very few triple clusters appear below row 60. As MuPix9 has only 20 rows of pixels it is unlikely to show crosstalk as the lines do not run parallel for long enough for a large capacitive coupling to occur.

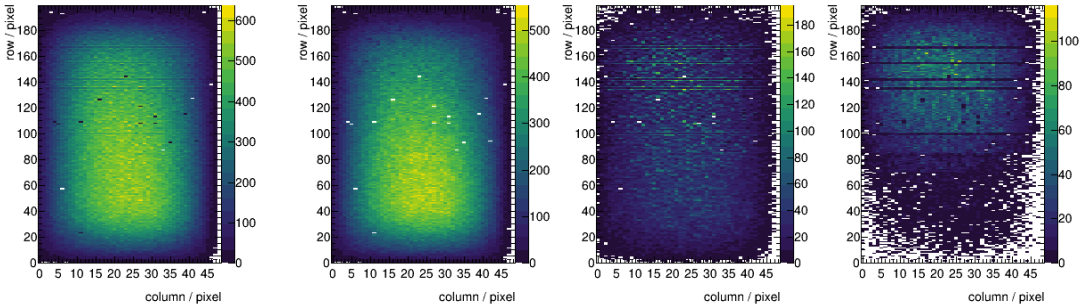

(a) (b) (c) (d)

FIGURE 3.11: Cluster position on the detector chip for clusters all clusters (a) and cluster size of 1 (b), 2 (c) and 3 (d).

3.2.3 Efficiency and Noise

Efficiency and noise are the most important aspects of the chip performance. An efficiency map and a noise map are plotted in figure 3.12, this shows that most of the chip has nearly 100% efficiency apart from the edges. The change in efficiency with respect to threshold voltage is shown in figure 3.13. Crosstalk is accounted for in this calculation. A reduction at the edge is expected due to the matching radius going outside the sensitive region on the chip. The noise rate, as defined earlier in this chapter, at the centre of the chip is approximately 5 Hz, the noise increases nearer to the edge in the upstream telescope layers. The white pixels have been masked due to unusually high noise rate. The edge effects on this is due particle scattering in from other places in the reference layer, the way this is accounted for in the efficiency calculations for figure 3.13 is to select a region of interest to remove these edge pixels.

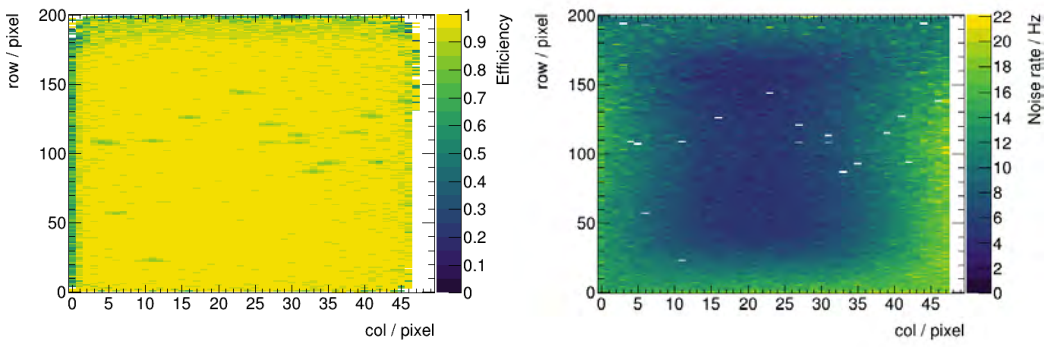

(a) (b)

FIGURE 3.12: Efficiency map (a) and noise map (b) for the MuPix8 chip with a threshold of 10 mV and a bias voltage of −60 V.

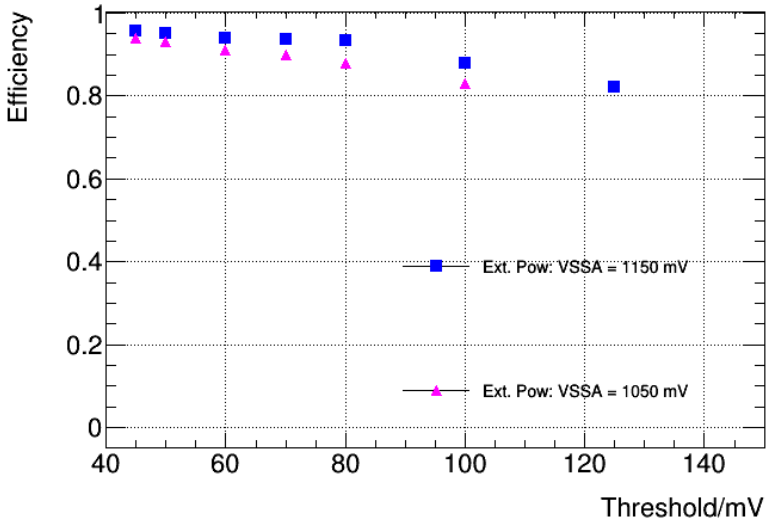

FIGURE 3.13: Efficiency of the MuPix8 chip with various thresholds and for 2 different external powering voltages of the amplifier (VSSA).

3.3 MuPix9 Studies

Due to the MuPix9 being small it is mounted on a PCB, with no cut-out, in the telescope and put into layer 1 of the telescope. Only a small number of tracks will actually pass through the DUT sensitive area. This must be accounted for when doing the efficiency calculation, a track map with the outline of the DUT is shown in figure 3.14.

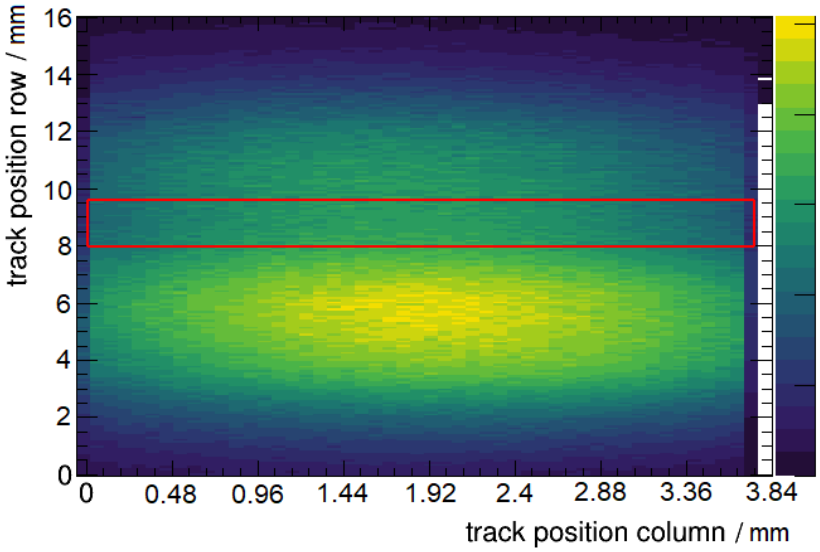

FIGURE 3.14: Track map, projected onto the DUT plane, for the MuPix9 runs with the DUT size marked in red. Only one matrix (A) in the MuPix8 is in use during these studies.

3.3.1 Alignment

Just as for the MuPix8 layers there is a mechanical alignment up to a precision of 150 μm. This is then followed by a software-based alignment which corrects for rotation around the beam axis and any remaining mis-alignment in x and y. After these alignment steps the residual distributions shown in figure 3.15. The distribution has a much larger RMS than that for MuPix8, the distribution is due to rounding in the calculation putting them more in one bin than the other. To understand why this difference exists we will examine variables that are imputed in the alignment procedure. The 2 variables inputted are the matching radius and the χ^2 of the track calculated from the track parameters and errors on hits. The χ^2 does not include the DUT. The distributions for these are shown in figure **??**, this shows that a suitable criterion for the matching radius is 450 μm to select a majority of tracks. This value is chosen to not cover a significant portion of the chip, this is also the same value used for MuPix8.

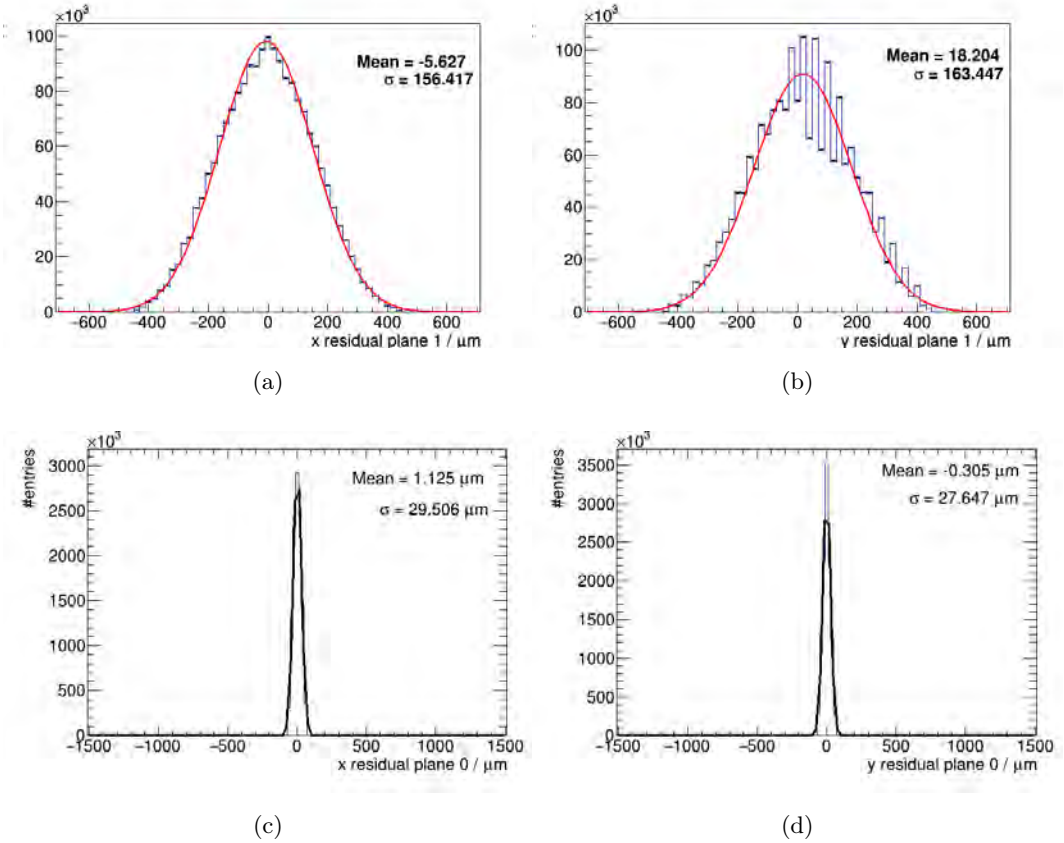

FIGURE 3.15: Residual plots for MuPix9 DUT layer for both x (a) and y (b) as well as residual plot for the 1st MuPix8 reference layer (c,d). Both of these have fitted with a Gaussian and the mean and standard deviation is shown on the plot.

We can check if there are rotations around the z axis by plotting the column (row) against the residuals of both the columns and rows and there profile taken. However it was noted that there was a rotation of the chip on the PCB. Adding a rotation of 17° around the y axis resulted in a flat centre indicating the rotation is account for, this should have been visible on the PCB however they chips had already been removed for the PCB. The corrected distributions are shown in figure 3.17.

The χ^2 criterion chosen is 20 as it will give enough data for analysis and selects tracks that are less affected by multiple scattering. The MuPix9 chip is mounted directly on a PCB without a cut-out where the sensitive area of the chip is and the sensor itself is not thinned. This leads to much larger scattering compared to MuPix8. To confirm that there are no other tracking problems that have been masked by this source of scattering we can look at the residual for the reference layers, as shown in figure 3.15(C)(D). The layer shown is layer

0, thus it is before any of the scattering of the MuPix9 chip.

Other track finding methods have been considered to try and improve the resolution of MuPix9. The method that was most suitable for the use case is a general broken line fit, this is a line fit that considers multiple scattering. This is however challenging with only three reference layers. This method was implemented, and the alignment was redone. The reference layer for the alignment in this case was the DUT. This is because the DUT is likely to have the largest kink in track, so the others are aligned around that. This however struggles to fit data due to the large scattering in MuPix9 PCB. To try and improve it the only scattering that the fit should consider is in the DUT layer, this however is still a worse result than the straight line fit by a factor of 4. This could be because the DUT layer scattering is so large that too many tracks can be considered, thus leading to a worse resolution due to the inclusion of higher scattering tracks.

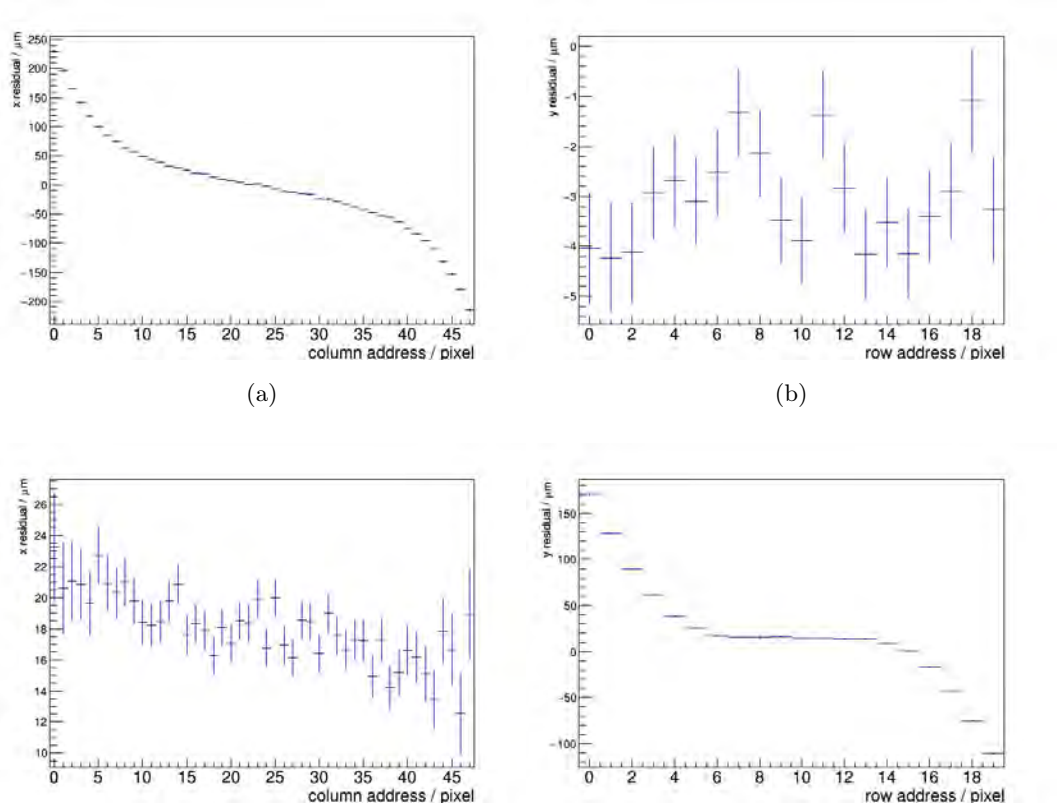

(a) (b)

(c) (d)

FIGURE 3.16: Profiles of the residuals and position for the MuPix9 sensor.

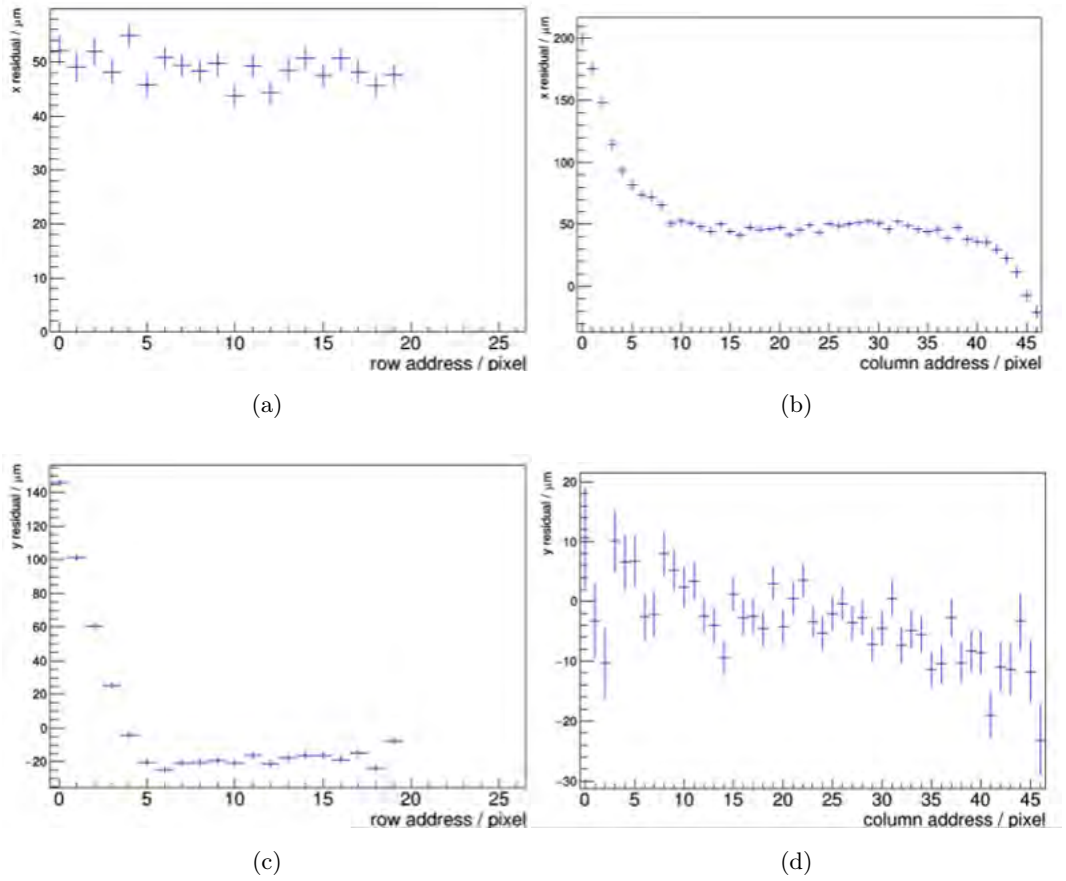

(a) (b)

(c) (d)

FIGURE 3.17: Profiles of the residuals and position for the MuPix9 sensor. These include a manual rotation of 17°.

3.3.2 Efficiency and Noise

For the MuPix9 chip the efficiency map as well as a noise map for a bias voltage of −40 V and a threshold of 80 mV is shown in figure 3.18. This shows that the measured efficiency in the centre of the chip is around 90% with the efficiency lowering toward the pixel edge due to scattering effects and matching efficiency. If we consider that MuPix9 is made on a 20 Ωcm substrate the depletion zone is smaller than the MuPix8 chip, a lower efficiency is expected. See also figure 3.3(D). Due to the increased scattering the track matching is also less efficient (figure **??**).

The noise of this chip is fairly uniform across the whole chip apart from 2 hot pixels with most being around 100 Hz, the map is shown in figure 3.18. The high noise 100 Hz compared to MuPix8 (2 Hz) is very odd as the threshold is set a factor of 8 higher (80 mV vs 10 mV). Due to the higher noise than MuPix8

a PMOS amplifier is preferred.

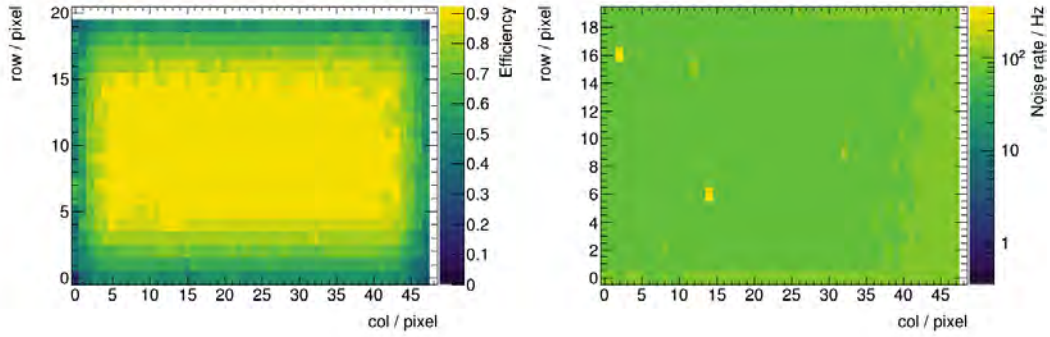

(a) (b)

FIGURE 3.18: Efficiency map (A) and noise map (B) for the MuPix9 chip with a bias voltage of −40 V and and a threshold voltage of 80 mV.

Chapter 4

The Pixel Tracker and Outer layer construction

The Mu3e detector will be the first to use the new ultra thin HV-CMOS chips in a particle physics experiment in order to make a high-rate capable detector with a very tight material budget constraint. The pixel tracker is described in detail in this chapter. It will then move onto discussing the development, construction and testing of the Mu3e outer pixel layer modules at the Liverpool Semiconductor Detector Center (LSDC).

4.1 The Pixel Tracker

The pixel tracker modules all have a very similar design consisting of 4 or 5 ladders glued to a polyethermide (PEI) endpiece on each side. For the 2 inner layers each module is a half cylinder shape with 4 or 5 ladders, each with 6 MuPix chips. For the outer layers each 4 ladder module is either 1/6th (layer 3) or 1/7th (layer 4) of the full cylinder having, with each module having 68 or 72 MuPix chips.

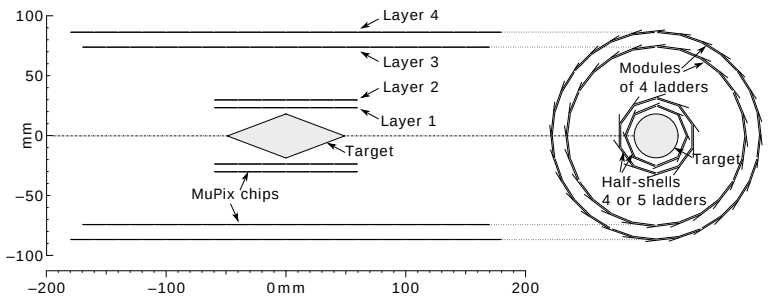

FIGURE 4.1: Geometry of the central pixel station

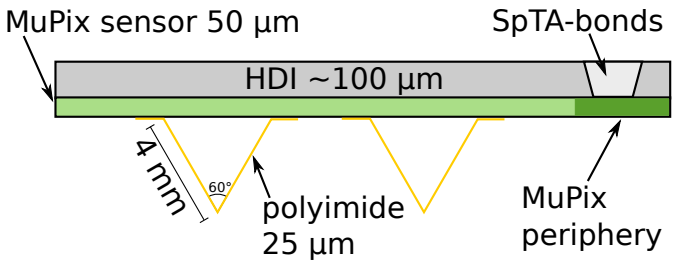

FIGURE 4.2: Cross section of the pixel ladders for layer 3 and 4 modules. This shows and labels each key element of the ladder.

	Layer 1-2		Layer 3-4	
	thickness [µm]	X/X_0	thickness [µm]	X/X_0
MuPix Si	45	0.48×10^{-3}	45	0.48×10^{-3}
MuPix Al	5	0.06×10^{-3}	5	0.06×10^{-3}
HDI polyimide & glue	45	0.18×10^{-3}	45	0.18×10^{-3}
HDI Al	28	0.31×10^{-3}	28	0.31×10^{-3}
polyimide support	25	0.09×10^{-3}	≈ 30	0.10×10^{-3}
adhesives	10	0.03×10^{-3}	10	0.03×10^{-3}
total	158	1.15×10^{-3}	163	1.16×10^{-3}

TABLE 4.1: Material radiation length of a MuPix ladder [1].

Pixel tracker ladders

The pixel ladders form the smallest mechanical unit of the pixel tracker, they integrate 6, 17 or 18 MuPix chips onto a 100 μm thick High Density Interconnect (HDI) circuit. For the inner layers there are small flaps connecting the layers together. This is to prevent helium flow between ladders causing mechanical vibrations. Due to the outer layers being substantially longer, there are two polyimide strips folded to a v-shape, glued to each ladder to add rigidity, as shown in figure 4.2. The ladders have been optimised to achieve a low material budget which is detailed in table 4.1.

Each ladder is electrically divided in half with the MuPix sensors being read out from either end, the chips are powered and read out through the HDI [99], to which the chips are glued. The main requirement for these is to be very thin and not to have any high Z material, this is achieved using multi layer aluminium/polyimide circuits. SpTAB-bonding is used to connect the different aluminium traces to the chips and to create vias.

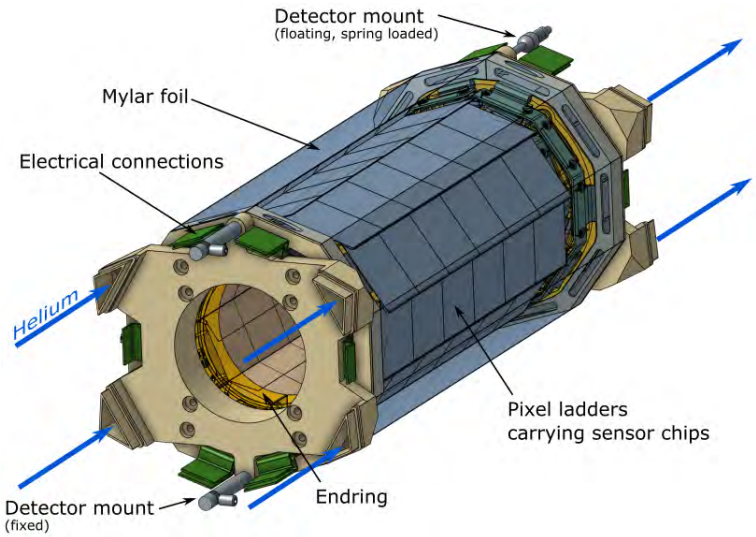

FIGURE 4.3: CAD diagram of the inner pixel tracker. The helium inlets and outlets are shown and other important elements labelled.

Inner layer modules

Layers 1 and 2 consist of half shell modules mounted onto support-rings as shown in figure 4.3. Each module consists of 4 (layer 1) or 5 (layer 2) pixel ladders and the connection to the outside is made via a custom interposer flex that is SpTAB-bonded to the HDI. This is done just outside the active detector region.

The inner layers are constructed at the Physikalisches Institut, Universität Heidelberg using a manual procedure. The chips are glued to the HDI under a microscope using fiducial marks. The ladders are assembled in to a module using a custom made tool.

Outer layer modules

The outer pixel layers consist of 13 modules in total each with 4 ladders. These will be read out the same way as the inner layers. A schematic view of a layer 4 module is shown in figure 4.4.

The outer pixel ladders are constructed in the University of Oxford's Physics Microstructure Detector (OPMD) Laboratory. The MuPix chips are placed and glued to the HDI using a robotic pick and place machine along with custom tooling achieving a precision of 5 μm. These ladders are then SpTAB-bonded before the v-folds are glued to the chips. This is done by a liquid dispensing

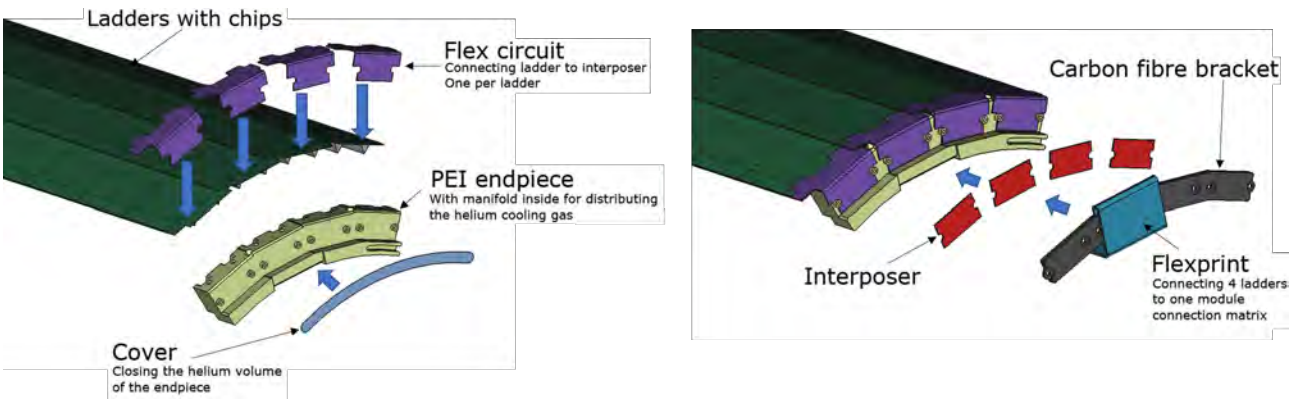

FIGURE 4.4: Exploded view of a layer 4 module. The blue arrows show construction ordering steps.

robot to form a glue layer of 5 μm. Ladders are shipped to the University of Liverpool LSDC where the modules will be assembled and tested. A detailed description of the latter procedures is given in this thesis.

Global mechanics

The pixel tracker outer layers are mounted on 2 end-rings to form the full cylinder. The end-rings are mounted on the beam pipe. They are made out of PEI and will provide the helium flow ducts. A diagram for the outer layer end-ring is shown in figure 4.5. The end-rings have dowel pins for each module to guide these during mounting, as well as screw holes for the modules to be secured. The outer pixel layer end-rings are spring mounted at one end to accommodate the thermal expansion of modules. The mounting procedures for the outer layers to the end-ring are devised by the University of Liverpool Mu3e group.

Detector cooling system

The cooling system will use Helium gas, cooled to 0°C, to keep the pixel chips operating under the required conditions. Helium was chosen to not add a lot of material in the active detector region. The estimated power consumption of each MuPix chips is 250 mW/cm^2 while the maximum planned for is 400 mW/cm^2. A schematic diagram of the Helium flow in Mu3e is shown in figure 4.6.

There are 3 different helium flows used in the design each with different flow speeds which are detailed in table 4.2. The different flows in the detector are

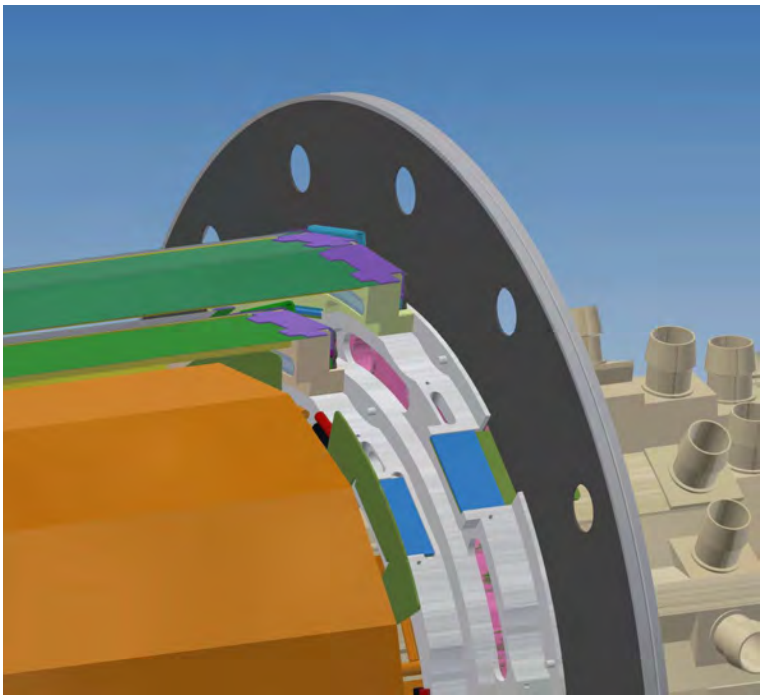

FIGURE 4.5: Diagram of the outer pixel modules mounted on the end-ring.

Location	Velocity $\mathrm{m\,s^{-1}}$
Gap L1-L2	10
Gap SciFi-L3	10
Gap Tile-L3	10
Gap L3-L4	10
Global flow	0.5

TABLE 4.2: Helium gas velocities in the pixel detector gaps, channels, and global flow [1].

shown in figure 4.6. There are global flows between layer 3 and 4 as well as between 1 and 2. There is also a global flow between the fibres and layer 3 [99].

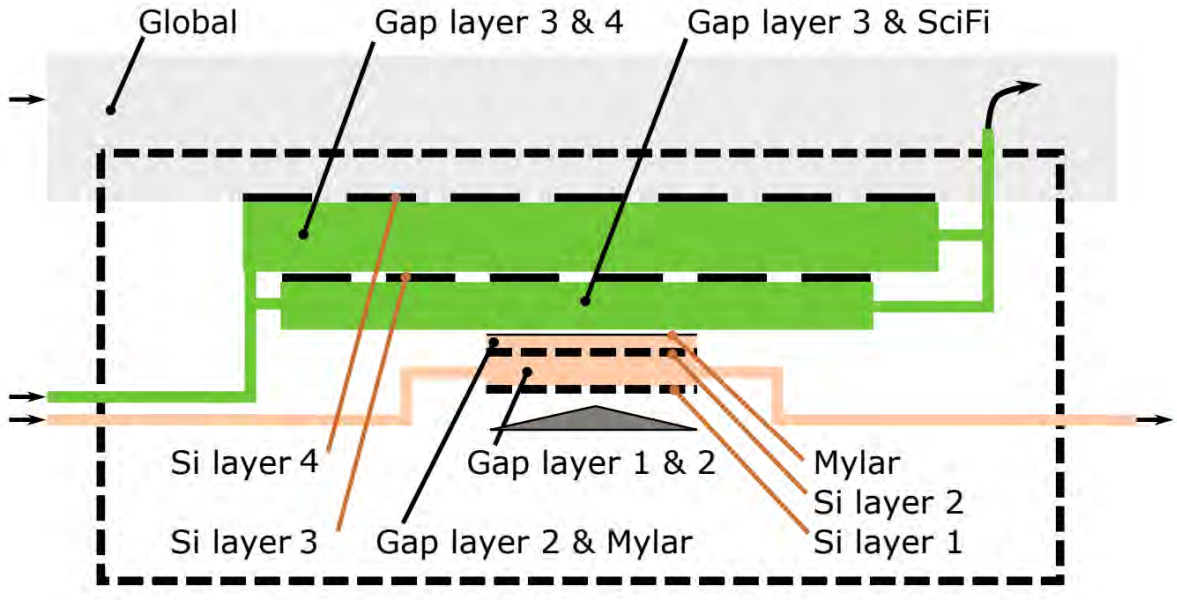

FIGURE 4.6: Helium cooling schematic for the pixel detector with the flow volumes and directions shown. This is a slice of the central detector station along x=0 [1].

4.2 Thermo-mechanical mockup construction

The thermo-mechanical mockup modules are the first type of modules that have been produced. The purpose of these modules is to develop the construction procedures and allow for testing of the cooling system. The ladders for these modules consists of a layer of kapton with a thin layer of aluminium on top, aluminium is then etched away using a laser cutter to form 2 resistance traces which, when powered, can produce similar heat as a ladder with chips. Flowing Helium through the v-folds was originally foreseen as necessary for the overall cooling, however it later transpired that this was not necessary and not feasible economically. Helium flow in the v-folds only accounts for 17% of cooling and the power consumption is less than the specification. The thermo-mechanical modules were produced when v-fold flow was still intended to be used.

When constructing the thermo-mechanical mockup modules the first step was sealing the endpiece to allow Helium to flow through the v-folds. This meant that a groove cut for machining purposes needed to be sealed, this is done with a 25 μm PEI plate. The method devised to glue this plate securely involved applying a layer of araldite to the whole of one side while the plate is on a piece of tape. The tape allowed for the end plate to be handled without affecting

the glue. The obtained glue seal was tested to withstand the required 100 mbar over-pressure. This was tested by constructing a mock up of the seal with access to flow air from behind. It was then flowed up to 6000 mbar when the test was stopped.

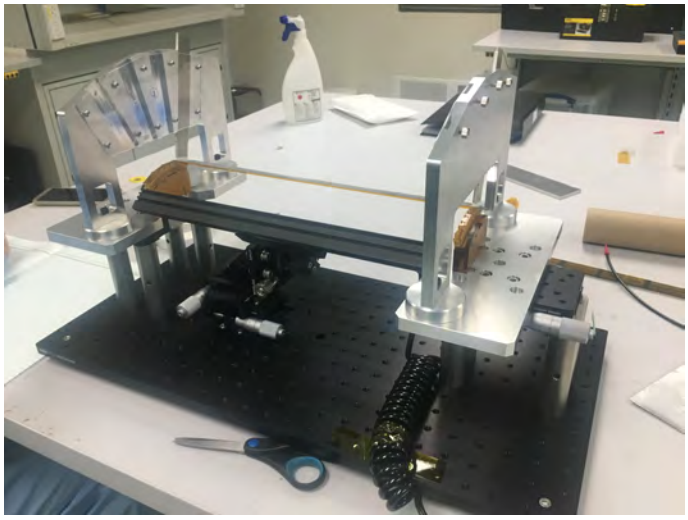

FIGURE 4.7: Construction stand for the thermo-mechanical ladders.

The ladders for module construction are sent from Oxford to Liverpool in purpose-built support frames. The first task when they are received is to do a visual inspection of the ladder and the v-folds. This is to check if there are any visible defects. Defects can arise from transport or problems during manufacture. For the first delivered ladders it was noticed that some of the resistance traces where not etched away correctly so cannot be used electrically. Another problem found was that the support frame clamping mechanism cut into the ladder compromising the traces, this was fixed in a later design. The final check before metrology is performed for the thermo-mechanical ladders is to take resistance measurements of the inner and outer traces to confirm that the heater circuit performs as expected. Metrology is then performed on each ladder. This is detailed in section 4.3.1.

For module assembly, endpieces are secured to the construction stand with screws. A picture of the construction stand is shown in figure 4.7. It consists of a few key parts, the endpiece mounts are located on 2 optical boards allowing for fine adjustment with a micrometer screw. There is an arch above each on the endpieces allowing for gluing weights to be held at the correct angles for each of the ladders. The final part is the vacuum chuck for the ladders to

be positioned with minimal physical handling due to its mounting on a x,y,z,θ stage.

The endpieces are set at a fixed distance by using a precision-made metal bar with a calibrated length of 360000 $\pm$ 5 μm. The ladder is then placed onto the vacuum chuck and epoxy (Araldite 2011) is applied to the endpieces for the ladder to be secured. Each ladder is mounted individually as the ladders overlap each other.

This method was used to construct the first prototype module, however various issues where found. It was found that the x,y,z stage for the vacuum chuck was difficult to manipulate with sufficient precision and was thus not adequate for placing the ladders. This also meant that once the ladder was rotated into position, it did not fit well.

This led to the vacuum chuck being removed to make a series of thermo-mechanical modules using a more manual procedure, allowing for other quality tests, while a new construction stand is designed and manufactured.

Another change was to place glue on the endpiece where the heater circuit is folded over the endpiece, this can be seen in figure 4.8. This allows for the ladder to be secured in 2 locations and allows for better alignment the multipin interposer. This may mean that the v-folds don't sit entirely in their natural position, as we are not aligning to these any longer, however there is more tolerance in the v-folds than in the interposer position.

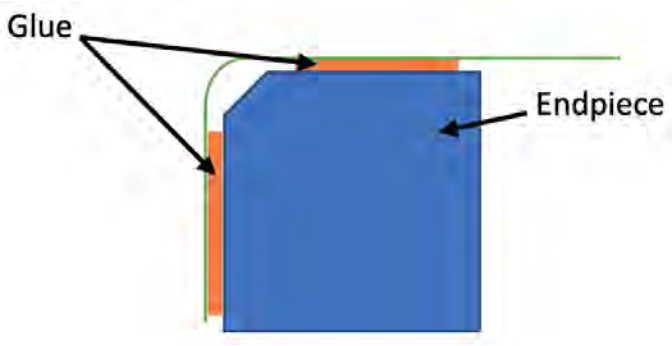

FIGURE 4.8: Location of glue for securing the ladder to the endpiece. A weight is applied to each gluing location to ensure good contact.

4.2.1 Sealing the v-fold

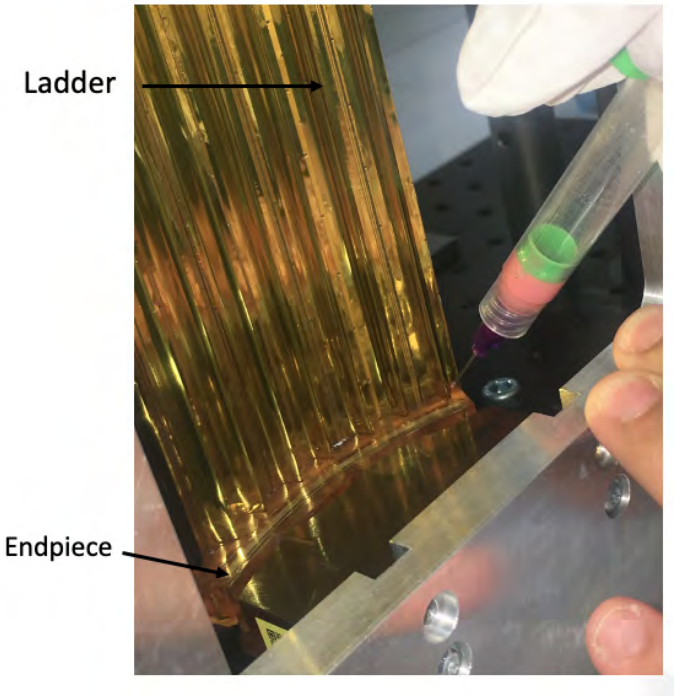

FIGURE 4.9: Sealing of the v-folds with a hypodermic needle and a vacuum pump. This allows for fine control of location and quantity.

After the ladders have been glued onto the endpieces the v-fold must be secured to the endpiece, this is to prevent leakage of the Helium into the global volume leading to less efficient flow.

To achieve this an optical glue was used initially called Epotek 301-2, dyed green for better visual inspection as its stock colour is clear. This glue was chosen due to its low viscosity allowing for the capillary effect to be used, thus allowing the v-folds to be sealed along the length of their contact to the endpiece. The glue was applied by placing the module in a vertical position and using a hypodermic needle to apply the glue.

It was found that the glue penetrated well beyond the v-fold walls and flowed into the helium channels inside the endpiece thus blocking these. Different methods where trailed to prevent this from happening. The first was to apply the glue from below. However, in this gravity is greater than the capillary force and the glue ran down the ladders. The other method was to use a vacuum pump to improve control on the amount of glue deposited. However, the problem persisted.

This led to other glues being tried. The first method tried was using SYLGARD™ 186, however due to this being a silicone-based glue it is more of a sealant and due to concerns about the long-term performance a solid setting glue was preferred.

The next glue that was tried was Loctite EA 9396, this is an already dyed glue and has a high viscosity. Due to this high viscosity value the glue does not penetrate far from where it is applied. To improve sealing Araldite 2011 was also applied to the endpiece where the v-folds sit. This improved the seal along the contact between v-fold and endpiece. It was found that this process worked well and is repeatable, it is shown in figure 4.9. All glues used have been tested for radiation tolerance by other experiments and are also used by them, eg. ATLAS [100].

4.2.2 Clamping tests

Due to the change in the cooling of the pixel tracker, no longer using Helium flow in the v-channels, a new option for construction became available to us. This is to clamp the ladders to the endpiece rather than by using glue, this has the benefit of allowing ladders to be replaced in case of failure of chips. Tests were done to establish the potential loss in rigidity of the module or ladders.

The first test done was to construct a module without sealing the v-folds allowing for comparisons to be made, both modules where then placed on a wire bond pull tester. The hook of the tester was hooked over the edge of a ladder and the machine pulled until the hook slipped. This allows us to spot differences in the torsional stiffness of these ultra-low mass ladders. For the module with sealed v-folds the results are 5.04 $\pm$ 0.13 g and 1.61 $\pm$ 0.10 g for 2 ladders at different positions on a module, and thus at different angles with respect to the hook. While for the module without v-folds the results are 4.86 $\pm$ 0.21 g and 1.62 $\pm$ 0.04 g. All variations are small and within errors.

A further method to check the stiffness was to mount a module onto a vibrating table, vibrating at a frequency of $\sim$5 Hz. The movement of the module was measured with a capacitance distance sensor with a reading rate of $\sim$3000 Hz. This test was also done for both modules and a snapshot of the observed movement is shown in figure 4.10. The amplitude of the ladder with sealed v-folds vibration is 77.8 μm while that for the ladder without sealed v-folds is 85.5 μm

and the vibration and frequency are comparable.

It was concluded that the sealing of the v-folds does not contribute substantially to the module rigidity.

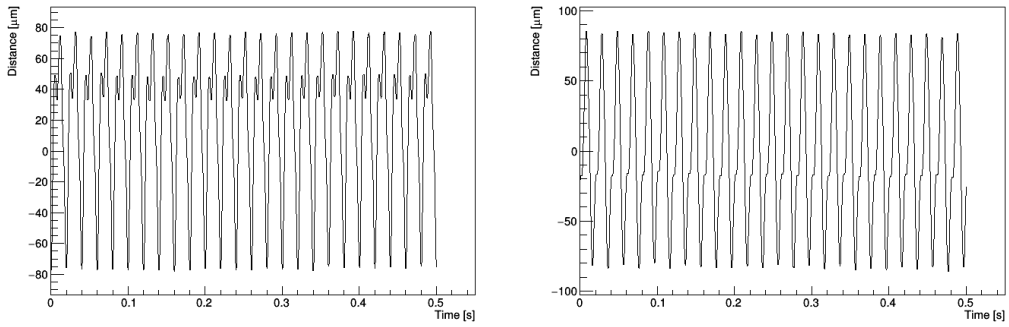

(a) Sealed V-folds (b) Non sealed V-folds

FIGURE 4.10: The vibration produced on the vibrating table with (a) a module with sealed v-folds and (b) a module without sealed v-folds. The slight step seen around 40 μm deflection is a feature of the vibrating table.

4.3 Quality assurance tests

4.3.1 Metrology

Before the ladders are used in the construction of the module's metrology tests are performed. Because of the strict tolerances in the detector, we need to know the length of each ladder to within 100 μm as well as the position of the v-folds to 100 μm. On the final production modules chip positions are also foreseen to be recorded.

Ladders

Metrology is performed on an Optical Gaging Products Smart Scope. A number of positions on each ladder are recorded by manually selecting, as detailed in figure 4.11. These are chosen to constrain all critical dimensions of the heater ladders ranging from the length of the v-folds and the ladder to the position of the v-folds on the ladder. Each ladder is measured, and data are recorded to file for later analysis and record keeping.

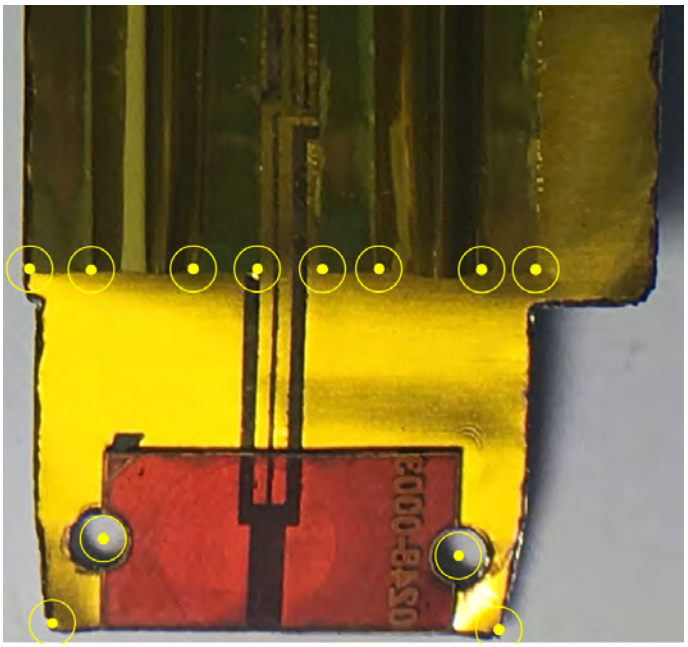

FIGURE 4.11: Diagram showing the points taken during meterology for a thermo-mechanical ladder, only one half is shown. The other side is a mirror image.

The main area of interest is the length of the ladder and the properties of the v-fold. These are important as the length of the modules is tightly constricted due to the mounting of multiple modules to a single set of end-rings. The v-folds need to sit inside dedicated slots in the endpiece. If the channels are distorted the Helium will not flow correctly and the ladder may become distorted.

For the thermo-mechanical ladders, a spacer element is glued to the ends of each ladder. This is a 25 μm piece of kapton to add space due to the missing interposer flex used to read and power the chips. As this locates the ladder to the endpiece, it defines the length of the ladder. The nominal length of layer 4 ladders is 390 mm. Figure 4.12 show the measured length of all manufactured flex heater ladders for layer 4. As can be seen the ladders tend to be longer than the nominal length however the distribution narrowed as more ladders were made converging on a more repeatable length. Deviations can be absorbed in the mounting of the thermo-mechanical modules, since where the ladder meets the endpiece there can be a small overshoot of the flex circuit before it bends down by 90° to connect to the interposer.

The length of the v-folds has also been examined. The metrology results for all layer 4 flex heater ladders is shown in figure 4.13. The nominal length shown is from the original design. However, this allowed only a 100 μm tolerance for

the assembly, which was deemed too small. Thus, the length of the v-folds was reduced to allow for a better fit.

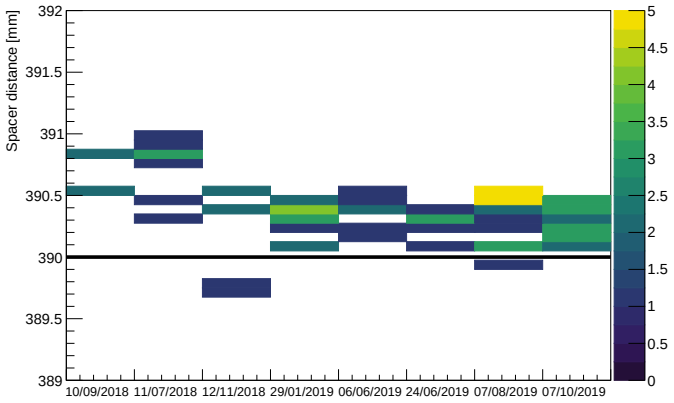

FIGURE 4.12: The distance between the ladder spacers over time, the black lines show the nominal length.

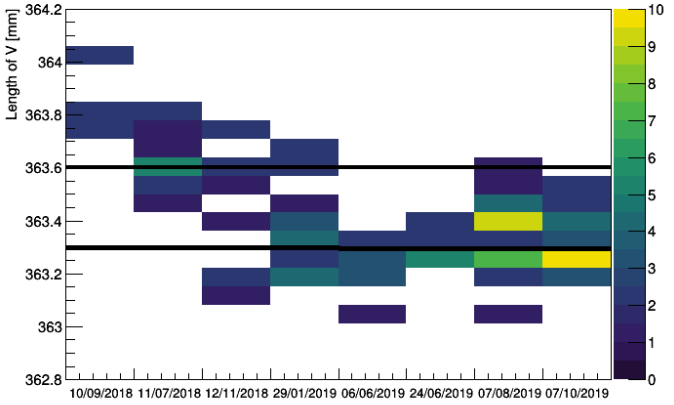

FIGURE 4.13: The length of the v-fold glued to the underside of the layer 4 ladder. The black lines at 363.6 mm show the initial nominal length, while the line at 363.3 mm shows the new nominal length. It was reduced to allow more tolerance when mounted inside the endpiece.

Modules

After assembly, metrology is done on all modules, this allows to verify the relative positions of the ladders and the length of the modules. The length of the module is important as there is only a small tolerance on the length difference between modules in the same layer. Due to the end-ring design, the length difference between layer 3 and 4 is also fixed. The data are shown in table 4.3, this shows that as more modules were produced the difference between these

Module Number	Length (mm)	Δ L	%RH
1	379.90	0.10	47.2
2	380.28	0.10	47.1
3	379.97	0.10	47.3
4	380.36	0.10	47.2
5	380.46	0.10	47.4
6	379.59	0.10	47.4
7	379.51	0.10	47.1

TABLE 4.3: Metrology data for the L4 thermo-mechanical modules. The relative humidity in the room was also taken due to its effect on the length of kapton.

became smaller. The variation in temperature in the clean room was ± 1 °C thus have minimal effect. The variation in humidity was ± 20% across days, this could have a strong effect on the length of a module leading us to measure the humidity to ensure minimal effect. This allows us to understand the difference in each module length is down to construction procedure. The measurement error is due to the repeatability of identifying positions on the module for the metrology measurement, this was done by a master's student who repeatedly took measurements and plotted a Gaussian to find the mean.

4.3.2 Air flow system

To be able to perform electrical testing on the module in the lab it needs to be cooled. This is to prevent heat damage to the chips and glue. Two methods were devised for cooling the module, this is a different cooling system than the final detector. The first was using the v-folds when these were still planned to be used for cooling, still discussed if the v-fold cooling will be needed in future, and the second using air flow around the outside of the module.

V-fold flow

The v-fold cooling system has been designed to mimic the proposed cooling for the final detector as close as possible, this allows for full access around the module while the module is running. This means that the most challenging requirement for this system was to have 0±5 mbar differential pressure at the centre of the module. This allows the experiment to achieve the necessary high flow rate without any substantial pressure that would deform the thin-walled

channels.

The first method considered was to use a fan inside a closed circuit, however there was no fan found that can deliver the correct pressure needed in the small diameter tube. This led to a venturi pump being considered, this makes use of the venturi effect where the flow of the gas passes another pipe causing suction creating negative pressure in that pipe. A schematic of the air flow system is shown in figure 4.14 (a). This design was realised in the system shown in figure 4.14 (b). The air passes through the venturi pump before being split in two with most of the air leaving the system, this is to achieve the negative pressure needed. The air that doesn't leave passes through a pressure and flow meter. This set up allows for full control of the flow rate and the pressure at the inlet and outlet of the module allowing us to achieve the required 0 mbar differential pressure at the centre of the module. It also can provide flows up to 2 L/min of air.

The system allowed for the testing of how well the v-folds are sealed to the ladder and endpiece, thus finding if any leaks are present. During early thermo-mechanical construction, we were able to use a leak detection fluid to find the leaks. The fluid produces bubbles in case of leaking gas. This works well and we can detect very small leaks with this. However, the method is not suitable for the final detector. It was then studied if leaks could be detected with a precision microphone. Using a PCB Piezotronics 130F20 microphone connected to an oscilloscope, we were able to detect even smaller leaks than we were able to with the fluid. We did not quantify this due to us needing to seal any leak found and the v-fold cooling was abandoned not long after this work as done.

Global flow

Once the v-fold cooling requirement had been removed a new method needed to be designed, one that could flow air around the module. The removal of the v-folds removed the challenging requirement to limit the differential pressure in the channels. A box was designed and constructed that allows for this to happen while also keeping the module secured to a plate. A CAD diagram of the designed part is shown in figure 4.15. The box consists of 2 parts, the undercase which slides under the module in grooves cut into the aluminium base plate where the module is fixed, and the top case which is lowered onto dowel

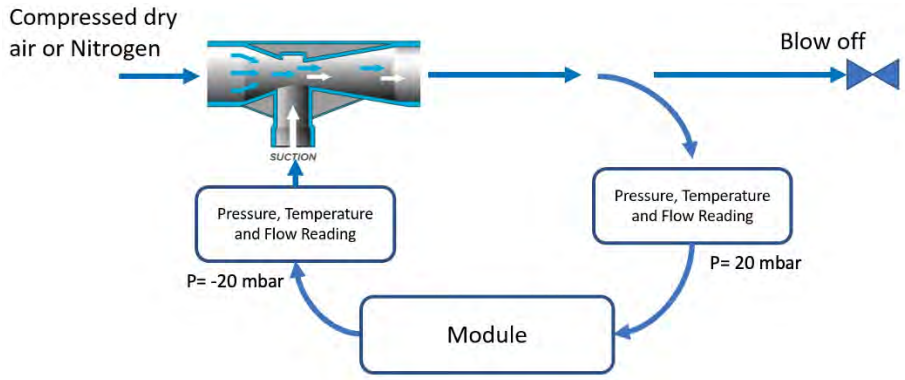

(a)

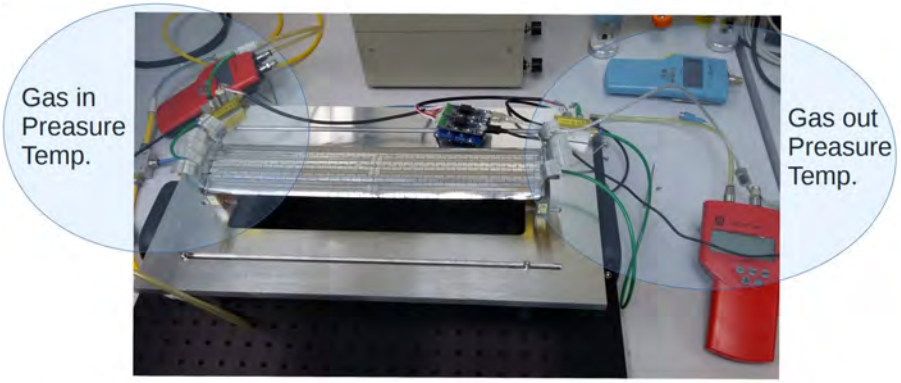

(b)

FIGURE 4.14: Airflow system for the v-fold cooling. (A) Is a schematic view of the cooling system showing the location of the key elements. (B) is the image of the system in use.

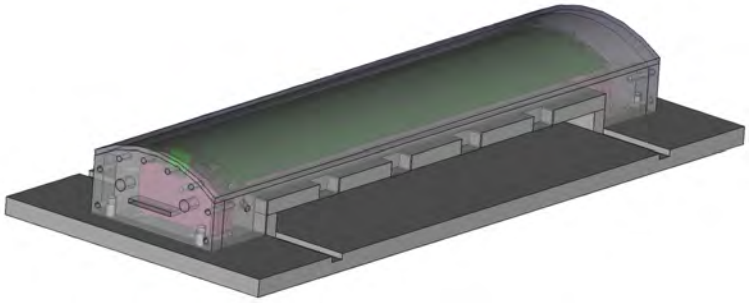

FIGURE 4.15: CAD diagram of the global cooling box. It consists of a top box placed over a module and a box under the module.

pins. The top case has all the inlets for air as well as the openings for electrical connections. The top surface can be made out of a very thin material such a kapton, to allow for the heat of the module to be read out by a thermal camera.

Cooling of the gas

To add extra cooling power to the system the circulated gas is cooled before getting to the module. This is done by placing a winded copper tube onto a cold plate set to −30 °C. This method reduces the gas temperature from 22 °C at the inlet to 12 °C.

4.3.3 Powering and temperature sensing

Using the global cooling box we can test the cooling of a module at different levels of power dissipation. To be able to test the cooling potential it is important to know the temperature of the module without cooling. Therefore 3 data sets are taken. The first was a module not inside the global cooling box, one inside the cooling box including the lid but still without cooling and the final one inside the box with cooling provided. The data set taken inside the cooling box but without cooling is important as it allows for the effect of the lid and the heating of the air around the module to be estimated. The cooling air, at a temperature of 18.7 °C, flows from one side of the box through 4 inlets at a rate of 18 L/min per inlet. A thermal image of a flex-heater module can be seen in figure 4.16 after 2 minutes of running. The bright spots are spots where Tippex has been painted onto the module to remove any reflections from

the aluminium surface and thus to obtain a more reliable temperature measurement. The observed temperature as a function of the set power dissipation for the half of the module closest to the cooling is shown in figure 4.17(a) while that for the half further away from the inlets is shown in figure 4.17(b). Fully functional half modules will dissipate approximately 9 W of power. The results show the cooling test stand has a substantial margin to keep temperature rises small and we can operate the module with cooling easily. It also shows that we will be able to run the module without any cooling for a period of time without overheating as well. To further see the effect of only cooling from one side the hottest spots at both module ends are plotted together, in figure 4.18. This shows that in the operating range of the modules, and with the high gas flow rate in the test box, there is no substantial variation in temperature along the length of the module.

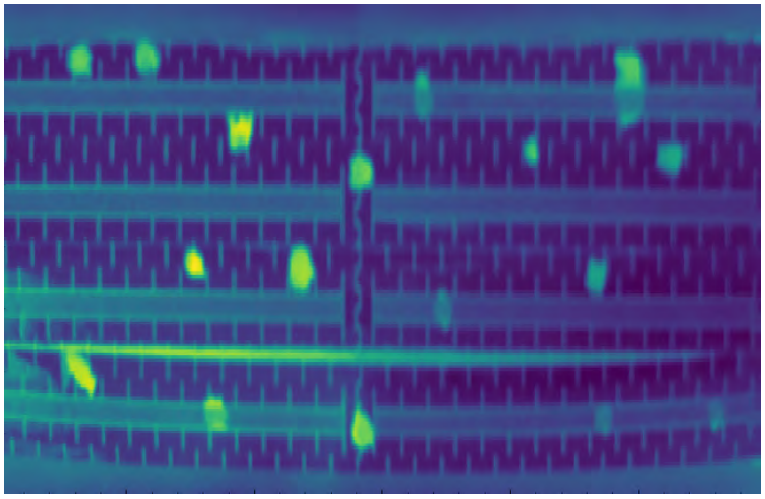

FIGURE 4.16: Thermal image of a flex-heater module with power of 18 W. The dots shown on the image are tippex which was painted on to deal with the reflections from the aluminium.

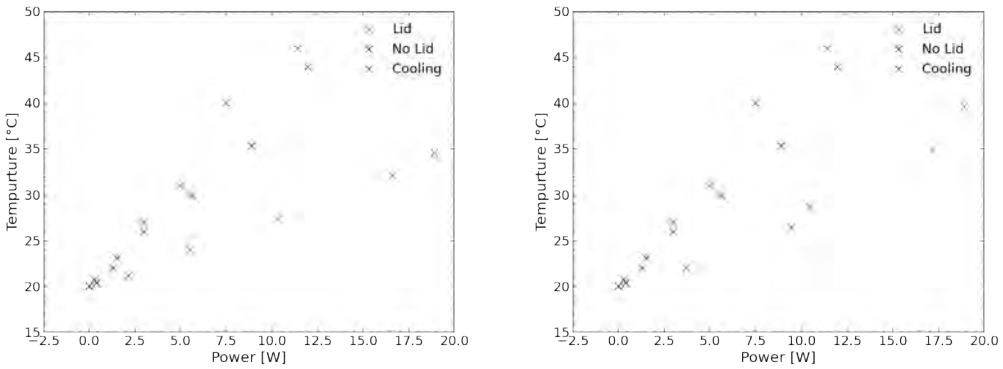

(a) (b)

FIGURE 4.17: Distributions of the temperature of the module. The power shown is for each half-ladder. It is split into 2 halves (a) the first half is closest to the cooling inlet while (b) is from the middle of the module to the end of the module.

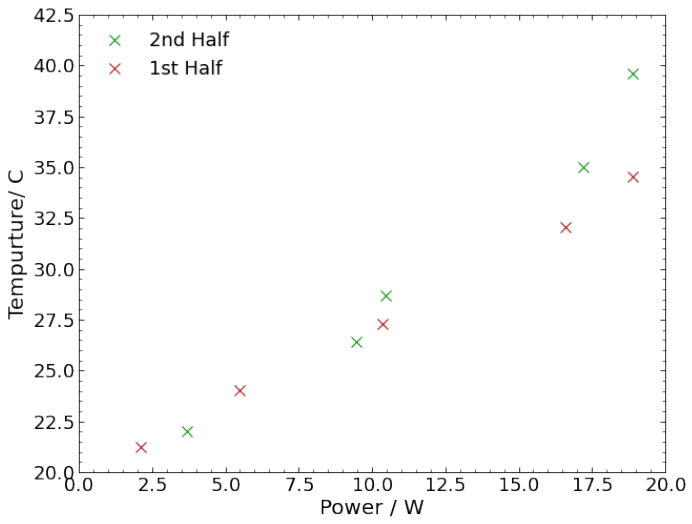

FIGURE 4.18: Comparing the maximum temperature of each half of the module. The first half is closest to the cooling inlet while the second half is from the middle of the module to the end of the module.

4.4 Mounting studies

4.4.1 Length Tolerance and Ladder Extension Studies

The minicage is a setup designed to facilitate the development of the tooling and methods to mount modules safely to the pixel support rings, which is

particularly challenging because one of the rings is spring-mounted. It also allowed cooling studies to be done at the University of Applied Sciences and Arts Northwestern Switzerland. The minicage consists of a mock-up of the beam pipe sections with the same mounting points envisaged for the final detector, including the spring mechanism.

The first test done were to try to determine the maximum difference in length that can be tolerated between modules. To do this the modules were mounted to the minicage without the spring mounting included. This was done for a number of combinations and ordering of the modules to study different length differences between neighbouring modules. It was found that with a length difference around 500 μm between neighbouring modules there started to be visible deformation in the modules. This led to setting a conservative upper tolerance of 50 μm for module differences.

Due to the modules being mounted under spring tension we also investigated how a ladder behaves when pulled using a material tester. This allows us to select a value for the spring constants of the spring used that ensures that no damage will be done. It also allows us to see if we can tolerate a larger tolerance of the length deviations by investigating the expansion of modules under tension. The force extension graph for a single ladder is shown in figure 4.19. The first test was done only going up to 100 μm extension and no visible deformation was observed however when the extension was taken to 200 μm some deformation was observed. This led for us to be cautious when choosing the spring for the minicage and wanting to keep the force between 1 N and 2 N for each of three springs around the ring.

4.4.2 Mounting Studies

Due to the end-ring being spring mounted, there needs to be a way to hold it into place while modules are mounted, the first method tried was to attach a rigid carbon bar to protect modules from taking all the strain of the springs before all modules are attached. This proved to be effective, however this solution did not provide a good solution for transferring the load from bars to the modules. This could lead to a unacceptable force on the modules when the rigid bar is removed, which is would be dangerous for the module with chips. This meant a

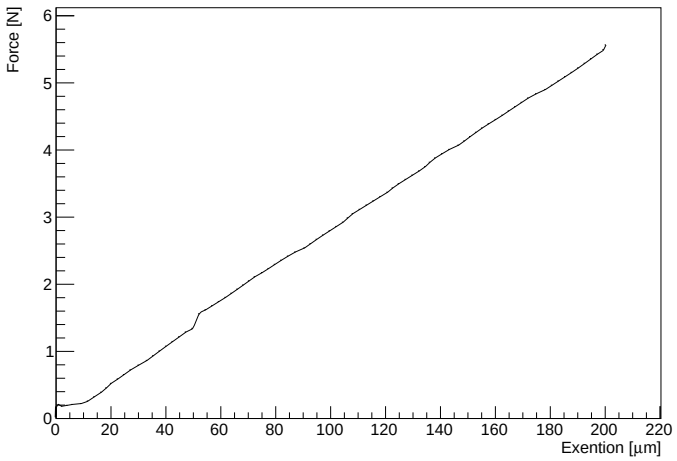

FIGURE 4.19: Force extension graph of a single ladder. The test was stopped at 200 μm due to a test run showing inelastic deformation when extended to 300 μm.

alteration to the rigid bar has been made to allow for a controlled extension of the length by up to 5 mm. The extendable bars are shown in figure 4.20. This has been preliminary tested and works effectively.

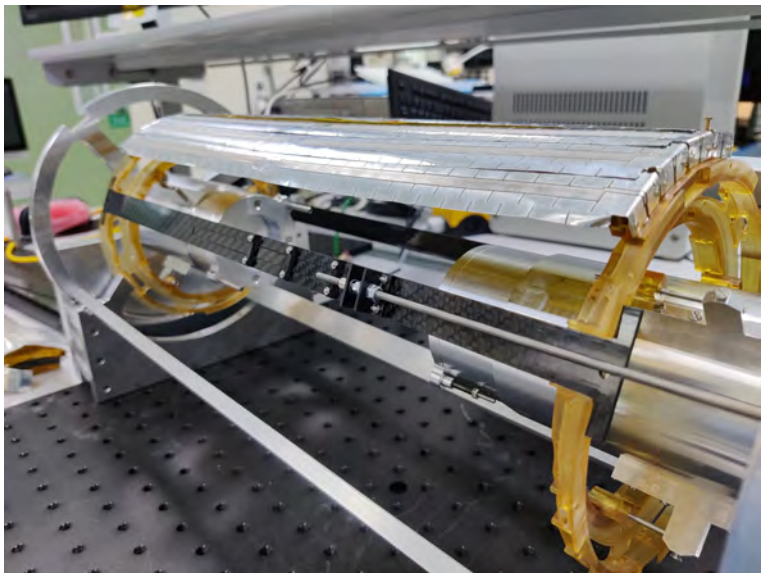

FIGURE 4.20: Picture of the extendable carbon bar mounted on the end rings.

Chapter 5

Sensitivity study

The Mu3e experiment aims to measure the electron and positron tracks from the decay $\mu \longrightarrow eee$ with high acceptance and resolution. The resolution allows for the final state to be precisely reconstructed, allowing for the desired signal events to be separated from the background from Internal Conversion events, $\mu \longrightarrow eee\nu\nu$. The sensitivity relies on the ability to reduce this background.
The aim of this chapter is to establish how well the main sources of background can be suppressed. This chapter will look at Internal Conversion events and the dominant source of combinatoric backgrounds, the combination of Michel positrons with a Bhabba electron positron pair. Selection criteria applied to the reconstructed vertices are discussed and the detector resolution of studied. The selection criteria are optimised to reduce the number of background events in the signal region. The sensitivity of the experiment to the signal is studied and an expected upper limit on the branching ratio of $\mu \longrightarrow eee$ as a function of the number of data-taking days is provided.

5.1 Simulation of Signal and Internal Conversion

The simulation of signal decays is done by using three particle phase space distributions, this follows the practice of SINDRUM. Signal and Internal Conversion events are simulated by having only one muon decay in each simulated frame. A frame is a 64 ns window. As the decay can happen at any point in time the decay can have particles that are detected in the following frame, if this is the case then no new decay is generated in the following frame. The simulation of Internal Conversion events does have generator criteria applied. This is because the region of interest is that in which the neutrinos carry little energy. The phase space when the neutrinos have a total energy less than 20

MeV [88] branching ratio is 2.1×10^{-11} with the inclusive branching ratio being $(3.4 \pm 0.4) \times 10^{-5}$ [72]. The generator criteria also account for the acceptance of the detector. The first is that each electron positron must have a minimum energy of 10 MeV, this is the minimum energy needed for the particle to traverse at least 4 pixel layers. There is also a criterion on the absolute value of the $\cos(\theta)$[1] to be less than 0.8 for each track. The final criterion is on the invariant mass of the 3 electrons, requiring this to be greater than 90 MeV/c^2 to ensure this is close to the signal mass window. The signal sample contains 8.779×10^7 frames with one signal decay each. The Internal Conversion sample is weighted with the leading order tree level matrix element for polarised muons from Ref [88] and the phase-space volume [101]. The sample consists of 4.995×10^8 frames, corresponding to an effective number of muon decays of 2.247×10^{13}.

5.2 Reconstruction and Selection

5.2.1 Reconstruction

The events simulated are reconstructed using the algorithms described in section 2.4.2. Tracks are first reconstructed as short tracks made from 4 hits. These are then extended to long tracks with 6 or 8 hits for better momentum resolution. Vertices are reconstructed for all track combinations of 1 electron and 2 positrons. There is a selection on the χ^2 (equation 2.5) of the tracks to be at most 32 and 48 for short and long tracks, respectively.

It is possible that when reconstructing a track there can be multiple track segments for the same particle. This can happen when a particle passes through the overlap regions of pixel ladders or through the target more than once. A particle passing more than once through the target can also be reconstructed with the opposite sign charge. To reduce this source of error a selection is made on the opening angle between tracks. If there are 2 tracks of the same electric charge and a momentum difference less than 1 MeV/c then the opening angle needs to be greater than 0.14 rad. If the 2 tracks are of opposite sign then the angle needs to be smaller than 3 rad. If this is not the case the event is rejected. The only decays that are considered are those where the muon decay is reconstructed close to the target. This is done by selecting only those vertices that

[1] θ is the polar angle measured from the z axis

fall inside a cylinder of radius 19 mm and length 100 mm centred at the target location.

5.2.2 Selection and Background Estimate

Once good vertices are selected, a number of further constraints are applied. The criteria applied in the following studies are on the vertex χ^2 value; described in section 2.4.2, the absolute momentum of the 3 tracks, the mass of the lowest mass track pair and the invariant mass of the tree track system.
The criterion on the vertex χ^2 value allows for the selection of vertices whose tracks coincide closely in space. This allows for further reduction of accidental backgrounds, as vertices reconstructed from tracks from independent decays tend to have larger χ^2. The criterion is not expected to have a major effect on the Internal Conversion background. The distribution of the χ^2 for both Internal Conversion and signal events is shown in figure 5.1. The fraction of long tracks to all tracks is 53% for Internal Conversion and 51% for signal. As expected, the criterion does not provide a strong handle on this background. The standard selection on this value from Ref. [1] is $\chi^2 \leq 15$. This was chosen due to the need to suppress Bhabba + Michel combinatoric background while keeping the most amount of signal decays.

The kinematics of the signal decay means that the combined three-track-momentum vector magnitude at the vertex should equal 0. This is not true for Internal Conversion events or accidental backgrounds, providing a further handle to reject background. The distribution for Internal Conversion and signal events is shown in figure 5.2. As the momentum is the only handle on Internal Conversion the experiment needs to have excellent momentum resolution, the targeted resolution is 1 MeV/c, which as shown in figure 5.3 is achieved. The Internal Conversion distribution is broader than signal as expected, this is due the to missing neutrinos. The step near 15 MeV/c is due to the generator selection. The criterion on the total momentum is also highly effective for reducing the Bhabba+Michel background. The selection from Ref. [1] is $p \leq 4$ MeV/c, this was chosen to suppress both Internal Conversion and Bhabba + Michel combinatoric backgrounds. Although it has a stronger effect for Bhabba+Michel.

The final criterion before the mass selection is the criterion on the lowest track pair mass. The distributions are shown in figure 5.4. This is an effective

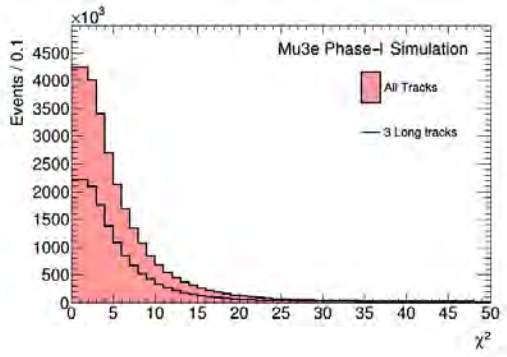

(a) Signal

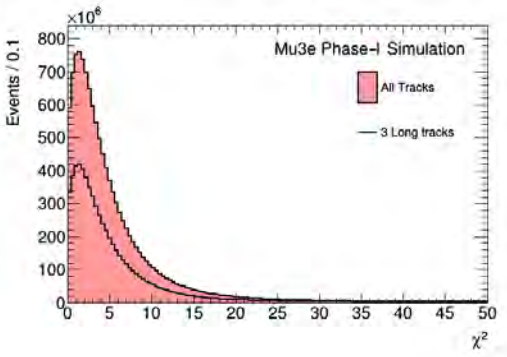

(b) Internal Conversion

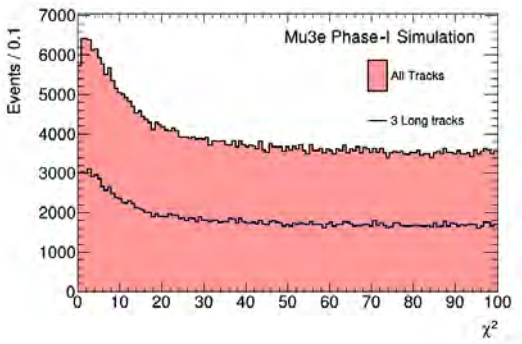

(c) Bhabba and Michel

FIGURE 5.1: The χ^2 distribution for simulated signal, Internal Conversion and Bhabba and Michel events. These have been divided up into all tracks and only 3 long tracks.

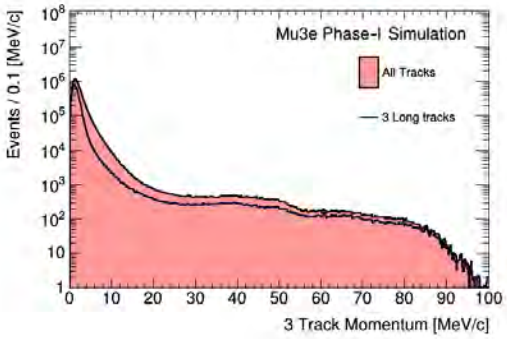

(a) Signal

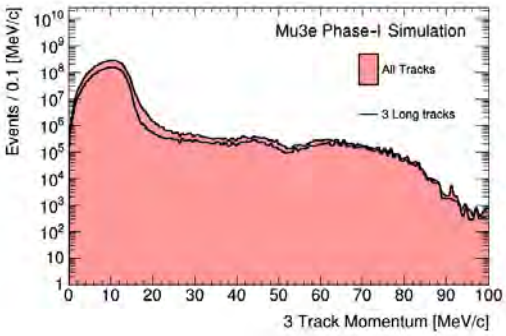

(b) Internal Conversion

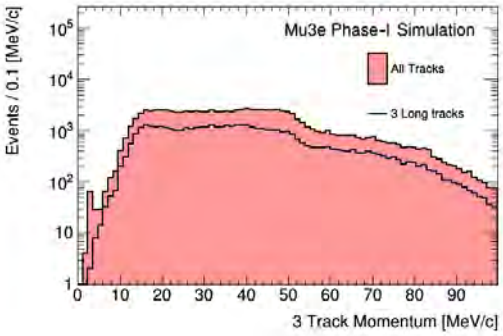

(c) Bhabba and Michel

FIGURE 5.2: The 3 electron momentum distribution for signal (a), Internal Conversion (b) and Bhabba and Michel (c). These have been divided up into all tracks and only 3 long tracks.

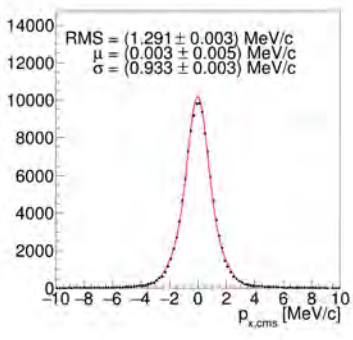

(a)

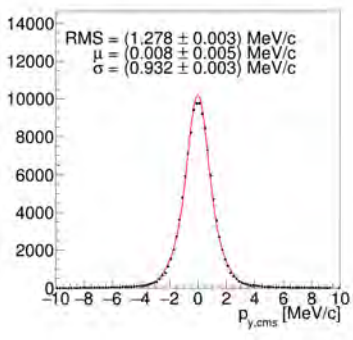

(b)

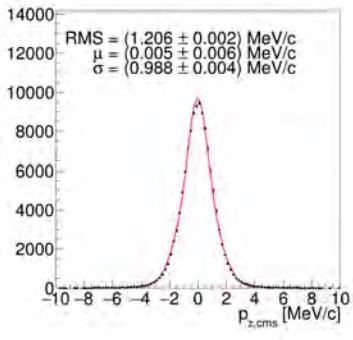

(c)

FIGURE 5.3: The resolution of the total summed momentum for events with 3 long tracks in x (a), y (b) and z (c). Each distribution is fitted with a Gaussian and the fitted parameters shown on the plot.

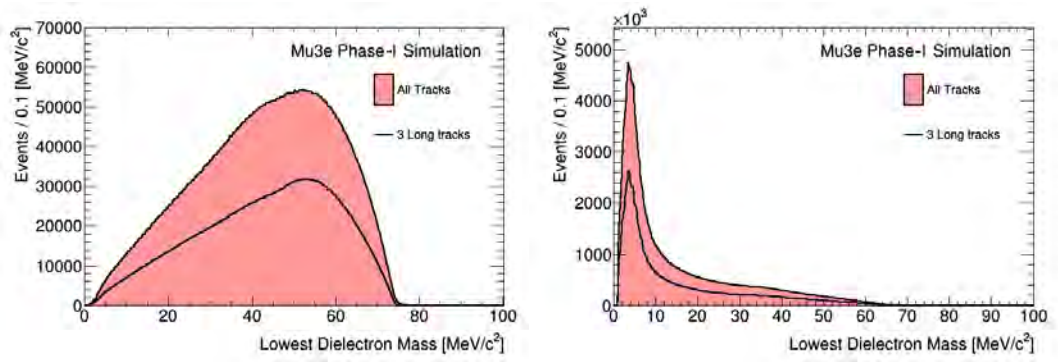

(a) Signal (b) Internal Conversion

FIGURE 5.4: The lowest dielectron mass for signal and Internal Conversion. These have been divided up into all tracks and only 3 long tracks.

criterion in reducing background, because in the signal the track pair masses are generally higher compared to the background of Internal Conversion. The current selection removes events when the lowest 2 track mass is between 5 MeV/c^2 and 10 MeV/c^2. This range was chosen due to the Bhabba + Michel combinatoric background peaking near 7 MeV/c^2 as shown in figure 5.5. This is because Bhabba scattering events with e^+e^- pair mostly originate from a Michel positron close to the Michel edge scattering of a particle at rest [1]:

$$m_{e^+e^-} \approx \sqrt{\frac{2m_e m_\mu}{2}}. \tag{5.1}$$

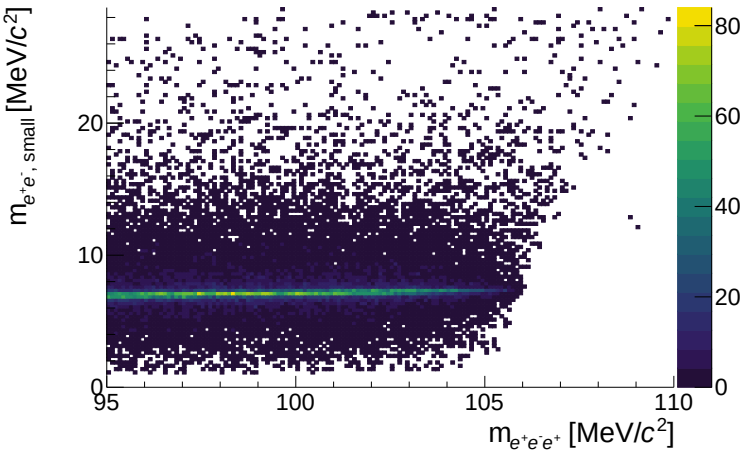

FIGURE 5.5: Small invariant mass of e^+e^- pairs versus $e^+e^-e^+$ invariant mass for accidental combinations of a Bhabha e^+e^- pair with a Michel positron [1].

The most effective criterion finally is on the invariant mass of the 3 track system, this is because the signal invariant mass is equal to the muon rest mass while the mass in Internal Conversion events is lower due to the unobserved neutrinos. This distribution is shown in figure 5.6. As expected, signal events peak at the muon mass. There is a tail to the lower values of the invariant mass, due to individual particles losing energy in the detector due to bremsstrahlung or ionization. For the Internal Conversion events there is a drop off just before the muon mass as expected. When considering all tracks, the distribution does extend above the muon mass. This is due to the poorer mass resolution. The standard criterion used for Ref. [1] is $103 \leq m_{eee} \leq 110$ MeV/c^2.

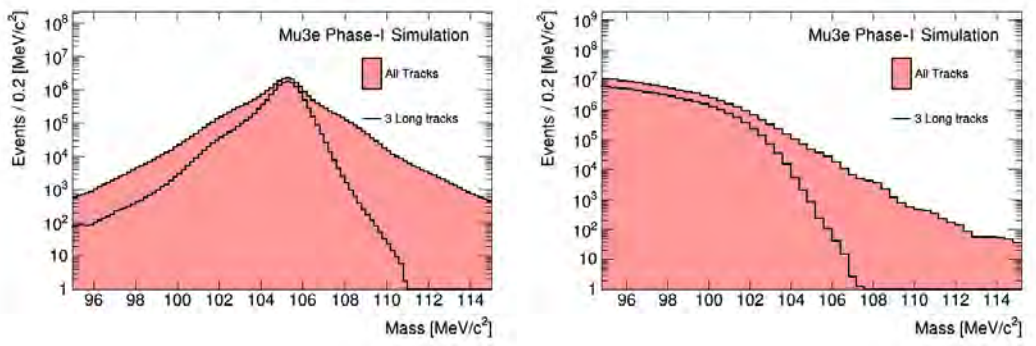

(a) Signal (b) Internal Conversion

FIGURE 5.6: The 3 electron mass distribution for signal and Internal Conversion. These have been divided up into all tracks and events with only 3 long tracks.

The described criteria have been applied to both the signal and the Internal Conversion event samples and the resulting cutflow is shown in table 5.1 and 5.2, respectively. The mass of the 3 track systems is shown in figure 5.7, after the dielectron mass criterion. To better understand the background distribution the events have been scaled with the relevant selection efficiencies. The total scale factor applied is:

$$N_{muon} BR \epsilon_{selection} \epsilon_{timing}. \tag{5.2}$$

In this equation N_{muon} is the number of muon decays on target expected in phase-I, set to 2.5×10^{15}. The efficiency of the timing criteria, ϵ_{timing}, is taken from Ref. [102] to be 90%. The selection efficiency, $\epsilon_{selection}$, is the sum of weights of selected events divided by the sum of weights for all simulated events.

The branching ratio is $(3.4\pm0.4)\times10^{-5}$ [72] for Internal Conversion events and different potential branching ratios are considered for the signal decay.

A scatter plot of the invariant mass against the summed momentum of the 3 track system is shown in figure 5.8. The contours for the signal have been drawn by removing the lowest 5% of the reconstructed muon mass for the 95% contour and the same method for the others. This is done because one of the tracks for these events have a higher than usual energy loss either in the target or first pixel layer, this results in higher reconstructed muon momentum and lower reconstructed mass.

For Internal Conversion events, the number of events in the mass window: 103 MeV/c^2 - 110 MeV/c^2 only considering long tracks, is 0.53 ± 0.02 after 300 days of data taking at the phase-I rate. This can be reduced by considering a mass range of 104 MeV/c^2 - 110 MeV/c^2 which results in 0.052 ± 0.003 events. This includes all cuts down to dielectron cut. This shows that a background suppressed measurement can be achieved if the only background is Internal Conversion. If we consider all tracks the estimated number of Internal Conversion events is 4.914 ± 0.148 in the window 103 MeV/c^2 - 110 MeV/c^2, showing that a background suppressed measurement is not achievable in this case.

Considering next-to-leading order corrections (NLO), differences are typically only at the percent level. However, the effect can be larger in the extreme parts of the phase space where the signal peak is located. In Ref [88] this calculation has been done with special considerations to the Mu3e experiment. This paper shows that corrections to the branching ratio when the neutrinos have energy of less than $20 \cdot m_e$ is -10.1% and if it is less than $10 \cdot m_e$ the correction is -13.2%. This shows that the estimate quoted above is a conservative number that would be lower after higher order corrections.

Criterion	No of Frames $\times 10^8$	Efficiency	Step Efficiency
Generated Number of muon decays	161.1 ± 0.1	-	
$\chi^2 < 15$ All Tracks	109.5	0.680	-
$\chi^2 < 15$ Long Tracks	58.41	0.363	-
3-track system momentum < 4 MeV/c All tracks	4.446	0.0276	0.0406
3-track system momentum < 4 MeV/c Long Tracks	2.404	0.0149	0.0411
$m_{ee} < 5$ or $m_{ee} > 10$ All Tracks	3.382	0.0210	0.761
$m_{ee} < 5$ or $m_{ee} > 10$ Long Tracks	1.835	0.0114	0.764

TABLE 5.1: Selection for simulated Internal Conversion events. Statistical uncertainty are less than 0.01%. This results from the sum of weights and does not represent events for phase-I.

Criterion	No of Frames $\times 10^7$	Efficiency	Step Efficiency
Generated Number of muon decays	8.779	-	
$\chi^2 < 15$ All Tracks	2.762	0.315	-
$\chi^2 < 15$ Long Tracks	1.417	0.161	-
3-track system momentum < 4 MeV/c All tracks	2.427	0.277	0.879
3-track system momentum < 4 MeV/c Long Tracks	1.342	0.153	0.947
$m_{ee} < 5$ MeV/c^2 and > 10 MeV/c^2 All Tracks	2.379	0.271	0.980
$m_{ee} < 5$ MeV/c^2 and > 10 MeV/c^2 Long Tracks	1.316	0.150	0.981

TABLE 5.2: Selection for simulated signal. Statistical uncertainty in this table are less than 0.03%. This results from the sum of weights and does not represent events for phase-I.

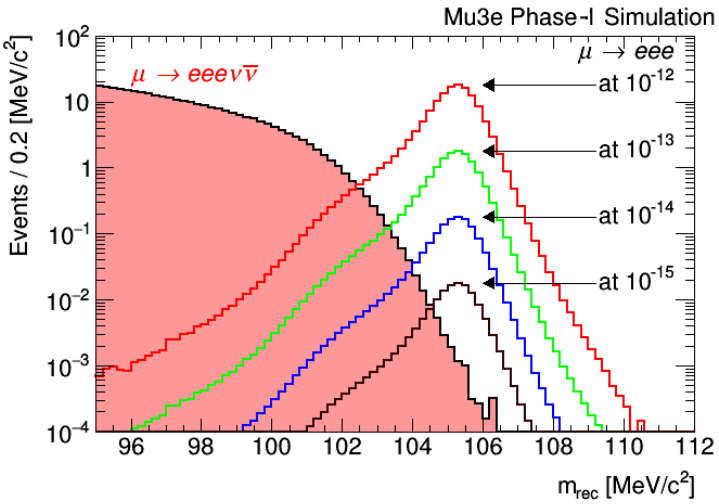

FIGURE 5.7: Three-electron mass distribution, normalised to the phase-I muon-on-target rate.

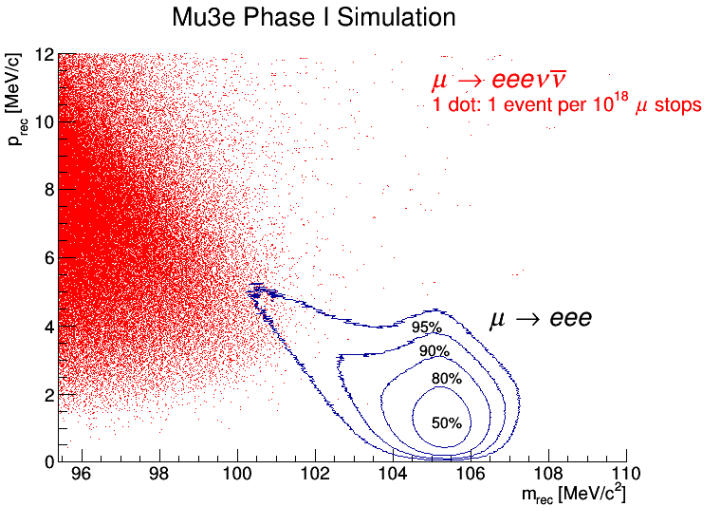

FIGURE 5.8: Scatter plot showing the mass against momentum for Internal Conversion and signal.

Conclusion

This section details the studies done on the signal and Internal Conversion simulation files, it looks at how the reconstruction for these events happen and at the selection criteria used for the analysis with a summary of criteria applied shown in tables 5.1 and 5.2. Once this was completed the details of how we are able to extract the total number of background events we would expect to see in the region 103 MeV/c^2 - 110 MeV/c^2 when only considering long tracks, is 0.53 ± 0.02 after 300 days of data taking at the phase-I rate. The selection criteria that have been detailed for the main study are the same used in Ref. [1].

Chapter 6

Combinatoric background from Internal Conversion pairs and Michel Positrons

This chapter describes a study of one of the main sources of accidental backgrounds in the Mu3e experiment. The background occurs when an e^+e^- pair from an Internal Conversion decay and a Michel positron are reconstructed such that their extrapolated tracks are compatible with a single vertex. This is not the dominant combinatoric background which is from e^+e^- pairs resulting from a Bhabba scatter combined with a Michel positron. The latter has been studied in detail in the TDR and it was found 4 events are expected in the signal mass window after 300 days of phase-I operation [1].
This chapter discusses how these two processes can be misreconstructed as signal-like events. This is followed by a study of the kinematics and an estimate of the number of Internal Conversion and Michel events that are expected in the signal region to establish how important this source of background is.

6.1 Generation and Selection Criteria

To generate the decays that are needed to study this combinatoric background, each frame needs to have at least one or more Internal Conversion decays and a number of Michel positrons. This is done by running the simulation at the full Phase-I rate and forcing one of the muon decays to be an Internal Conversion event. The Internal Conversion decays are generated as described in section 6.3 but without generator level criteria. The Michel positrons are generated using

the Geant4 implementation. The sample generated has 2.305×10^{18} effective muon decays. The selection criteria for good vertices are the same as in section **??**. The selection table is shown in table 6.1.

Cut	No of Frames $\times10^{10}$	Efficiency
Generated Number of muon decays	$(2.02\pm1.77)\times10^{8}$	-
$\geq$1 vertex	7.061×10^{4}	3.492×10^{-4}
$\chi^2 < 15$ All Tracks	$(4.38 \pm 0.76)\times10^{4}$	2.164×10^{-4}
$\chi^2 < 15$ Long Tracks	$(2.11 \pm 0.40)\times10^{4}$	1.043×10^{-4}
3-track system momentum < 4 MeV/c All tracks	3.571 ± 1.205	1.766×10^{-8}
3-track system momentum < 4 MeV/c Long Tracks	0.767 ± 0.548	3.793×10^{-9}
$m_{ee} < 5$ MeV/c^2 and > 10 MeV/c^2 All Tracks	2.015 ± 0.387	9.975×10^{-9}
$m_{ee} < 5$ MeV/c^2 and > 10 MeV/c^2 Long Tracks	0.740 ± 0.547	3.661×10^{-9}

TABLE 6.1: Selection flow for events in the combined Internal Conversion and Michel decay sample.

6.2 Vertex Reconstruction

Tracks contributing to the studied background source do not originate from a single muon decay. This means that an understanding of the distance between the true and reconstructed vertices is needed. Figure 6.1 shows the distance between the true Internal Conversion vertex and the vertex of a Michel decay in the same frame, for different track categories of the Michel positron track. In all cases the three tracks have been combined to a single vertex with $\chi^2 < 15$. This shows that there can be a sizeable distance between the two truth vertices.

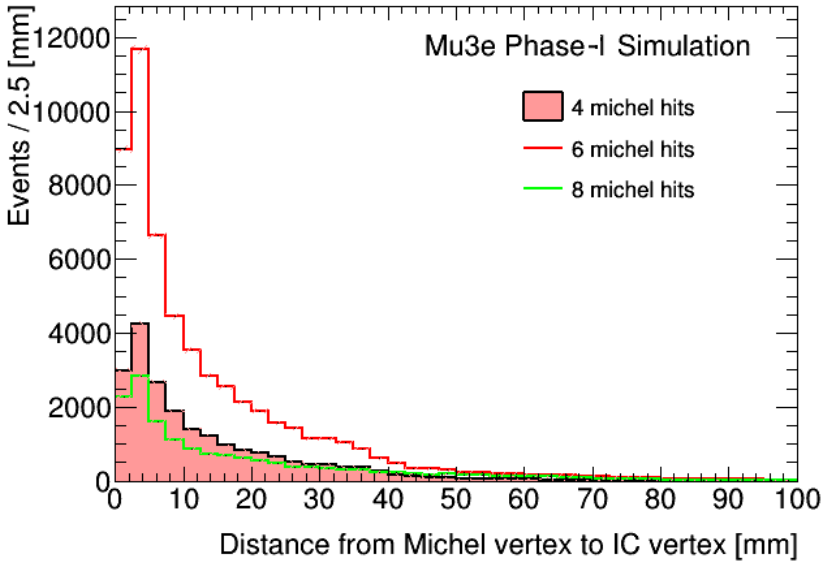

FIGURE 6.1: Distance from the true Michel positron decay point to the true Internal Conversion decay point for Michel positron tracks with 4, 6 or 8 hits.

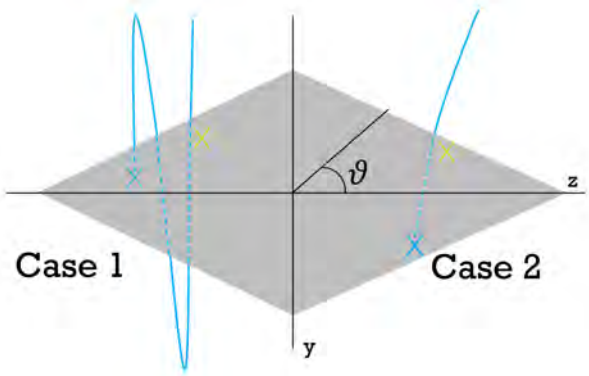

FIGURE 6.2: Distance from the truth Michel positron decay to the truth Internal Conversion decay divided into number of hits of the Michel positron track. The events is the sum of weighted frames for every 2.5 mm, these weights do not correspond to the phase-I values.

There are two main reasons why this can happen. For instance the particle can pass through the opposite side of the target before hitting any silicon pixel layers (Case 2 in figure 6.2). The track direction can also be misreconstructed if the particle passes through the target multiple times (Case 1 in figure 6.2). The latter is most likely to happen if particles have a high angle with respect to the beam.

The distribution of the angle with respect to the beam for the Michel positron is shown in figure 6.3, for events with a selected reconstructed vertex and with

large or small distance between the conversion pair and Michel electron true vertices. This indicates that a large angle with respect to the beam increases the probability of tracks from separate decay points to be reconstructed as originating from a single vertex.

To further examine the distance from the truth vertex to the track we will only consider the transverse plane for the Michel positron. A diagram is shown in figure 6.4(A) showing the reconstructed 3 track vertex and the truth Michel vertex. If our explanation for the behaviour seen in figure 6.2 is correct we could expect the extrapolated track to pass very close to the truth Michel vertex location at some point along its trajectory. This would mean that there is a relation between θ and d/R and we would expect d/R to be near 0. The distribution of d/R for the Michel positrons is shown in figure 6.4(B), it is shown for the simulation and for different values of d_0/R. These distributions indicate that the distance from the truth vertex to the track is normally small for simulation. However, when the angle θ is random values d/R tends towards unity.

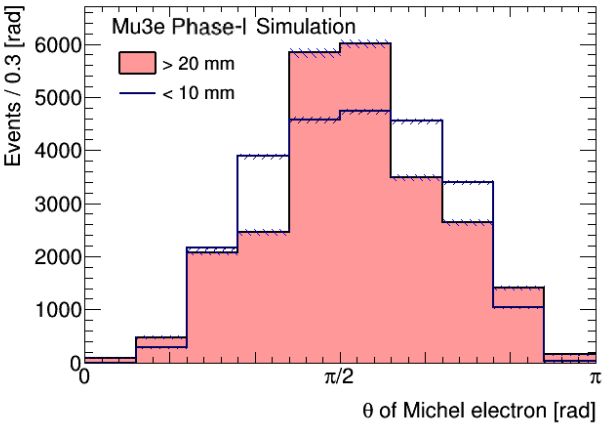

FIGURE 6.3: θ angle of Michel positrons particle from the combined sample for case where the distance of closest approach to the reconstructed vertex is less than 10 mm or greater than 20 mm.

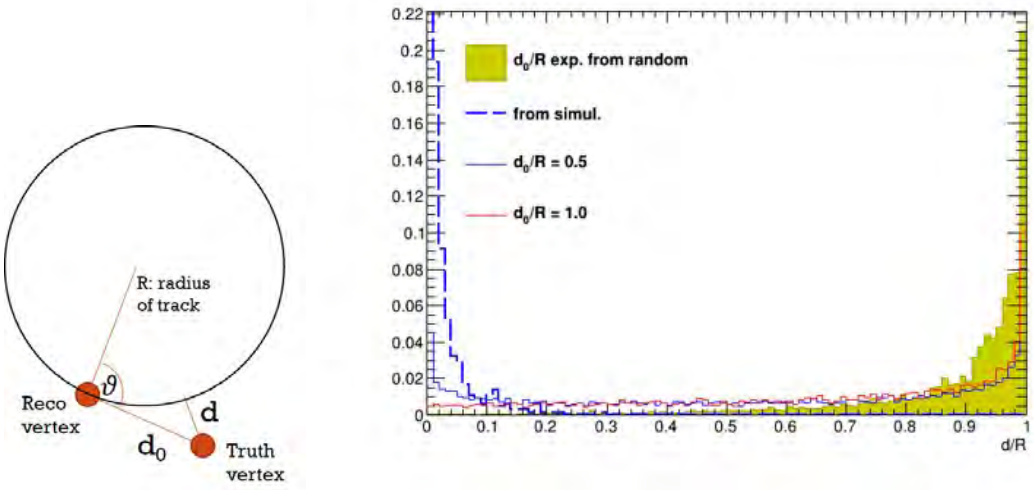

(a) (b)

FIGURE 6.4: Comparing whether it is more probable for the truth vertex to be closer to the track than the reconstructed vertex. If the track often passes close to the truth vertex, we would expect d/R to be close to 0, which is seen in the simulation. The plot has been normalised to 1 and only shows the region we are interest in.

6.3 The Vertex Weight

When examining the distributions produced for the vertex variables it was noted that there are some frames with very large weights. These weights are the generator weights (the matrix element and the phase space weight, see section). As the Michel positrons have a constant weight, this is appeared likely to be due to the Internal Conversion weights. As seen in chapter 5 high weights were not seen in the Internal Conversion sample used there. The distributions of the weights for both Internal Conversion and the combinatoric background is shown in figure 6.5. These distributions show that the combinatoric background has higher weights than the Internal Conversion only sample.

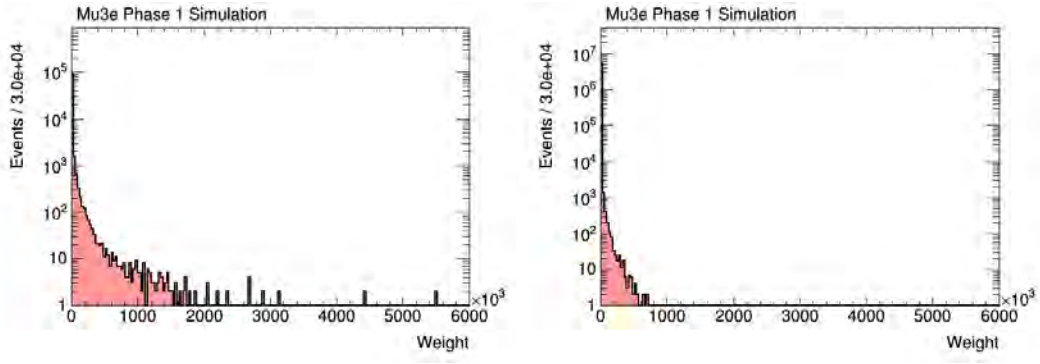

(a) Internal Conversion and Michel sample

(b) Internal Conversion sample

FIGURE 6.5: Weights of each frame for both the Internal Conversion sample (a) and Internal Conversion and Michel sample (b).

To further examine this increase in weights the kinematics of the Internal Conversion simulation were examined. To do this we split simulated events into two samples, one with event weights greater than 500×10^3 and the other with the remaining events. In the Internal Conversion sample from chapter 5 we only examined the region where the neutrinos have very little energy. However, this is no longer a requirement in this combinatoric background sample. It was studied whether high weighted events happen only at higher neutrino energies. To examine this, the distribution of neutrino momenta is shown in figure 6.6, this indicates that high weight events also occur at low neutrino energies.

The next hypothesis that was examined was whether there is colinear soft photon emission. The distribution of the angle between the photon conversion and the positron is shown in figure 6.7. These distributions support this hypothesis as all high-weight events have an angle lower than 1 rad while the standard distribution ranges from 0 - π rad. This indicates that the photon is emitted along the same direction of the positron.

With the source for the high weights identified we examine why this isn't seen in chapter 5. The mass distribution of the vertex is plotted for the high weight Internal Conversion events and for all other events (see figure 6.8). This shows that the high-weight events are not in the mass region of interest for the Internal Conversion background. However, with the additional Michel positron included in the reconstruction it pushes these events towards the mass region of interest for the combinatoric background case.

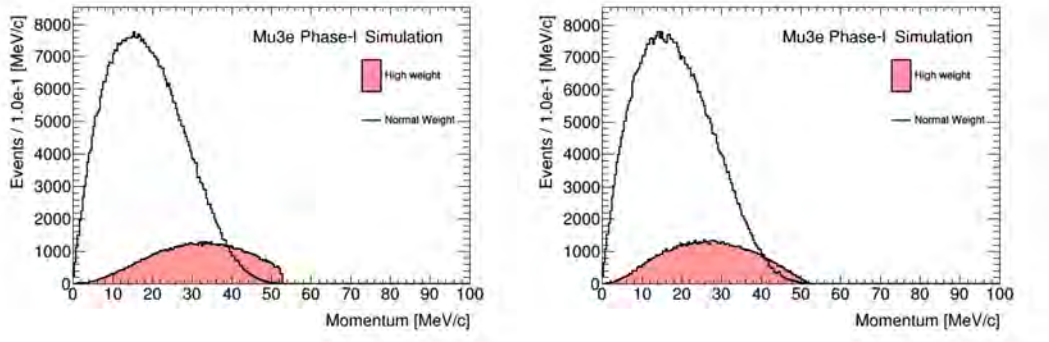

(a) ν_μ (b) ν_e

FIGURE 6.6: Neutrino momentum from a truth simulation from the Internal Conversion comparing high weighted events to normal weight.

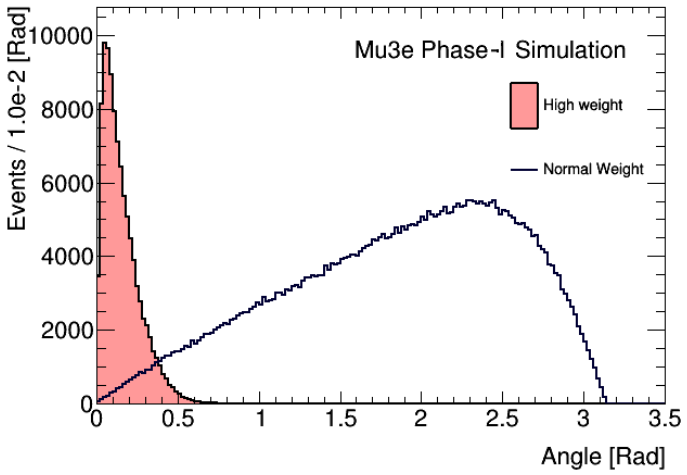

FIGURE 6.7: The angle between the photon conversion and the Michel positron of the simulated Internal Conversion event, comparing high weight events to the normal weight event.

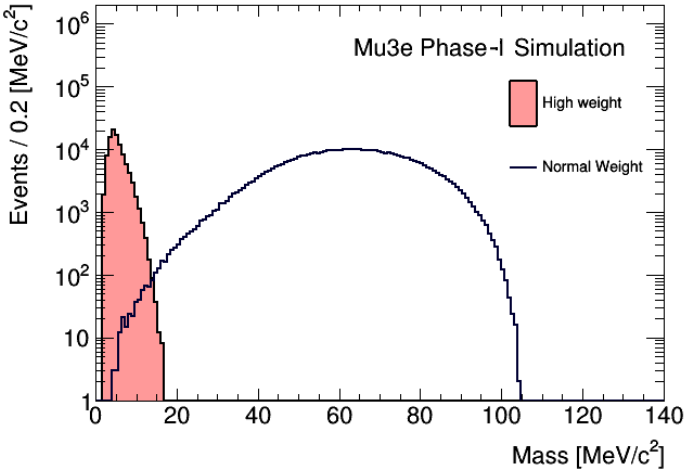

FIGURE 6.8: Reconstructed muon mass of the positron and conversion pair of the Internal Conversion decay for high weight events and all events.

6.4 Normalisation

The main purpose of this study is to estimate the number of expected events inside the signal mass region. To do this we need to scale the generated weighted events to the total number of phase-I muon decays. If a criterion based selection was applied no events would survive the full selection criteria. Therefore instead, events are kept but scaled with the relevant selection efficiencies. The total scale factor applied is

$$\text{Scale} = N_{muon} BR\, \epsilon_{sel}\, \epsilon_{timing}. \tag{6.1}$$

Where N_{muon} is the phase-I target number of 2.5×10^{15} muon decays. The selection and reconstruction efficiency, ϵ_{sel}, is calculated from the number of simulated frames. The timing efficiency, ϵ_{timing}, is taken from Ref. [102] and is 0.7. The branching ratio used is $(3.605 \pm 0.001) \times 10^{-5}$ [103].

The timing information allows for additional background suppression, which is particularly effective for combinatoric backgrounds. The suppression achieved for 2 correlated tracks and one uncorrelated track is a factor 70 while the timing efficiency for a genuine vertex with 3 correlated tracks is 90% [1]. The branching ratio used for this combinatoric background is that of the Internal Conversion decays since the Michel rate is close to 1. Which is already accounted for by the number of muon decays generated per frame. To summarise, the selection criteria are all accounted for by scaling, apart from the selection of the mass

region of interest. The mass histogram is then scaled according to equation 6.1 leading to figure 6.9, which applied to events with three tracks with at least 6 hits each. The plot shows that there are a total of $(2.15 \pm 0.48) \times 10^{-5}$ background events in the mass range of 103 - 110 MeV/c^2. In the mass range 104 - 110 MeV/c^2, the number of events is $(1.22 \pm 0.28) \times 10^{-5}$.

Conclusion

This section details the second most dominant source of combinatoric backgrounds expected in the experiment, the combination of Internal Conversion pairs and Michel positrons. This details the criterion flow used and how this sample was generated. It then moves to explaining the multiple different methods that these decays can be combined into one 3 track system. It was also found that the weight for this combinatoric sample was for a high number of events significantly larger than pure Internal Conversion. It was found that it was due to the photon being emitted along the same direction of the electron for the Internal Conversion event. Finally this chapter gives an estimated number of events in the mass region 103 - 110 MeV/c^2 of $(2.15 \pm 0.48) \times 10^{-5}$.

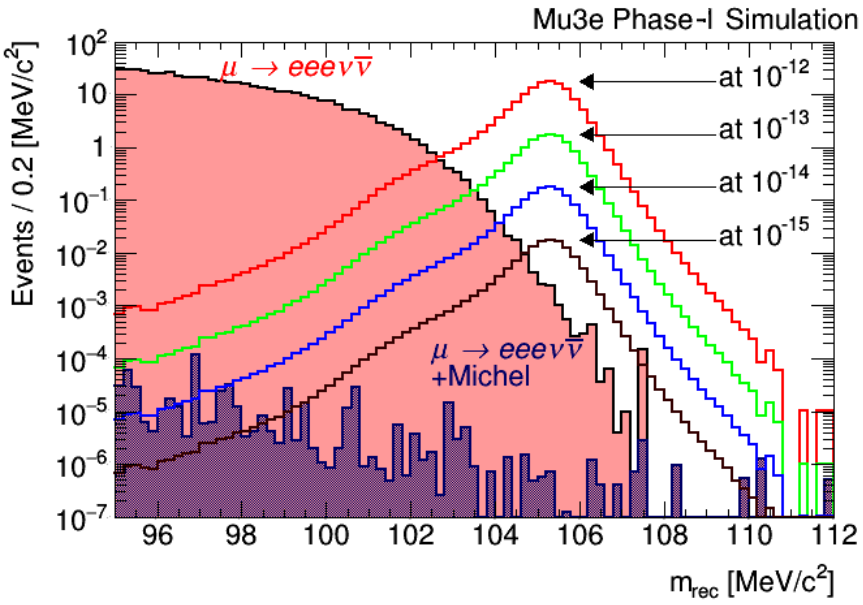

FIGURE 6.9: Mass plot showing the Internal Conversion background alongside the Internal Conversion and Michel combinatoric background. This plot also shows the signal decay with varying branching ratios.

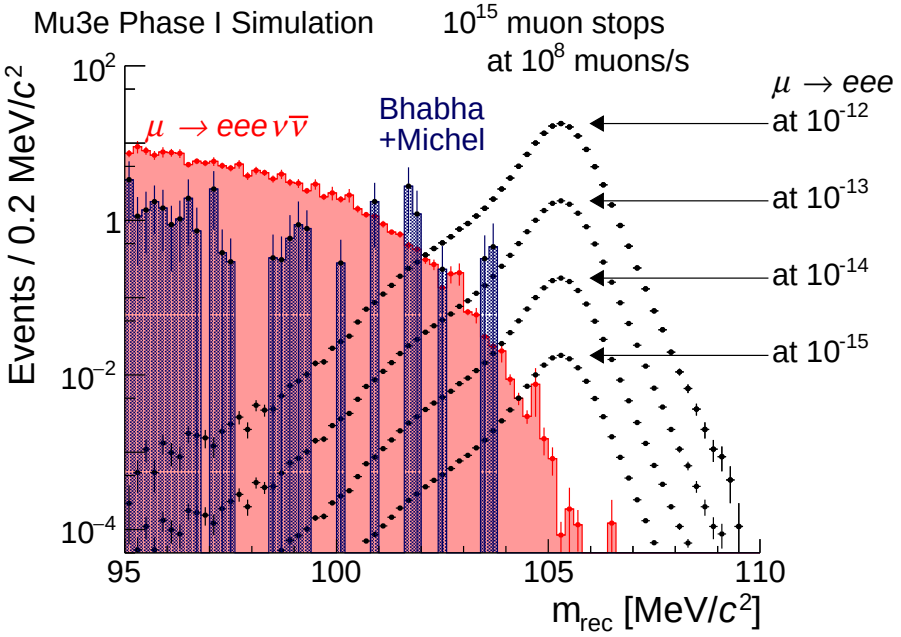

FIGURE 6.10: Mass plot showing the Internal Conversion background alongside the Bhabba and Michel combinatoric background. This plot also shows the signal decay with varying branching ratios. This plot is taken from Ref. [1]. The Bhabba and Michel combinatoric background statistics was limited by computing power available at the time.

Chapter 7

Combinatoric Background of Photon Conversion pairs and Michel Positron

This chapter details the study of cases where electron positron pairs from a photon conversion have a vertex which is compatible with the track of a Michel positron. Such an arrangement can cause the reconstruction of a signal-like signature. This chapter will detail how the photons are generated and it will estimate the number of such events estimated in the signal region.

7.1 Generation

To be able to investigate this background a large number of photons needs to be simulated. These photons come mainly from radiative muon decays, $\mu \to e\gamma\nu\overline{\nu}$, however there are other small sources such as Bremsstrahlung or electron positron annihilation. As the main source of photons are radiative muon decays, this is how this background was simulated. The simulation was done by forcing one of the muons in each frame to decay via the radiative decay with the rest being normal muon decays at the full phase-I rate, as described in section 2.4.3. This allows for a number of Michel positrons to be produced as well as a photon in each frame that may convert in the detector.

This study focuses on the high end of the photon conversion momentum spectrum, so it is useful to investigate a generator criterion on the energy of the photon. Due to the acceptance of the detector, a particle must have a transverse momentum of greater than 10 MeV/c to be detected. This means that

a photon must have a minimum energy of 20 MeV which for radiative muon decays has a branching ratio of $(3.3 \pm 1.3) \times 10^{-3}$ [104]. This was first measured in 1961 with the most recent result for this decay coming from the MEG collaboration [105] in 2016. MEG founds a value of $(6.03 \pm 0.14 \pm 0.53) \times 10^{-8}$, photon energies greater than 40 MeV and a $E_e > 45$ MeV. The values found by MEG is in agreement with the theoretical value of 6.15×10^{-8} for the same phase space [54].

A simulated sample is employed to test generator level criteria to confirm if the generator criterion performs a useful pre-selection. As only final state particles are retained in the event file, the photon energy must be reconstructed from the conversion particles. This distribution is shown in figure 7.1, to further check this stage a simulation with a 25 MeV photon energy criterion off was also done. The distribution shown does depend on the detector acceptance, but no other selection criteria are applied. This again shows good agreement and confirms the generator criterion can be used. The lower tail in the $E_\gamma > 40$ MeV distribution comes from electrons being mis-reconstructed.

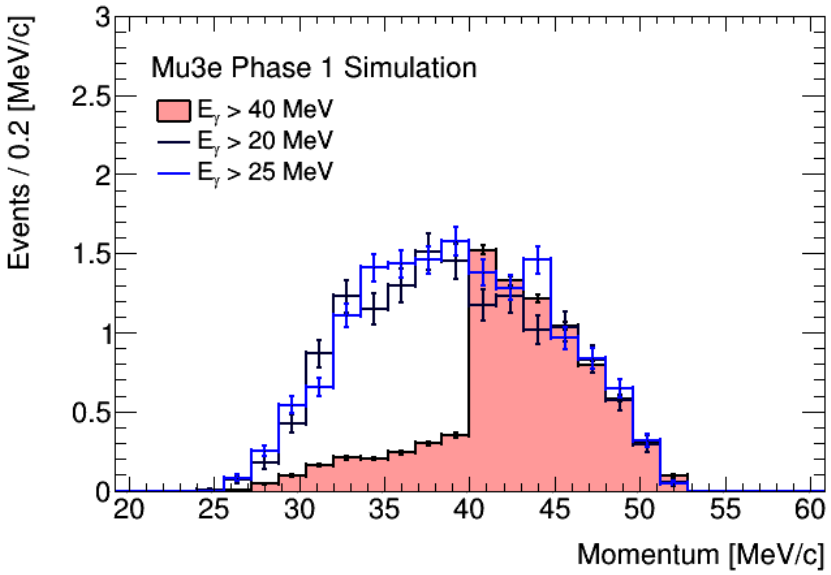

FIGURE 7.1: Photon energy for different photon energy generator criteria after the vertex reconstruction stage when simulating radiative muon decay. The photon momentum is reconstructed from truth e^+e^- pair without any selection to remove miss reconstructed tracks. However the tracks must fall in the acceptance of the detector.

Confirming that the generator criterion performs correctly is important, but

the generator criterion also needs to cover the desired phase space. To do this we need to examine how the reconstructed 3 track system, combination of 2 positrons and 1 electron, mass and momentum behaves with photon energy. These plots are shown in figure **??**. It should be noted that the sample with a criteria of 25 MeV was used as figure 7.1 shows very few photons with an energy lower than 25 MeV. There is no significant difference in the predicted number of events in the signal region between the samples with a different photon energy criterion, indicating the 40 MeV generator criteria can be applied safely.

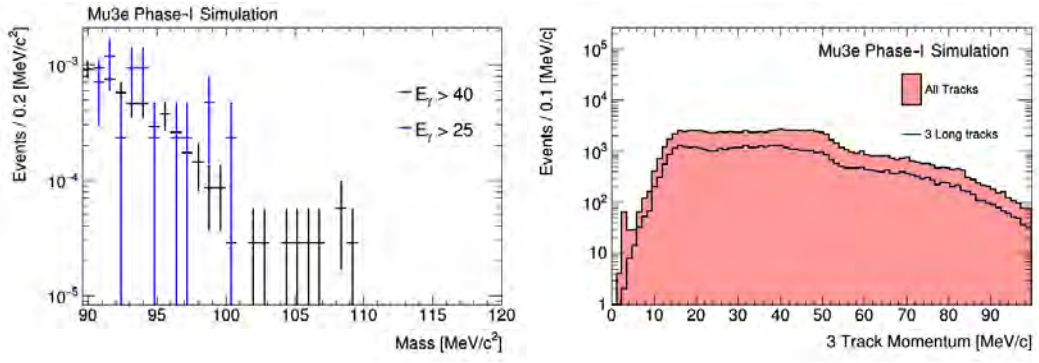

(a) (b)

FIGURE 7.2: 3 track mass (a) and momentum (b) for simulation with generator criteria on the photon energy of 25 and 40 MeV. These plots have been normalised. The photon energy of 40 MeV simulation has more statistics due to it being used for the final analysis.

To limit required disk space due to the large samples needed, a pre-selection on the position where the photon converts is made. In the simulation the photon conversion position has been plotted for the full detector and for a zoomed-in view around the target. These are shown in figure 7.3. The large band at the top of figure 7.3 (a) is the detector solenoid and the rest of the detector and support structures can also be seen. The photon conversion position for events in which the generated e^+e^- pair passes the track and vertex reconstruction and selection, is shown in figure 7.4. The mean and standard deviation at this stage for x, y and z are 0.19, -0.58 and 2.14 for the means, and 16.38, 10.65 and 15.71 for the standard deviation, respectively. This shows that a selection can be performed to only retain a subset of frames where the photon is converted in an area of interest. The selection chosen is very loose, requiring the absolute

value of z to be less than 200 and r to be less than 100. This removes photon conversion in beam pipe and recurl stations as well as in the magnet. The study helps us understand the properties of the photon and their effect on the reconstructed 3 track system and allows for a more efficient sample of 14.5 billion frames, before the conversion region criteria, to be generated.

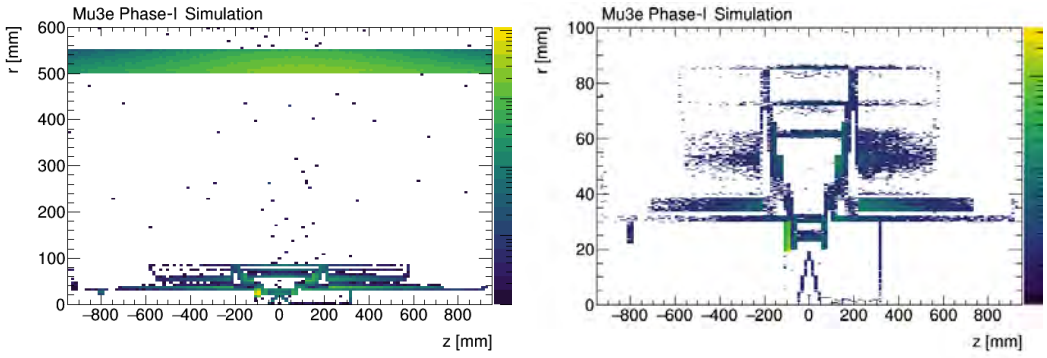

(a) (b)

FIGURE 7.3: Position where the photon converts in the detector after the simulation stage. In (a) the large bar at the top is due to the magnet.

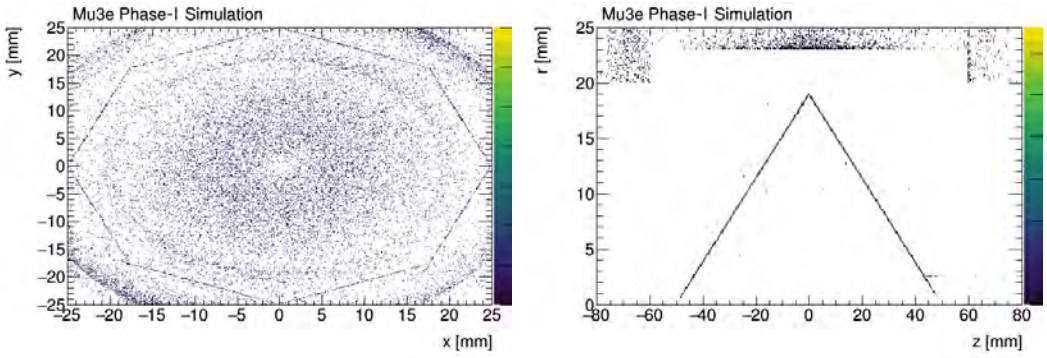

(a) (b)

FIGURE 7.4: Position where the photon converts in the detector for frames in which 3 long tracks are reconstructed. This is done after the χ^2 criterion.

7.1.1 Event estimate

The selection criteria for good vertices are the same as in section 5.2.1. A criterion flow for this sample is shown in table 7.1. This combinatoric background is suppressed heavily by the momentum selection with only two events passing, however these events have a low reconstructed vertex mass. This can be seen

criterion	No of Frames $\times 10^3$	Efficiency
Generated Number of muon decays	1.45×10^7	
$\geq$1 vertex	1.039×10^3e+03	7.135×10^{-5}
$\chi^2 < 15$ All Tracks	146.8	1.008×10^{-5}
$\chi^2 < 15$ Long Tracks	97.64	6.705×10^{-6}
3-track system momentum < 4 MeV/c All tracks	0.004	2.747×10^{-10}
3-track system momentum < 4 MeV/c Long Tracks	0.002	1.373×10^{-10}

TABLE 7.1: Selection criterion flow for events in the combined Photon Conversion and Michel combinatoric decay sample. No events pass the dielectron mass criterion.

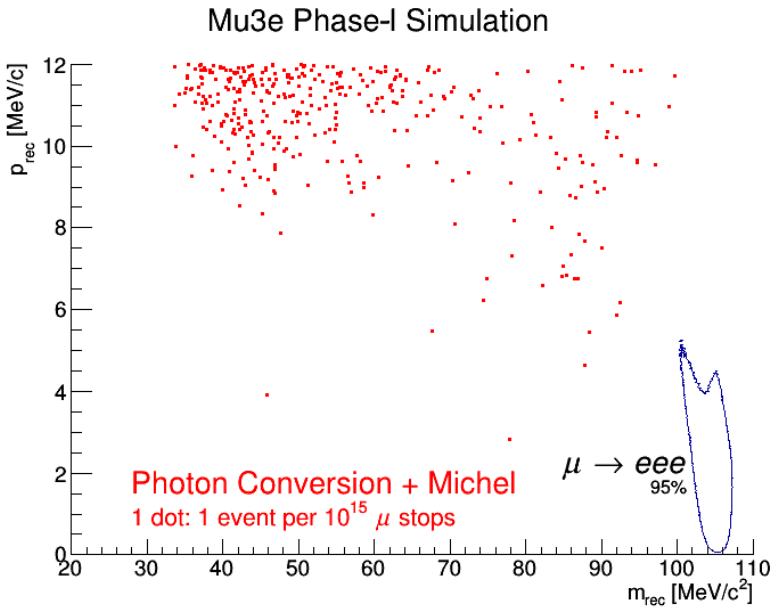

FIGURE 7.5: Mass momentum scatter plot for the reconstructed 3 track system after the χ^2 criterion for 3 long tracks. The figure shown has been limited to the momentum region of the signal, there are combinatoric decays with a higher p_{rec} than 12 MeV/c.

more clearly by the distributions of momentum and the reconstructed vertex mass shown in figure 7.5. As this shows that no reconstructed event lies inside the mass and momentum window, only an upper limit on the number of expected vertices can be set. To find this upper limit we need to extrapolate the efficiency for the mass criterion and the momentum criterion separately after the χ^2 criterion, using this method we will be able to set a loose upper limit.

The distribution of this efficiency for various different momentum criteria is shown in figure 7.6. The efficiency for the momentum criterion has been found by fitting the last 3 points of figure 7.6 with a exponential obtaining a value of $(3.62 \pm 0.66) \times 10^{-5}$ with uncertainties assumed to be Poisson. As a cross check

the efficiency distribution has also been created for the samples with different photon energy generator criteria. An exponential fit was performed on these distributions. The results of these fits are consistent with all samples.

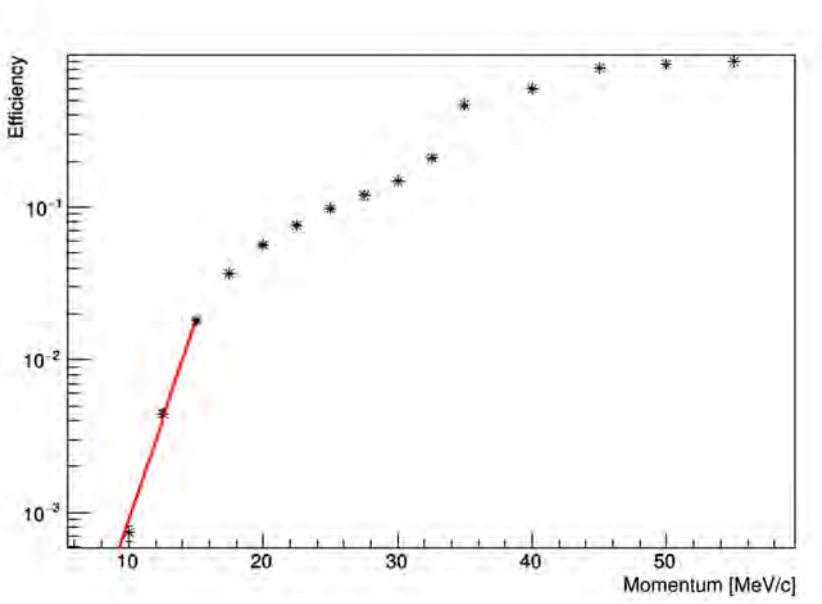

FIGURE 7.6: Background rejection factor for photon conversion and Michel combinatoric background for different momentum criterion. The last 3 points have been fitted with a exponential function.

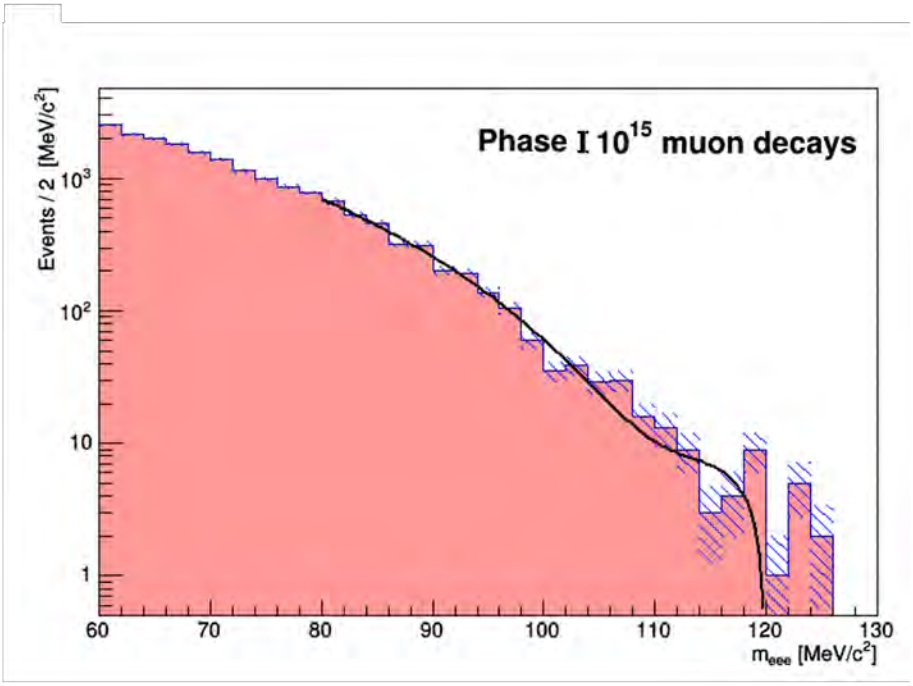

FIGURE 7.7: Mass of the reconstructed 3 track system. This is after the χ^2 criterion.

The rejection power of the mass window selection criterion by counting events is $(9.93 \pm 1.04) \times 10^{-4}$ and the mass plot, for all events after the vertex χ^2 criterion, is shown in figure 7.7. This value has been found using the integral of the distribution, however a 3^{rd} degree polynomial has also been fitted, yielding a consistent result.

This results in a maximum number of events during phase-I in the final mass window of 103 - 110 MeV/c^2 1.161×10^{-7} at a 95% confidence level indicating that this is a negligible source of background. If we were to consider phase-II of the experiment as well, it can be estimated that this background will increase by a factor of 400 assuming identical detector performance. This will still not bring this background to an observable level.

7.2 Sensitivity

Due to the background being suppressed to below 1 for the mass range 104 - 110 MeV/c^2 we are able to define the single event sensitivity for this experiment to be,

$$B_{SES}(\mu \longrightarrow eee) = \frac{1}{\epsilon N_\mu}. \tag{7.1}$$

This equation uses the number of muon decays on target (N_μ) for a certain number of data taking days and the efficiency, ϵ, to reconstruct signal events. The equation gives the branching ratio for which SES sensitivity can be achieved. This allows the experiment to calculate the sensitivity as a function of the number of days of phase-I operation. If no signal events are found, an upper limit can be set on the branching ratio for a desired confidence level.

$$B_{(1-\beta)CL}(\mu \longrightarrow eee) = \frac{-\ln \beta}{\epsilon N_\mu} \tag{7.2}$$

This assumes a Poisson distribution of events in the signal mass region. Figure 7.8 shows the evolution of the branching ratio limit over data taking time, this shows that the experiment will surpass the previous limit set, by SINDRUM, very quickly and can reach the single event sensitivity of 2×10^{-15} within 400 days of data taking. This corresponds to a 90% confidence level exclusion of a branching ration of 5×10^{-15}, in the absence of events in the signal window.

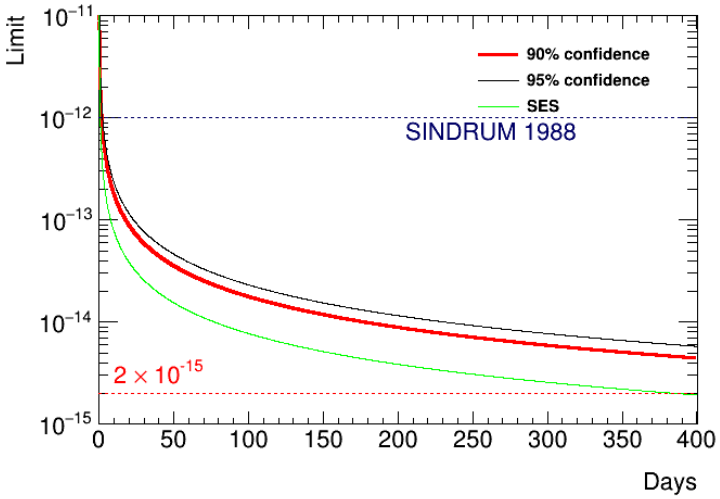

FIGURE 7.8: Single event sensitivity (SES) for phase-I rate.

7.2.1 Selection optimisation

The selection criteria that have been used during this thesis have been defined manually in Ref. [1] to reduce the contamination of Bhabba + Michel background to 0 in the signal mass region of 104 - 110 MeV/c^2. This section will aim, to optimise the selection by maximising the signal significance, which is defined as:

$$Z = \sqrt{2\Big((s+b)\ln\Big(1+\frac{s}{b}\Big) - s\Big)}, \tag{7.3}$$

which is taken from the asymptotic formula for significance [106].

Background rejection is the fraction of all background events that are rejected. This will be done for the optimisation of each selection criterion.

Internal Conversion cannot be reduced by optimising the vertex χ^2 criterion, as tracks all originate from a single vertex, like for the signal. All other criteria are optimised using the Internal Conversion sample as background. The vertex χ^2 criterion will be optimised using the Bhabba + Michel background. Figure 7.9 shows the vertex χ^2 significance plot and indicates that the optimal criterion is 20.

Figure 7.10 shows the absolute momentum significance plot. This shows that for the rejection of Internal Conversion events the optimal criterion is 6 MeV/c. This is higher than in Ref [1] as this criterion was chosen to also help reduce the combinatoric background from Bhabba + Michel events. The significance plot for this background source is shown in figure 7.11. This also shows a criterion

of 6 MeV/c to be optimal.

As the dielectron criterion is double sided there are 2 values that need to be optimised. For the lower criterion optimisation the higher criterion of 10 MeV/c^2 is kept constant while the lower criterion ranges from 0-7 MeV/c^2. For the higher criterion the lower criterion of 5 MeV/c^2 was kept constant while the higher criterion ranges from 10–23 MeV/c^2. This leads to the optimal rejected range for the lowest dielectron mass is 1 - 19 MeV/c^2.

The final selection to be optimised is the mass window requirement. The lower side of the window is optimised without considering an upper limit and shows that 104 MeV is optimal, this means that the mass window will not change i.e. the Ref [1] requirement is already optimal. For the higher mass criterion a lower limit of 95 MeV/c^2 was set and the higher criterion varied. This leads to a plateau of significance starting around 110 MeV/c^2 meaning the upper criterion does not require to be changed.

After this optimisation the only selection to change is dielectron mass window, which leads to a reduction of the signal efficiency by 0.004% and a reduction in the Internal Conversion efficiency from 1.149% to 1.141%. This reduces the event estimate in the mass region of 103 - 110 MeV/c^2 to 0.50 ± 0.002 events while the event estimate in the region 104 - 110 MeV/c^2 to be 0.051 ± 0.007 events.

For the Internal Conversion and Michel background Taking a new event estimate for the region 103 - 110 MeV/c^2 is $(1.02 \pm 0.6) \times 10^{-5}$ and $(8.9 \pm 5.8) \times 10^{-6}$ for the range 104 - 110 MeV/c^2. This is of particular importance, for phase-II when the rate of combinatoric backgrounds will increase.

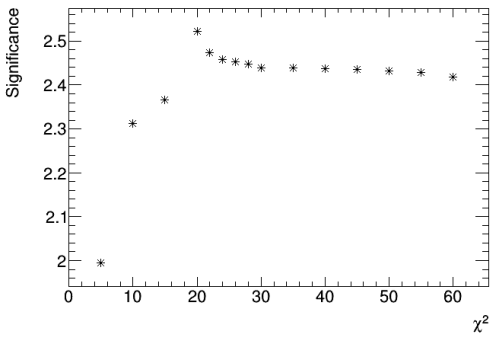

FIGURE 7.9: The significance plot for χ^2 of the vertex.

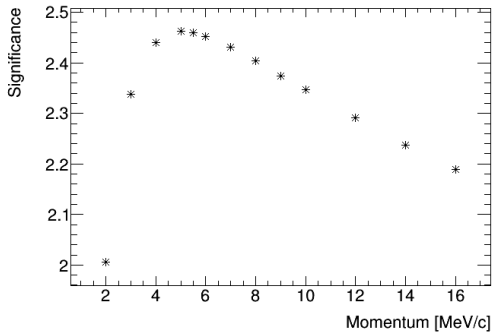

FIGURE 7.10: The significance plot for absolute momentum of the vertex.

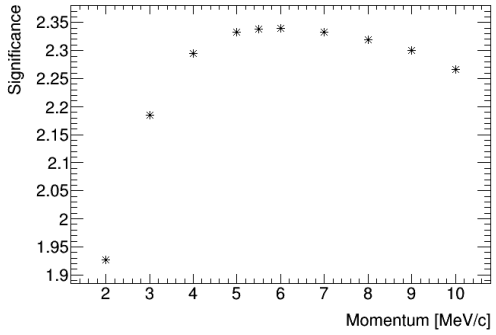

FIGURE 7.11: The significance plot for absolute momentum of the vertex for the background of Bhabba and Michel.

Chapter 8

Conclusion

The Mu3e experiment is dedicated to the search for the decay $\mu^+ \to e^+e^+e^-$ with a sensitivity of 10^{-16} using the world's most intense muon beam as PSI in Switzerland. This decay violates lepton flavour conservation and is strongly suppressed in the Standard Model, however there are many beyond models that do predict some level of flavour violations making this decay a great indicator for new physics.

There are many challenges to measuring this decay with this sensitivity, we need a detector with a large acceptance that is capable of recording up to 2×10^9 muon stops per second. We also need excellent momentum, space and time resolution to reduce background levels to below the 10^{-17} level. Another challenge is that due to low momentum of the decay electrons the dominant source of the momentum uncertainty is multiple scattering. This thus requires a very strict material budget. To be able to achieve this, a long cylindrical pixel tracker design has been adopted using HV-MAPS sensors thinned to 50 μm for the pixel tracker. This not only provides the material budget needed but also allows for the granularity and rate capability needed. This thesis summarised the development of the outer pixel tracker construction methods. It develops the methods of securing the pixel ladders to the endpieces to form the pixel modules and then quality assurance tests.

The first silicon heather chip ladders should arrive from Oxford by summer 2022, this will allow the first module to be constructed that is mechanically the same of the final modules. After these modules are constructed ladders with MuPix10 chip, however to allow these to be produced only every second chip is able to read out due to configuration issues. These problems will be solved for MuPix11 which was submitted at the start of 2022.

In the summer of 2021 a milestone for the experiment happened with the first integration run completed. The modified inner pixel layers where constructed with MuPix10 on a PCB rather than the HDI, due to the same configuration issues, and was mounted inside the magnet with a number of the fibre modules. The muon beam was then fired at the target and data was taken. This is the first time modules are mounted inside the magnet and data taken with the beam. It allowed the testing of the readout as well as the fibre and pixel detectors. At the time of writing the data was still being taken.

At the conclusion of this thesis all the major potential background sources have been studied, this thesis proved that the only background source to be aware of is the Bhabba and Michel combinatoric. The background from internal conversion and the combinatoric background of internal conversion and Michel positron do not sum up to 1 event in the signal mass region for 300 days of data taking. This thesis also showed that the cuts defined in Ref. [1] have room for improvement, thus there is still room for reducing the background further.

The Mu3e experiment is on track to start taking data in 2024 for phase-I which includes both recurl stations. Phase-II of the experiment requires the new high intensity muon beam line which will start being installed in 2027, this should be after the completion on phase-I. It will also require new pixel detectors to include increase the timing while the fibre detector will be removed to reduce the material budget.

Bibliography

[1] K. Arndt et al. Technical design of the phase I mu3e experiment. *Nuclear Instruments and Methods in Physics Research Section A: Accelerators, Spectrometers, Detectors and Associated Equipment*, 1014:165679, 2021.

[2] Murray Gell-Mann. A Schematic Model of Baryons and Mesons. *Phys. Lett.*, 8:214–215, 1964.

[3] S. Tomonaga. On a relativistically invariant formulation of the quantum theory of wave fields. *Prog. Theor. Phys.*, 1:27–42, 1946.

[4] Anthony J.G. Hey Ian J.R. Aitchison. *Gauge Theories in Particle Physics: A Practical Introduction*. CRC Press, Boca Raton, 2013.

[5] E. Fermi, E. Teller, and V. Weisskopf. The decay of negative mesotrons in matter. *Phys. Rev.*, 71:314–315, Mar 1947.

[6] W. Pauli. Dear radioactive ladies and gentlemen. *Phys. Today*, 31N9:27, 1978.

[7] Florian Nortier. *Dimension spatiale supplémentaire compactifiée et champ de Higgs branaire*. PhD thesis, U. Paris-Saclay, 2020.

[8] H. Fritzsch, Murray Gell-Mann, and H. Leutwyler. Advantages of the Color Octet Gluon Picture. *Phys. Lett. B*, 47:365–368, 1973.

[9] R P. Feynman. Very high-energy collisions of hadrons. *Phys. Rev. Lett.*, 23:1415–1417, 1969.

[10] R.D. Field and R.P. Feynman. A Parametrization of the Properties of Quark Jets. *Nucl. Phys. B*, 136:1, 1978.

[11] Julian S. Schwinger. On Quantum electrodynamics and the magnetic moment of the electron. *Phys. Rev.*, 73:416–417, 1948.

[12] R.P. Feynman. Space-time approach to nonrelativistic quantum mechanics. *Rev. Mod. Phys.*, 20:367–387, 1948.

[13] R.P. Feynman. The Theory of positrons. *Phys. Rev.*, 76:749–759, 1949.

[14] R.P. Feynman. Mathematical formulation of the quantum theory of electromagnetic interaction. *Phys. Rev.*, 80:440–457, 1950.

[15] Carl D. Anderson. The positive electron. *Phys. Rev.*, 43:491–494, Mar 1933.

[16] J. H. Christenson, J. W. Cronin, V. L. Fitch, and R. Turlay. Evidence for the 2π Decay of the K_2^0 Meson. *Phys. Rev. Lett.*, 13:138–140, 1964.

[17] C. S. Wu, E. Ambler, R. W. Hayward, D. D. Hoppes, and R. P. Hudson. Experimental Test of Parity Conservation in β Decay. *Phys. Rev.*, 105:1413–1414, 1957.

[18] R. P. Feynman and M. Gell-Mann. Theory of the fermi interaction. *Phys. Rev.*, 109:193–198, Jan 1958.

[19] F. J. Hasert et al. Observation of Neutrino Like Interactions Without Muon Or Electron in the Gargamelle Neutrino Experiment. *Phys. Lett. B*, 46:138–140, 1973.

[20] Sheldon L. Glashow. The renormalizability of vector meson interactions. *Nucl. Phys.*, 10:107–117, 1959.

[21] Abdus Salam and John Clive Ward. Weak and electromagnetic interactions. *Nuovo Cim.*, 11:568–577, 1959.

[22] Steven Weinberg. A Model of Leptons. *Phys. Rev. Lett.*, 19:1264–1266, 1967.

[23] Eite Tiesinga, Peter J. Mohr, David B. Newell, and Barry N. Taylor. Codata recommended values of the fundamental physical constants: 2018. *Rev. Mod. Phys.*, 93:025010, Jun 2021.

[24] Nicola Cabibbo. Unitary Symmetry and Leptonic Decays. *Phys. Rev. Lett.*, 10:531–533, 1963.

[25] S. L. Glashow, J. Iliopoulos, and L. Maiani. Weak Interactions with Lepton-Hadron Symmetry. *Phys. Rev. D*, 2:1285–1292, 1970.

[26] S. W. Herb. Observation of a dimuon resonance at 9.5 gev in 400-gev proton-nucleus collisions. *Physical Review Letters*, 39(5), 1 1977.

[27] Makoto Kobayashi and Toshihide Maskawa. CP Violation in the Renormalizable Theory of Weak Interaction. *Prog. Theor. Phys.*, 49:652–657, 1973.

[28] Jr. Davis, Raymond, Don S. Harmer, and Kenneth C. Hoffman. Search for neutrinos from the sun. *Phys. Rev. Lett.*, 20:1205–1209, 1968.

[29] Q.R. Ahmad et al. Direct evidence for neutrino flavor transformation from neutral current interactions in the Sudbury Neutrino Observatory. *Phys. Rev. Lett.*, 89:011301, 2002.

[30] Y. Fukuda et al. Evidence for oscillation of atmospheric neutrinos. *Phys. Rev. Lett.*, 81:1562–1567, 1998.

[31] Ziro Maki, Masami Nakagawa, and Shoichi Sakata. Remarks on the unified model of elementary particles. *Prog. Theor. Phys.*, 28:870–880, 1962.

[32] B. Pontecorvo. Inverse beta processes and nonconservation of lepton charge. *Sov. Phys. JETP*, 7:172–173, 1958.

[33] ABHAY ASHTEKAR. Loop quantum gravity: Four recent advances and a dozen frequently asked questions. *The Eleventh Marcel Grossmann Meeting*, Sep 2008.

[34] C. Marletto and V. Vedral. Gravitationally induced entanglement between two massive particles is sufficient evidence of quantum effects in gravity. *Phys. Rev. Lett.*, 119:240402, Dec 2017.

[35] H. C. van de Hulst, E. Raimond, and H. van Woerden. Rotation and density distribution of the Andromeda nebula derived from observations of the 21-cm line. *Bulletin of the Astronomical Institutes of the Netherlands, Vol. 14, p.1*, 14:1, November 1957.

[36] V. C. Rubin, Jr. Ford, W. K., and N. Thonnard. Rotational properties of 21 SC galaxies with a large range of luminosities and radii, from NGC 4605

(R=4kpc) to UGC 2885 (R=122kpc). *Astrophysical Journal*, 238:471–487, June 1980.

[37] G. F. et al Smoot. Structure in the cobe differential microwave radiometer first-year maps. *Astrophysical Journal Letters*, 396(1 PART 2):L1–L5, 1992.

[38] R. Adam et al. Planck 2015 results. I. Overview of products and scientific results. *Astron. Astrophys.*, 594:A1, 2016.

[39] A. D. Sakharov. Violation of CP Invariance, C Asymmetry, and Baryon Asymmetry of the Universe. *Soviet Journal of Experimental and Theoretical Physics Letters*, 5:24, January 1967.

[40] Y. Fukuda et al. Evidence for oscillation of atmospheric neutrinos. *Phys. Rev. Lett.*, 81:1562–1567, 1998.

[41] Gregory Ciezarek, Manuel Franco Sevilla, Brian Hamilton, Robert Kowalewski, Thomas Kuhr, Vera Lüth, and Yutaro Sato. A challenge to lepton universality in b-meson decays. *Nature*, 546(7657):227–233, Jun 2017.

[42] Aldo Antognini et al. Proton Structure from the Measurement of $2S-2P$ Transition Frequencies of Muonic Hydrogen. *Science*, 339:417–420, 2013.

[43] Randolf Pohl et al. The size of the proton. *Nature*, 466:213–216, 2010.

[44] Peter J. Mohr, Barry N. Taylor, and David B. Newell. CODATA Recommended Values of the Fundamental Physical Constants: 2010. *Rev. Mod. Phys.*, 84:1527–1605, 2012.

[45] J.C. Bernauer et al. High-precision determination of the electric and magnetic form factors of the proton. *Phys. Rev. Lett.*, 105:242001, 2010.

[46] G.W. Bennett et al. Final Report of the Muon E821 Anomalous Magnetic Moment Measurement at BNL. *Phys. Rev. D*, 73:072003, 2006.

[47] J. Grange et al. Muon (g-2) Technical Design Report. 1 2015.

[48] B. Abi et al. Measurement of the Positive Muon Anomalous Magnetic Moment to 0.46 ppm. *Phys. Rev. Lett.*, 126(14):141801, 2021.

[49] Wilhelm H. Bertl et al. Search for the Decay $\mu^+ \to e^+e^+e^-$. *Nucl. Phys. B*, 260:1–31, 1985.

[50] A.M. Baldini et al. Search for the lepton flavour violating decay $\mu^+ \to \mathrm{e}^+\gamma$ with the full dataset of the MEG experiment. *Eur. Phys. J. C*, 76(8):434, 2016.

[51] R.H. Bernstein and Peter S. Cooper. Charged lepton flavor violation: An experimenter's guide. *Physics Reports*, 532(2):27–64, Nov 2013.

[52] Samoil M. Bilenky, S.T. Petcov, and B. Pontecorvo. Lepton Mixing, $\mu \to e^+\gamma$ Decay and Neutrino Oscillations. *Phys. Lett. B*, 67:309, 1977.

[53] S.T. Petcov. The Processes $\mu \to e^+\gamma$, $\mu \to ee\overline{e}$, $\nu \to \nu\gamma$ in the Weinberg-Salam Model with Neutrino Mixing. *Sov. J. Nucl. Phys.*, 25:340, 1977. [Erratum: Sov.J.Nucl.Phys. 25, 698 (1977), Erratum: Yad.Fiz. 25, 1336 (1977)].

[54] Yoshitaka Kuno and Yasuhiro Okada. Muon decay and physics beyond the standard model. *Rev. Mod. Phys.*, 73:151–202, 2001.

[55] Ann-Kathrin Perrevoort. *Sensitivity Studies on New Physics in the Mu3e Experiment and Development of Firmware for the Front-End of the Mu3e Pixel Detector*. PhD thesis, U. Heidelberg (main), 2018.

[56] William J. Marciano, Toshinori Mori, and J.Michael Roney. Charged Lepton Flavor Violation Experiments. *Ann. Rev. Nucl. Part. Sci.*, 58:315–341, 2008.

[57] H. Georgi. Effective field theory. *Ann. Rev. Nucl. Part. Sci.*, 43:209–252, 1993.

[58] Andre de Gouvea and Petr Vogel. Lepton Flavor and Number Conservation, and Physics Beyond the Standard Model. *Prog. Part. Nucl. Phys.*, 71:75–92, 2013.

[59] Savas Dimopoulos and Howard Georgi. Softly broken supersymmetry and su(5). *Nuclear Physics B*, 193(1):150–162, 1981.

[60] Ugo Amaldi, Wim de Boer, and Hermann Furstenau. Comparison of grand unified theories with electroweak and strong coupling constants measured at LEP. *Phys. Lett. B*, 260:447–455, 1991.

[61] K. Huitu, J. Maalampi, M. Raidal, and A. Santamaria. New constraints on R-parity violation from mu e conversion in nuclei. *Phys. Lett. B*, 430:355–362, 1998.

[62] T. P. Cheng and Ling-Fong Li. Neutrino masses, mixings, and oscillations in su(2)×u(1) models of electroweak interactions. *Phys. Rev. D*, 22:2860–2868, Dec 1980.

[63] Martti Raidal and Arcadi Santamaria. Muon electron conversion in nuclei versus mu —> e gamma: An Effective field theory point of view. *Phys. Lett. B*, 421:250–258, 1998.

[64] Yoshitaka Kuno. A search for muon-to-electron conversion at J-PARC: The COMET experiment. *PTEP*, 2013:022C01, 2013.

[65] L. Bartoszek, E. Barnes, J. P. Miller, J. Mott, A. Palladino, J. Quirk, B. L. Roberts, J. Crnkovic, V. Polychronakos, V. Tishchenko, P. Yamin, C. h. Cheng, B. Echenard, K. Flood, D. G. Hitlin, J. H. Kim, T. S. Miyashita, F. C. Porter, M. Röhrken, J. Trevor, R. Y. Zhu, E. Heckmaier, T. I. Kang, G. Lim, W. Molzon, Z. You, A. M. Artikov, J. A. Budagov, Yu. I. Davydov, V. V. Glagolev, A. V. Simonenko, Z. U. Usubov, S. H. Oh, C. Wang, G. Ambrosio, N. Andreev, D. Arnold, M. Ball, R. H. Bernstein, A. Bianchi, K. Biery, R. Bossert, M. Bowden, J. Brandt, G. Brown, H. Brown, M. Buehler, M. Campbell, S. Cheban, M. Chen, J. Coghill, R. Coleman, C. Crowley, A. Deshpande, G. Deuerling, J. Dey, N. Dhanaraj, M. Dinnon, S. Dixon, B. Drendel, N. Eddy, R. Evans, D. Evbota, J. Fagan, S. Feher, B. Fellenz, H. Friedsam, G. Gallo, A. Gaponenko, M. Gardner, S. Gaugel, K. Genser, G. Ginther, H. Glass, D. Glenzinski, D. Hahn, S. Hansen, B. Hartsell, S. Hays, J. A. Hocker, E. Huedem, D. Huffman, A. Ibrahim, C. Johnstone, V. Kashikhin, V. V. Kashikhin, P. Kasper, T. Kiper, D. Knapp, K. Knoepfel, L. Kokoska, M. Kozlovsky, G. Krafczyk, M. Kramp, S. Krave, K. Krempetz, R. K. Kutschke, R. Kwarciany, T. Lackowski, M. J. Lamm, M. Larwill, F. Leavell, D. Leeb,

A. Leveling, D. Lincoln, V. Logashenko, V. Lombardo, M. L. Lopes, A. Makulski, A. Martinez, D. McArthur, F. McConologue, L. Michelotti, N. Mokhov, J. Morgan, A. Mukherjee, P. Murat, V. Nagaslaev, D. V. Neuffer, T. Nicol, J. Niehoff, J. Nogiec, M. Olson, D. Orris, R. Ostojic, T. Page, C. Park, T. Peterson, R. Pilipenko, A. Pla-Dalmau, V. Poloubotko, M. Popovic, E. Prebys, P. Prieto, V. Pronskikh, D. Pushka, R. Rabehl, R. E. Ray, R. Rechenmacher, R. Rivera, W. Robotham, P. Rubinov, V. L. Rusu, V. Scarpine, W. Schappert, D. Schoo, A. Stefanik, D. Still, Z. Tang, N. Tanovic, M. Tartaglia, G. Tassotto, D. Tinsley, R. S. Tschirhart, G. Vogel, R. Wagner, R. Wands, M. Wang, S. Werkema, H. B. White Jr. au2, J. Whitmore, R. Wielgos, R. Woods, C. Worel, R. Zifko, P. Ciambrone, F. Colao, M. Cordelli, G. Corradi, E. Dane, S. Giovannella, F. Happacher, A. Luca, S. Miscetti, B. Ponzio, G. Pileggi, A. Saputi, I. Sarra, R. S. Soleti, V. Stomaci, M. Martini, P. Fabbricatore, S. Farinon, R. Musenich, D. Alexander, A. Daniel, A. Empl, E. V. Hungerford, K. Lau, G. D. Gollin, C. Huang, D. Roderick, B. Trundy, D. Na. Brown, D. Ding, Yu. G. Kolomensky, M. J. Lee, M. Cascella, F. Grancagnolo, F. Ignatov, A. Innocente, A. L'Erario, A. Miccoli, A. Maffezzoli, P. Mazzotta, G. Onorato, G. M. Piacentino, S. Rella, F. Rossetti, M. Spedicato, G. Tassielli, A. Taurino, G. Zavarise, R. Hooper, D. No. Brown, R. Djilkibaev, V. Matushko, C. Ankenbrandt, S. Boi, A. Dychkant, D. Hedin, Z. Hodge, V. Khalatian, R. Majewski, L. Martin, U. Okafor, N. Pohlman, R. S. Riddel, A. Shellito, A. L. de Gouvea, F. Cervelli, R. Carosi, S. Di Falco, S. Donati, T. Lomtadze, G. Pezzullo, L. Ristori, F. Spinella, M. Jones, M. D. Corcoran, J. Orduna, D. Rivera, R. Bennett, O. Caretta, T. Davenne, C. Densham, P. Loveridge, J. Odell, R. Bomgardner, E. C. Dukes, R. Ehrlich, M. Frank, S. Goadhouse, R. Group, E. Ho, H. Ma, Y. Oksuzian, J. Purvis, Y. Wu, D. W. Hertzog, P. Kammel, K. R. Lynch, and J. L. Popp. Mu2e technical design report, 2015.

[66] U. Bellgardt et al. Search for the Decay mu+ —> e+ e+ e-. *Nucl. Phys. B*, 299:1–6, 1988.

[67] Malte Hildebrandt. The drift chamber system of the MEG experiment.

Nucl. Instrum. Meth. A, 623:111–113, 2010.

[68] A.M. Baldini et al. The design of the MEG II experiment. *Eur. Phys. J. C*, 78(5):380, 2018.

[69] Manolis Kargiantoulakis. A search for charged lepton flavor violation in the mu2e experiment. *Modern Physics Letters A*, 35(19):2030007, Apr 2020.

[70] Dzmitry Shoukavy. COMET status and plans. *EPJ Web Conf.*, 212:01006, 2019.

[71] MyeongJae Lee. Comet muon conversion experiment in j-parc. *Frontiers in Physics*, 6:133, 2018.

[72] C. Patrignani et al. (Particle Data Group). Particle data group review. *Chin. Phys. C*, 40(100001), 2016 and 2017 update.

[73] Dorothea vom Bruch. *Pixel Sensor Evaluation and Online Event Selection for the Mu3e Experiment.* PhD thesis, University of Heidelberg, 2017.

[74] A. Bravar. The Mu3e experiment. *Nuclear and Particle Physics Proceedings*, 287-288:169 – 172, 2017. The 14th International Workshop on Tau Lepton Physics.

[75] Virgil L. Highland. Some Practical Remarks on Multiple Scattering. *Nucl. Instrum. Meth.*, 129:497, 1975.

[76] A.E. Pifer, T. Bowen, and K.R. Kendall. A high stopping density μ^+ beam. *Nuclear Instruments and Methods*, 135(1):39 – 46, 1976.

[77] Dorothea vom Bruch. Online Data Reduction using Track and Vertex Reconstruction on GPUs for the Mu3e Experiment. *EPJ Web Conf.*, 150:00013, 2017.

[78] Heiko Augustin et al. The Mu3e Data Acquisition. *IEEE Trans. Nucl. Sci.*, 68(8):1833–1840, 2021.

[79] Niklaus Berger, Moritz Kiehn, Alexandr Kozlinskiy, and Andre Schöning. A New Three-Dimensional Track Fit with Multiple Scattering. *Nucl. Instrum. Meth. A*, 844:135, 2017.

[80] Kalman Rudolph Emil. A new approach to linear filtering and prediction problems. *Transactions of the ASME–Journal of Basic Engineering*, 82(Series D):35–45, 1960.

[81] J. Allison, K. Amako, J. Apostolakis, H. Araujo, P. Arce Dubois, M. Asai, G. Barrand, R. Capra, S. Chauvie, R. Chytracek, G.A.P. Cirrone, G. Cooperman, G. Cosmo, G. Cuttone, G.G. Daquino, M. Donszelmann, M. Dressel, G. Folger, F. Foppiano, J. Generowicz, V. Grichine, S. Guatelli, P. Gumplinger, A. Heikkinen, I. Hrivnacova, A. Howard, S. Incerti, V. Ivanchenko, T. Johnson, F. Jones, T. Koi, R. Kokoulin, M. Kossov, H. Kurashige, V. Lara, S. Larsson, F. Lei, O. Link, F. Longo, M. Maire, A. Mantero, B. Mascialino, I. McLaren, P. Mendez Lorenzo, K. Minamimoto, K. Murakami, P. Nieminen, L. Pandola, S. Parlati, L. Peralta, J. Perl, A. Pfeiffer, M.G. Pia, A. Ribon, P. Rodrigues, G. Russo, S. Sadilov, G. Santin, T. Sasaki, D. Smith, N. Starkov, S. Tanaka, E. Tcherniaev, B. Tome, A. Trindade, P. Truscott, L. Urban, M. Verderi, A. Walkden, J.P. Wellisch, D.C. Williams, D. Wright, and H. Yoshida. Geant4 developments and applications. *IEEE Transactions on Nuclear Science*, 53(1):270–278, 2006.

[82] J. Allison, K. Amako, J. Apostolakis, P. Arce, M. Asai, T. Aso, E. Bagli, A. Bagulya, S. Banerjee, G. Barrand, B.R. Beck, A.G. Bogdanov, D. Brandt, J.M.C. Brown, H. Burkhardt, Ph. Canal, D. Cano-Ott, S. Chauvie, K. Cho, G.A.P. Cirrone, G. Cooperman, M.A. Cortés-Giraldo, G. Cosmo, G. Cuttone, G. Depaola, L. Desorgher, X. Dong, A. Dotti, V.D. Elvira, G. Folger, Z. Francis, A. Galoyan, L. Garnier, M. Gayer, K.L. Genser, V.M. Grichine, S. Guatelli, P. Guèye, P. Gumplinger, A.S. Howard, I. Hřivnáčová, S. Hwang, S. Incerti, A. Ivanchenko, V.N. Ivanchenko, F.W. Jones, S.Y. Jun, P. Kaitaniemi, N. Karakatsanis, M. Karamitros, M. Kelsey, A. Kimura, T. Koi, H. Kurashige, A. Lechner, S.B. Lee, F. Longo, M. Maire, D. Mancusi, A. Mantero, E. Mendoza, B. Morgan, K. Murakami, T. Nikitina, L. Pandola, P. Paprocki, J. Perl, I. Petrović, M.G. Pia, W. Pokorski, J.M. Quesada, M. Raine, M.A. Reis, A. Ribon, A. Ristić Fira, F. Romano, G. Russo, G. Santin, T. Sasaki, D. Sawkey, J.I. Shin, I.I. Strakovsky, A. Taborda, S. Tanaka, B. Tomé,

T. Toshito, H.N. Tran, P.R. Truscott, L. Urban, V. Uzhinsky, J.M. Verbeke, M. Verderi, B.L. Wendt, H. Wenzel, D.H. Wright, D.M. Wright, T. Yamashita, J. Yarba, and H. Yoshida. Recent developments in geant4. *Nuclear Instruments and Methods in Physics Research Section A: Accelerators, Spectrometers, Detectors and Associated Equipment*, 835:186–225, 2016.

[83] S. Agostinelli, J. Allison, K. Amako, J. Apostolakis, H. Araujo, P. Arce, M. Asai, D. Axen, S. Banerjee, G. Barrand, F. Behner, L. Bellagamba, J. Boudreau, L. Broglia, A. Brunengo, H. Burkhardt, S. Chauvie, J. Chuma, R. Chytracek, G. Cooperman, G. Cosmo, P. Degtyarenko, A. Dell'Acqua, G. Depaola, D. Dietrich, R. Enami, A. Feliciello, C. Ferguson, H. Fesefeldt, G. Folger, F. Foppiano, A. Forti, S. Garelli, S. Giani, R. Giannitrapani, D. Gibin, J.J. Gómez Cadenas, I. González, G. Gracia Abril, G. Greeniaus, W. Greiner, V. Grichine, A. Grossheim, S. Guatelli, P. Gumplinger, R. Hamatsu, K. Hashimoto, H. Hasui, A. Heikkinen, A. Howard, V. Ivanchenko, A. Johnson, F.W. Jones, J. Kallenbach, N. Kanaya, M. Kawabata, Y. Kawabata, M. Kawaguti, S. Kelner, P. Kent, A. Kimura, T. Kodama, R. Kokoulin, M. Kossov, H. Kurashige, E. Lamanna, T. Lampén, V. Lara, V. Lefebure, F. Lei, M. Liendl, W. Lockman, F. Longo, S. Magni, M. Maire, E. Medernach, K. Minamimoto, P. Mora de Freitas, Y. Morita, K. Murakami, M. Nagamatu, R. Nartallo, P. Nieminen, T. Nishimura, K. Ohtsubo, M. Okamura, S. O'Neale, Y. Oohata, K. Paech, J. Perl, A. Pfeiffer, M.G. Pia, F. Ranjard, A. Rybin, S. Sadilov, E. Di Salvo, G. Santin, T. Sasaki, N. Savvas, Y. Sawada, S. Scherer, S. Sei, V. Sirotenko, D. Smith, N. Starkov, H. Stoecker, J. Sulkimo, M. Takahata, S. Tanaka, E. Tcherniaev, E. Safai Tehrani, M. Tropeano, P. Truscott, H. Uno, L. Urban, P. Urban, M. Verderi, A. Walkden, W. Wander, H. Weber, J.P. Wellisch, T. Wenaus, D.C. Williams, D. Wright, T. Yamada, H. Yoshida, and D. Zschiesche. Geant4—a simulation toolkit. *Nuclear Instruments and Methods in Physics Research Section A: Accelerators, Spectrometers, Detectors and Associated Equipment*, 506(3):250–303, 2003.

[84] W.E. Fischer and F. Scheck. Electron Polarization in Polarized Muon

Decay: Radiative Corrections. *Nucl. Phys. B*, 83:25–31, 1974.

[85] Florian Scheck. Muon Physics. *Phys. Rept.*, 44:187, 1978.

[86] C. Fronsdal and H. Uberall. mu-Meson Decay with Inner Bremsstrahlung. *Phys. Rev.*, 113:654–657, 1959.

[87] Yoshitaka Kuno and Yasuhiro Okada. Muon decay and physics beyond the standard model. *Rev. Mod. Phys.*, 73:151–202, 2001.

[88] G. M. Pruna, A. Signer, and Y. Ulrich. Fully differential NLO predictions for the rare muon decay. *Phys. Lett. B*, 765:280–284, 2017.

[89] Angela Papa. The high intensity muon beam (himb) project at psi. EPS-HEP, 2019.

[90] Chih-hsiang. Cheng, Bertrand Echenard, and David G. Hitlin. The next generation of $\mu \to e\gamma$ and $\mu \to 3e$ CLFV search experiments. In *Proceedings, 2013 Community Summer Study on the Future of U.S. Particle Physics: Snowmass on the Mississippi (CSS2013): Minneapolis, MN, USA, July 29-August 6, 2013*, 9 2013.

[91] M. Mager. ALPIDE, the Monolithic Active Pixel Sensor for the ALICE ITS upgrade. *Nucl. Instrum. Meth. A*, 824:434–438, 2016.

[92] Ivan Peric. A novel monolithic pixelated particle detector implemented in high-voltage CMOS technology. *Nucl. Instrum. Meth.*, A582:876–885, 2007.

[93] Heiko Christian Augustin et al. MuPix8 - A large-area HV-MAPS chip. *PoS*, Vertex2017:057, 2018.

[94] H. Augustin et al. MuPix8 — Large area monolithic HVCMOS pixel detector for the Mu3e experiment. *Nucl. Instrum. Meth. A*, 936:681–683, 2019.

[95] H. Augustin et al. Performance of the large scale HV-CMOS pixel sensor MuPix8. *JINST*, 14(10):C10011, 2019.

[96] H. Augustin et al. The MuPix Telescope: A Thin, high Rate Tracking Telescope. *JINST*, 12(01):C01087, 2017.

[97] Lennart Huth. *A High Rate Testbeam Data Acquisition System and Characterization of High Voltage Monolithic Active Pixel Sensors*. PhD thesis, University of Heidelberg, 2018.

[98] Intel. stratix iv - features. https://www.intel.com/content/dam/www/programmable/us/en/pdfs/literature/pt/stratix-iv-product-table.pdf. Accessed: 15/02/21.

[99] Frank Meier Aeschbacher, Marin Deflorin, and Lars Olivier Sebastian Noehte. Mechanics, readout and cooling systems of the Mu3e experiment. In *28th International Workshop on Vertex Detectors*, 3 2020.

[100] Luise Poley and Tim Jones. Measuring the coefficient of moisture expansion of Hysol 9396 loaded with boron nitride powder. *JINST*, 15(09):P09007, 2020.

[101] R. Kleiss, W. James Stirling, and S. D. Ellis. A New Monte Carlo Treatment of Multiparticle Phase Space at High-energies. *Comput. Phys. Commun.*, 40:359, 1986.

[102] S. Corrodi. *A Timing Detector based on Scintillating Fibres for the Mu3e Experiment*. PhD thesis, ETH Zürich, 2018.

[103] G.M. Pruna, A. Signer, and Y. Ulrich. Fully differential NLO predictions for the rare muon decay. *Phys. Lett. B*, 765:280–284, 2017.

[104] R. R. Crittenden, W. D. Walker, and J. Ballam. Radiative decay modes of the muon. *Phys. Rev.*, 121:1823–1832, Mar 1961.

[105] A.M. Baldini et al. Measurement of the radiative decay of polarized muons in the MEG experiment. *Eur. Phys. J. C*, 76(3):108, 2016.

[106] Glen Cowan, Kyle Cranmer, Eilam Gross, and Ofer Vitells. Asymptotic formulae for likelihood-based tests of new physics. *Eur. Phys. J. C*, 71:1554, 2011. [Erratum: Eur.Phys.J.C 73, 2501 (2013)].